ELECTRONIC STRUCTURE AND NUCLEAR MAGNETIC RESONANCE CHEMICAL SHIFT OF SOLIDS AND SURFACES

by

Bernd Georg Pfrommer

Dipl. Phys. (Universität Stuttgart) 1993

A dissertation submitted in partial satisfaction of the

requirements for the degree of

Doctor of Philosophy

in

Physics

in the

GRADUATE DIVISION

of the

UNIVERSITY of CALIFORNIA at BERKELEY

Committee in charge:

Professor Steven G. Louie, Chair

Professor Peter Yu

Professor Raymond Jeanloz

1998

The dissertation of Bernd Georg Pfrommer is approved:

Chair   Date

Date

Date

University of California at Berkeley

1998

ELECTRONIC STRUCTURE AND NUCLEAR MAGNETIC RESONANCE CHEMICAL SHIFT OF SOLIDS AND SURFACES ©1998

by

Bernd Georg Pfrommer

Abstract

ELECTRONIC STRUCTURE AND NUCLEAR MAGNETIC RESONANCE CHEMICAL SHIFT OF SOLIDS AND SURFACES

by

Bernd Georg Pfrommer

Doctor of Philosophy in Physics

University of California at Berkeley

Professor Steven G. Louie, Chair

Several different topics related to the electronic structure of solids and surfaces are discussed in this thesis. With the quasi-Newton algorithm for relaxing crystal structures, and a new *ab initio* method to compute nuclear magnetic resonance (NMR) chemical shifts, numerical methods are developed and implemented to efficiently compute properties related to the electronic structure. These techniques are then applied to a range of different materials. The quasi-Newton method is used to study the recently discovered high-pressure R8 phase of silicon, and the fcc-hcp high-pressure structural phase transition of xenon. Using the pressure-induced magnetic phase transition of a model atomic hydrogen crystal as a test system, the accuracy of density functional theory in both the generalized gradient approximation (GGA) and the local spin density approximation (LSDA) is compared to variational quantum Monte Carlo (VQMC) calculations [1]. Finally, for the first time, the NMR chemical shift of extended systems such as amorphous carbon and the hydrogenated diamond (111) surface are calculated from first principles.

- In the first chapter, a model body-centered cubic (bcc) atomic hydrogen solid is studied using density functional theory in LSDA and GGA. In GGA, the paramagnetic to antiferromagnetic phase transition occurs at a higher density, and is in much better agreement with previous VQMC calculations than LSDA. The metal-insulator transition in GGA is observed at a higher density and is also closer to the VQMC result than LSDA. For the limit of isolated hydrogen atoms, it is found that in GGA the self-consistent electron density is greatly improved over LSDA due to a better cancellation of the spurious electronic self-interaction.

- How a quasi-Newton method can be used to simultaneously relax the internal coordinates and lattice parameters of crystals under pressure is the subject of the second chapter. The symmetry of the crystal structure is preserved during the relaxation. From the inverse of the Hessian matrix, elastic properties and some optical phonon frequencies at the Brillouin zone center can be estimated. The efficiency of the method is demonstrated for silicon test systems.

- Chapter three presents a detailed *ab initio* study of the electronic and structural properties of the recently discovered R8 phase of silicon. Within the framework of density functional

theory in LDA, and using pseudopotentials with a plane wave basis set, the energetics of the R8 phase compared to the other tetrahedrally-bonded diamond, β-Sn, and BC8 phases, are examined. The bonding properties and the pressure dependence of the bond lengths of the BC8 and R8 phases are investigated. An analysis of the band structure reveals that R8 silicon could be a semimetal or a semiconductor with a small, indirect band gap. The computed density of states of R8 silicon shows a sharpening of the valence band edge similar to the one observed for amorphous silicon.

- In chapter four, the fcc-hcp high pressure structural phase transition of xenon is calculated, and the results are compared with experimental data from S. Caldwell, J. Nguyen, and R. Jeanloz [2]. Also, several candidate xenon-iron compounds under pressures of up to 500 GPa are simulated in order to explore the possibility of xenon having compounded with the iron in Earth's core, which could explain the low abundance of Xe in Earth's atmosphere. However, it is found that all considered Xe and Fe compounds are rather unstable, and even at high pressures, the formation of a chemical bond is unlikely.

- Chapter five describes a theory for the *ab initio* computation of the NMR chemical shift in extended systems, using periodic boundary conditions. This approach can be applied to periodic systems like crystals, surfaces, or polymers and, with a supercell technique, to non-periodic systems such as amorphous materials, liquids, or solids with defects. Calculations of hydrogen chemical shifts for a set of free molecules are presented, using density functional theory in LDA.

- In chapter six, the NMR chemical shift spectra of diamond, CVD diamond, and diamond-like amorphous carbon are computed from first principles. The results are in excellent agreement with experiments, and are useful for the interpretation of NMR spectra in terms of the microscopic structure of the materials. In particular, it is shown that the NMR and Raman line widths in polycrystalline CVD diamond are due to stress fluctuations, and a heterogeneous model for the amorphous hydrogenated phase is supported.

- Unexpected features in the NMR chemical shift spectra of the hydrogenated diamond (111) surface are reported in chapter seven. On this surface, the presence of unoccupied surface states has a strong paramagnetic effect on the carbon chemical shift when the external magnetic field is applied parallel to the surface. As the surface states decay towards the interior of the diamond crystal, so does their paramagnetic influence, which might open up the possibility of measuring the decay of surface states by NMR.

Contents

List of Figures **v**

List of Tables **vi**

Acknowledgements **vii**

1 Density-functional study of solid bcc hydrogen **1**
- 1.1 Introduction 1
- 1.2 Hydrogen atom 2
- 1.3 Solid hydrogen 4

2 Relaxation of crystals with the quasi-Newton method **8**
- 2.1 Introduction 8
- 2.2 The quasi-Newton method for crystal structure relaxation 9
- 2.3 Optical phonon modes and elastic properties 11
- 2.4 Numerical tests 15
- 2.5 Symmetry conservation 19
- 2.6 Conclusion 20

3 Silicon in the R8 structure **21**
- 3.1 Introduction 21
- 3.2 Structures 21
- 3.3 Method 24
- 3.4 Stability of four-fold coordinated phases of silicon 24
- 3.5 Structural properties of the BC8 and R8 phase 26
- 3.6 Electronic properties of the BC8 and R8 phases 29
- 3.7 Conclusion 35

4 Structure and geochemistry of xenon at high pressures **36**
- 4.1 Introduction 36
- 4.2 Xenon under high pressure 37
- 4.3 Stability of xenon-iron compounds 40

5 *Ab initio* calculation of the NMR chemical shift **44**
- 5.1 Introduction 44
- 5.2 NMR chemical shift tensor and magnetic susceptibility 45
- 5.3 Chemical shift tensor as an energy derivative 46
- 5.4 Perturbation theory 47
- 5.5 Handling divergences with the sum rule 50
- 5.6 Implementation using pseudopotentials and plane waves 51
- 5.7 Test calculations on molecules 52

6 NMR chemical shift of diamond and amorphous carbon 53
6.1 Introduction 53
6.2 Notation and tests 53
6.3 CVD diamond 54
6.4 Amorphous carbon 55
6.5 Conclusion 60

7 Surface state effects on the NMR chemical shift 61
7.1 Introduction 61
7.2 NMR chemical shifts on surfaces 61
7.3 Results for the hydrogenated diamond (111) surface 62
7.4 Analysis 64
7.5 Conclusion 67

Bibliography 68

List of Figures

1.1 Electron density of the hydrogen atom in LSDA and GGA. 3
1.2 Exchange-correlation potential of the hydrogen atom in LSDA and GGA. 4
1.3 Sublattice magnetic moment of the bcc hydrogen solid in LSDA, GGA, and VQMC. . . 6
1.4 Energy gap of the bcc hydrogen solid in LSDA, GGA, and VQMC. 7

2.1 Relaxation of a 16-atom silicon supercell with the quasi-Newton method. 17
2.2 Relaxation of the silicon R8 phase with the quasi-Newton method. 18

3.1 Ball and stick model of the silicon BC8 phase. 22
3.2 Ball and stick model of the silicon R8 phase. 23
3.3 Enthalpy of tetrahedral phases of silicon as a function of pressure. 25
3.4 Volume and rhombohedral angle of the silicon BC8 and R8 phases as a function of pressure. 27
3.5 Internal degrees of freedom of R8 silicon as a function of pressure. 28
3.6 Bond lengths of BC8 and R8 silicon as a function of pressure. 30
3.7 Band structures of BC8 and R8 silicon. 31
3.8 Density of states of BC8 and R8 silicon. 32
3.9 Local density of states of R8 silicon for the 2(c) atom. 33
3.10 Local density of states of R8 silicon for the 6(f) atom. 34

4.1 Enthalpy of fcc and hcp Xe as a function of pressure. 37
4.2 Unit cell parameters of fcc and hcp Xe as a function of pressure. 38
4.3 c/a ratio of hcp Xe as a function of pressure. 39
4.4 Electron density isosurface of $XeFe_2$ in the Laves phase. 41
4.5 Calculated density of hcp Xe and Fe as a function of pressure. 42

5.1 Influence of the sample shape on the NMR chemical shift. 45

6.1 Raman versus NMR line width in CVD diamond. 55
6.2 H chemical shift spectra in hydrogenated amorphous carbon. 57
6.3 C chemical shift spectra in hydrogenated amorphous carbon. 58
6.4 C chemical shift spectra in pure amorphous carbon. 59

7.1 Chemical shift of the hydrogenated diamond (111) surface as a function of layer depth. . 63
7.2 Induced current density and square modulus of a surface state of the hydrogenated diamond (111) surface. 65
7.3 Calculated energies of bulk and surface bands of the hydrogenated diamond (111) surface. 66

List of Tables

1.1 Energy contributions for the hydrogen atom in GGA and LSDA. 2

3.1 Ring count for the diamond, BC8, and R8 phases. 30

4.1 Enthalpy of formation of several model Xe-Fe compounds. 40

5.1 Computed and measured H chemical shifts of a set of molecules. 52

6.1 Calculated and measured C chemical shifts of a set of hydrocarbons in the gas phase. . 54
6.2 Calculated and measured C chemical shifts of diamond. 54

Acknowledgements

First I would like to acknowledge the financial and moral support I got from my advisor, Steven G. Louie.

Thanks also go to Francesco Mauri, who helped me during a difficult phase of my graduate student life. The method to compute the NMR chemical shifts presented in chapter 5 is his brainchild. We had a great deal of fun implementing this new method together, and finding the exciting results of chapters 6 and 7.

Sander Caldwell and Raymond Jeanloz are thanked for the always excellent collaboration on the xenon-iron project.

Thanks for helping me tackle the computational challenges go to Andrew Canning, Jim Demmel, Horst Simon, and the staff at the Illinois and Berkeley computing centers. In addition, Jing Zhu is acknowledged for getting me started on the hydrogen project.

Thanks are due to the entire Cohen-Louie group for many useful discussions.

Finally, thanks to my wife, Claudia, and my parents, for their encouragement during all these years.

Chapter 1

Density-functional study of solid bcc hydrogen

1.1 Introduction

Although density functional theory (DFT) in the local spin density approximation (LSDA) correctly describes the electronic structure of many systems, it fails in certain cases. In particular, the typical Mott insulators such as the transition metal oxides FeO and CoO are found to be metals. For CuO, not even the antiferromagnetic (AFM) order, a ground state property, is reproduced [3]. Likewise, the undoped parent compound of high-T_c materials, La_2CuO_4, is a paramagnetic metal [4] in LSDA, but an AFM insulator in experiment.

To overcome these difficulties, the LSDA has been improved in several different ways. The self-interaction-corrected LSDA (SIC-LSDA) correctly predicts that MnO, FeO, CoO, NiO, and CuO are AFM insulators, and drastically improves gaps and local magnetic moments [5]. Due to the numerical effort involved, this method is however not readily applicable to larger systems.

Other studies employ an "LDA+U" approach [3, 4, 6, 7, 8], where the local density approximation (LDA) or LSDA are augmented by additional terms to introduce the Hubbard energy U. These methods have enjoyed considerable success [4, 7] in that they correctly reproduce the AFM ground states of NiO, CoO, FeO, and La_2CuO_4. A systematic improvement of the ground-state and single-electron excited-state properties over LSDA has also been reported [9] for $LaMO_3$ perovskites (M=Ti-Cu). On the other hand, the method fails for early $3d$ transition-metal oxides [3].

Finally, generalized gradient approximations [10] (GGA) have been applied to Mott insulators. A fairly clear picture emerges from a literature review [11, 12, 13, 14]. GGA systematically improves over LSDA, but often not enough. For instance, the insulating $YTiO_3$ is metallic [11] both in GGA and LSDA, but with a smaller band overlap in GGA. GGA slightly enhances the magnetic moments of MnO, NiO, and CoO, and substantially improves the HOMO-LUMO band gaps of MnO and NiO [12]. In GGA, the AFM insulator $CaCuO_2$ is found [13] to be a paramagnetic (PM) metal, but it is closer to an AFM instability than in LSDA. For FeF_2, CoF_2 [13], YVO_3, and $LaVO_3$ [14], GGA correctly yields an insulator, whereas LSDA predicts a metal.

In this chapter, we compare the Ceperley-Alder [15] LSDA functional in the parametrization of Perdew and Zunger [16] with the Perdew-Wang 91 GGA functional (GGA PW91)[10]. We consider two systems: atomic hydrogen, and a model body-centered cubic (bcc) atomic hydrogen crystal. For atomic hydrogen, the exact solution to the electronic structure problem is known. In the bcc model solid, we can judge the quality of the density functionals by comparing with variational quantum Monte Carlo (VQMC) calculations from Jing Zhu's thesis [1]. We will focus on the accuracy with which the density functionals reproduce the magnetic and the Mott metal-insulator transitions. This transition is of particular interest because of the ongoing experimental efforts to produce metallic hydrogen [17, 18, 19]. In contrast with many metal oxides, solid hydrogen is a rather delocalized system, since near the phase transition, the hydrogen $1s$ wave functions overlap considerably. Therefore, the "LDA+U" method might not be appropriate here [6].

	E_{tot}	T	V	E_H	E_x	E_c	E_{xc}
Exact	-1	1	-2	0.625	-0.625	0	-0.625
LSDA	-0.958	0.933	-1.891	0.597	-0.513	-0.044	-0.557
PW91	-1.003	0.993	-1.991	0.615	-0.606	-0.013	-0.619

Table 1.1: Values (in Rydbergs) for total energy E_{tot}, kinetic energy T, potential energy V, Hartree energy E_H, exchange energy E_x, correlation energy E_c, and exchange-correlation energy E_{xc}. A self-consistent electron density is used for the GGA PW91 functional and the LSDA.

1.2 Hydrogen atom

In the Kohn-Sham [20] approach, the electronic energy E_{tot} is the sum of four terms:

$$E_{tot} = T + V + E_H + E_{xc} \ . \tag{1.1}$$

For a single-electron system such as the hydrogen atom, the exchange-correlation energy E_{xc} should exactly cancel the spurious self-interaction Hartree energy E_H, such that only the kinetic energy T and the ionic potential energy V are left, and the corresponding Kohn-Sham equation turns into Schrödinger's equation. The exchange-correlation energy E_{xc} can be decomposed further into exchange and correlation energy, $E_{xc} = E_x + E_c$, where E_x is defined as the Kohn-Sham exchange energy computed from the single-particle density matrix of the exact Kohn-Sham orbitals [21]. Obviously, $E_x = -E_H$, and therefore $E_c = 0$.

In Table 1.1, we show the numerical values for the various terms in (1.1) for the hydrogen atom. The energies have been calculated with the self-consistent electron number densities $n(\mathbf{r})$. Similar results have been published previously [21, 22], but not for self-consistent densities. For comparison, we also show the exact analytic results in Table 1.1. The GGA PW91 functional not only gives a much better agreement for the total energy than LSDA, but also the individual terms are closer to the exact values. Further, the separation between exchange and correlation appears to be improved, although from a practical point of view, this is immaterial.

As is evident from the kinetic and potential energy terms in Table 1.1, the self-consistent electron densities in GGA PW91 and LSDA must differ. They are shown in Fig. 1.1, along with the exact density. We see that the GGA PW91 pulls the wave function in towards the nucleus, compared to the LSDA, such that the self-consistent density is much closer to the exact one. This also explains why the kinetic energy is higher, and the potential energy is lower in GGA PW91 than in LSDA.

The differences in the self-consistent electron density are due to the exchange-correlation potential $v_{xc}(\mathbf{r}) = \delta E_{xc}/\delta n(\mathbf{r})$. Fig. 1.2 shows the exchange-correlation potentials for LSDA and GGA PW91, and the exact exchange-correlation potential, which is just the negative of the Hartree potential, $v_H(\mathbf{r}) = \int \frac{n(\mathbf{r}')}{|\mathbf{r}-\mathbf{r}'|} \mathrm{d}^3 r'$, using Rydberg units. We see that neither LSDA nor GGA PW91 track the exact exchange correlation potential well, and they both do not show the correct asymptotic limit [23] for large r, which is $\lim_{r\to\infty} v_{xc}(r) = -2/r$. The wiggle in the GGA PW91 exchange-correlation potential at about $r = 5$ a.u. (1 a.u. being the Bohr radius) is not an artifact of the implementation, but stems from the particular functional form of the PW91 exchange potential. Notice also the divergence at the origin, which is intrinsic to all gradient-corrected functionals. The improved quality of the electron density in GGA PW91 over LSDA thus appears somewhat fortuitous, since the potential shows deficiencies at large and small r, but has just the appropriate slope in the regime between $r \approx 1 - 3$ a.u. to yield a good density. A similar shape for $v_{xc}(r)$,

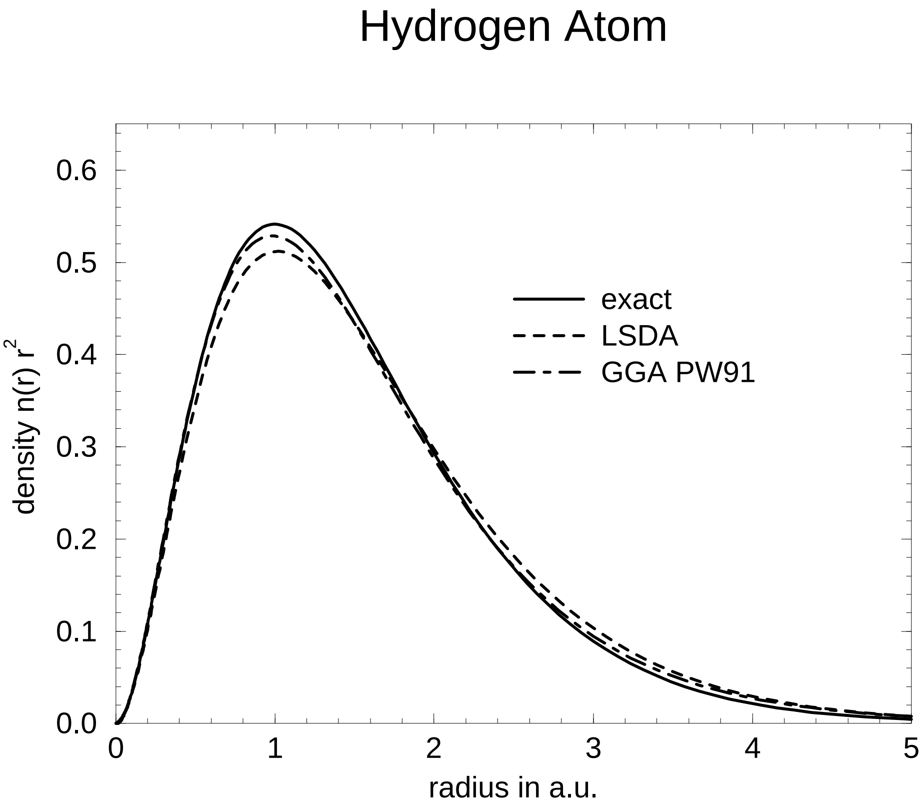

Figure 1.1: Electron number density $n(r)$ of the hydrogen atom as a function of the radius. Shown are the exact density (solid line), and the self-consistent densities in LSDA (dashed line) and GGA PW91 (dot-dashed line).

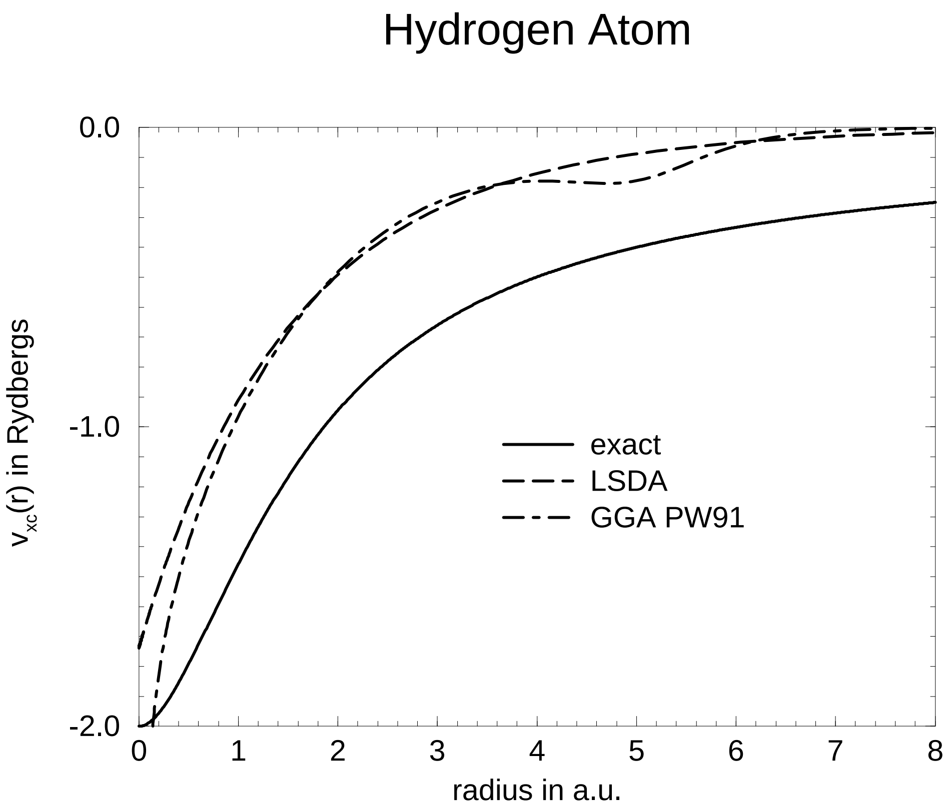

Figure 1.2: Exchange-correlation potential $v_{xc}(r)$ in Rydbergs for the hydrogen atom as a function of the radius. Shown are the exact v_{xc} (solid line), and the self-consistent v_{xc} in LSDA (dashed line) and GGA PW91 (dot-dashed line).

and a comparable improvement of the self-consistent density has been previously reported for the closed-shell helium [24] and neon [25] atoms.

1.3 Solid hydrogen

A crystal of sufficiently separated hydrogen atoms obviously is an insulator. However, without magnetic order, a one-electron band structure picture predicts metallic behavior, because the $1s$ band is only half filled. This error is remedied if AFM order is assumed [26], which leads to a doubling of the unit cell size, and can open a band gap. With now two atoms in the unit cell, there are four bands derived from the atomic $1s$ states (one for each spin and atom). Although by symmetry spin up and spin down bands are degenerate, the four bands can split into two pairs, separated by an energy gap. If the hydrogen atoms are brought closer together, the band dispersion increases, and at some critical lattice constant the occupied and unoccupied bands start overlapping, at which point the insulator becomes a metal. This can occur while still the AFM order is preserved. As the distance between the hydrogen atoms is decreased further, the AFM order vanishes, and a

PM metal is found.

In contrast with the band theory of “itinerant” Bloch electrons is the Hubbard model Hamiltonian approach [27], which was developed to describe systems where the electrons are fairly localized. There, two parameters describe the physical properties of the system: the electron hopping interaction t and the intra-atomic Coulomb correlation interaction energy U. Except for a few special cases, exact solutions of the Hubbard model Hamiltonian are not known. Some important conclusions however can be drawn from it [28]. For instance, Hubbard [27] demonstrated that the existence of an insulating gap can be independent of the existence of spin order. This is quite in contrast to the Slater picture, where the insulating phase must be spin ordered. Based on a screening argument, Mott argued that the metal-insulator transition should be of first order, and suggested that the magnetic transition might occur simultaneously with the metal-insulator transition [29]. However, since the long-range Coulomb interaction is treated as a short-range phenomenon in the Hubbard model, the physics of the Hubbard model metal-insulator transition should be quite different [28] from the one originally suggested by Mott [30].

By using the Kohn-Sham equations of DFT, we commit to band theory. There is no reason to believe that DFT must therefore fail. In fact, the magnetization is a ground state property, and is hence accessible to DFT. The Kohn-Sham eigenvalues on the other hand cannot be interpreted as quasi-particle excitation energies. It has been argued [3] that the gap in LSDA is related to a Hund’s rule exchange term rather than the Hubbard parameter U, and therefore the gap will necessarily come out too small. Because Kohn-Sham eigenvalues are nevertheless frequently used to characterize materials, we will compare LSDA and GGA gaps with those obtained from VQMC calculations.

Several DFT studies of atomic hydrogen solids can be found in the literature [5, 31, 32, 33, 34, 35]. Using LSDA and the linearized muffin-tin orbital method in the atomic sphere approximation (LMTO-ASA), Min [33] et al report a PM-AFM transition for bcc hydrogen at a Wigner-Seitz radius of $r_s = 2.55$ a.u., and a metal-insulator transition at $r_s = 2.85$ a.u.. Moruzzi and Marcus [34] employ LSDA to study a hydrogen fcc lattice, where they find a second-order PM-FM transition at $r_s = 2.7$ a.u. (the AFM solution was not considered). At $r_s = 3.0$ a.u. they observe a second-order metal-insulator transition. Finally, Svane and Gunnarsson [5] compare LSDA with the self-interaction corrected LSDA (SIC-LSDA), and find SIC-LSDA to produce a simultaneous first order PM-AFM and metal-insulator transition at $r_s = 2.45$ a.u. for the bcc hydrogen solid.

Our calculations on bcc hydrogen are performed using a local pseudopotential of the Kerker type [36] with a cutoff radius of 0.7 a.u.. The wave functions are expanded in plane waves up to a 60 Ry energy cutoff. A $14 \times 14 \times 14$ Monkhorst-Pack [37] grid is used to sample the Brillouin zone with 84 k-points in the irreducible wedge.

The results for the sublattice magnetic moment are shown in Fig. 1.3. In LSDA, the PM-AFM transition is found at $r_s = 2.5$ a.u., in agreement with previous results [5, 33]. With the GGA PW91, the phase transition occurs at the higher density $r_s = 2.25$ a.u., which is much closer to the VQMC result of $r_s = 2.2$ a.u.. Thus, GGA not only improves the description of the hydrogen atom, but also of the solid. From the absence of hysteresis and the shape of the curves in Fig. 1.3, we conclude that the PM-AFM transitions in both LSDA and GGA PW91 are of second order, or at most very weakly first order. The VQMC results indicate a weak first-order transition [1], but the statistical noise is too large for a definite statement. Notice that SIC-LSDA [5] observes the magnetic transition at $r_s = 2.45$ a.u., although this value might not be reliable due to sensitivities to the LSDA functional parameterization [5].

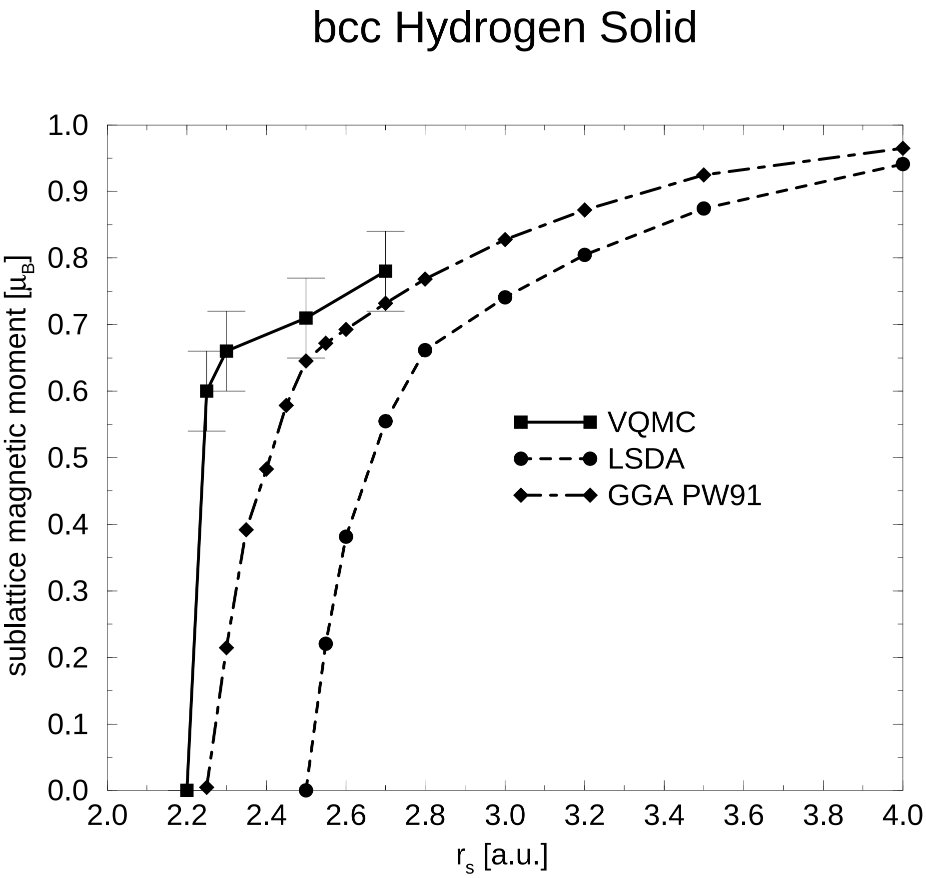

Figure 1.3: Sublattice magnetic moment of the bcc atomic hydrogen solid in units of μ_B (Bohr magneton) as a function of r_s in a.u.. The GGA magnetic moment (dot-dashed line) is close to the VQMC result (solid line), and clearly improves over LSDA (dashed line).

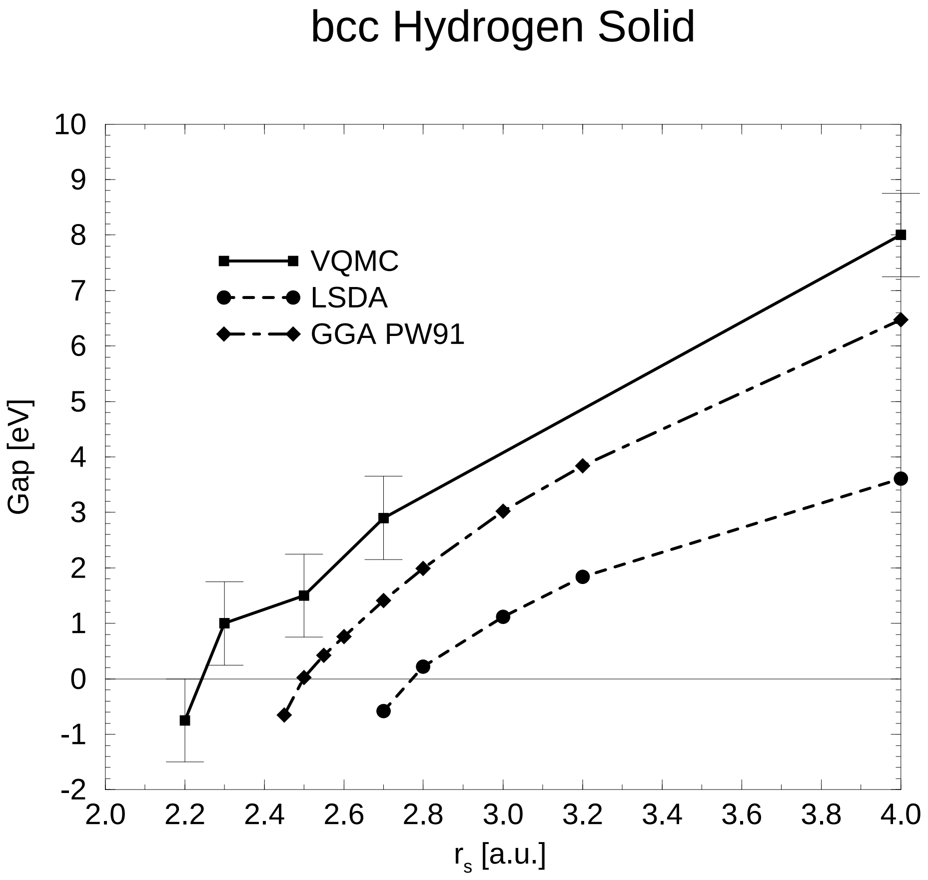

Figure 1.4: Energy gap (in eV) of the bcc hydrogen solid as a function of r_s (in a.u.). The GGA gap (dot-dashed line) opens at lower densities than in LSDA (dashed line), but is still off from the VQMC result (solid line).

Fig. 1.4 shows the band gap of bcc hydrogen at different densities. In close agreement with Min *et al.* [33], we find bcc hydrogen to be an insulator in LSDA for $r_s > 2.8$ a.u.. Using GGA PW91, the metal-insulator transition is observed at $r_s = 2.5$ a.u., and consequently occurs at lower density than the magnetic transition. VQMC on the other hand indicates metallic behavior for r_s smaller than about $2.2 - 2.3$ a.u., and thus the Mott and PM-AFM transitions occur at very similar densities. The agreement between GGA and VQMC is not as good as for the magnetic transition, but is much improved over LSDA.

In conclusion, it has been shown that for a bcc hydrogen crystal, GGA gives a metal-insulator and a PM-AFM phase transition at higher density than LSDA, and is in better agreement with VQMC results. Both transitions are most likely of second order in both LSDA and GGA. In the limit of the isolated hydrogen atom, the better cancellation of the self-interaction Hartree term in GGA leads to an improved self-consistent electron density, although the exchange-correlation potential in GGA is rather different from the exact one.

Chapter 2

Relaxation of crystals with the quasi-Newton method

2.1 Introduction

Ab initio computations of the total energy within the framework of density functional theory (DFT) and the local density approximation (LDA) [21] have been successful in predicting the structural properties of materials [38]. At zero temperature and pressure, the structural parameters are determined by moving the constituting atoms to positions where the energy E is minimal. This can be done much more efficiently if the forces on the atoms can be computed [39]. If a pressure p is applied to the material, it is the enthalpy $\mathcal{H} = E + pV$ which has to be minimized with respect to all structural parameters, including the volume V.

Our focus will be on crystalline materials at zero temperature, where the unit cell shape and the coordinates of the atoms inside the unit cell are the parameters to be adjusted such that the enthalpy acquires a minimum. In this chapter, we describe a symmetry-preserving algorithm to relax the unit cell shape and the atomic coordinates simultaneously by using the computed forces [39] and the stress [40]. This is a frequent task when structural phase transitions are studied, where one is interested in the properties of a phase with a given symmetry as a function of pressure. Although we demonstrate the efficiency of our method within the framework of DFT in LDA, it is of rather general use, and can be applied to relax crystal structures whenever forces and stress are available.

Quantum molecular dynamics schemes of different flavors are commonly used to tackle this problem. In contrast to the Car-Parrinello method [41], we follow the more traditional approach [42] and relax the electronic degrees of freedom completely before moving the atoms, and changing the shape of the unit cell. While the early molecular dynamics methods kept the unit cell shape of the crystal fixed, and relaxed only the internal degrees of freedom, the more recent algorithms allow for a variation of both. The first molecular dynamics approach with a variable unit cell *shape* was proposed by Parrinello and Rahman (PR) [43], where a fictitious Lagrangian governed the time evolution of internal coordinates and the cell shape. However, the crystal symmetry is not preserved along the trajectories derived from their Lagrangian, in other words the symmetry of the crystal can be reduced during the relaxation process. This is undesirable when structural phase transitions are examined, where one would like to impose the crystal symmetry. Picking the strain ϵ as time-dependent variable instead of the lattice vectors, Wentzcovitch [44] modified the PR Lagrangian to generate symmetry-preserving trajectories.

We present here a relaxation scheme which preserves the symmetry and is *not* based on a molecular dynamics approach, but uses a powerful quasi-Newton optimization scheme to search for the relaxed configuration. While this method has been applied to treat forces on atoms before [45], we report for the first time how to simultaneously relax the lattice parameters. The quasi-Newton method accumulates information about the enthalpy surface in the inverse of the Hessian matrix H, which renders it superior to the molecular dynamics algorithms proposed recently [42]. After the relaxation has been completed, H can be exploited to estimate elastic properties and the optical phonon energies at the center of the Brillouin zone. Using H obtained from similar calculations further improves the performance. We demonstrate the efficiency of our scheme for silicon in the diamond and the R8 phases [46].

2.2 The quasi-Newton method for crystal structure relaxation

We start this section by establishing the notation and defining the configuration space coordinates. The crystal structure is determined by the matrix of lattice vectors $h = \{a, b, c\}$ and the coordinates $s_i,\ i = 1, \dots N$ relative to h of the N atoms in the unit cell, which has a volume of $\Omega = \det(h)$. The energy E per unit cell is a function of h and the s_i's.

For convenience, we choose the finite strain tensor ϵ as a free variable instead of the lattice vectors h. It has 9 components and stretches a reference configuration h_0 into $h = (1+\epsilon)h_0$. Molecular dynamics schemes [44], [47] often constrain ϵ to be symmetric in order to avoid rotations of the unit cell. Since there is no notion of angular momentum in our scheme, we allow for an asymmetric ϵ to simplify the extraction of elastic properties and phonon modes in Section 2.3.

Relaxing a crystal structure with N atoms in the unit cell under the applied pressure p thus is an optimization problem for the enthalpy per unit cell $\mathcal{H} = E + p\Omega$ in a $9 + 3N$-dimensional space:

$$\mathcal{H} = \mathcal{H}(\epsilon, s_1, \dots s_N)\ . \tag{2.1}$$

Let us denote a point in configuration space by the column vector X. We define the first nine components of X to be the strain components ϵ, which are converted into a nine-element column vector by $X_{3(i-1)+j} = \epsilon_{ij};\ i, j = 1, 2, 3$. Then follow the coordinates of the atoms in the unit cell, $s_1, s_2, \dots s_N$. We will call the negative of the derivative of the enthalpy $\mathcal{H}$ with respect to X,

$$F = -\left.\frac{\partial \mathcal{H}}{\partial X}\right|_p\ , \tag{2.2}$$

the "force vector". The strain components of F are the derivatives of $\mathcal{H} = E + p\Omega$ with respect to ϵ:

$$f^{(\epsilon)} = -(\sigma + p\Omega)(1 + \epsilon^T)^{-1}\ , \tag{2.3}$$

where σ is the stress at a given configuration X:

$$\sigma = \left(\frac{\partial E((1+\epsilon')h)}{\partial \epsilon'}\right)_{\epsilon'=0}\ . \tag{2.4}$$

Notice that the right hand side of (2.3) need not be symmetric, and that we do not symmetrize it. Thus, ϵ can become asymmetric during the course of the relaxation.

The other $3N$ components of F are obtained by multiplying the forces on the atoms $f_1 \dots f_N$ in lattice coordinates with the metric tensor $g = h^T h$, such that the complete F can be written as

$$F = (f^{(\epsilon)}, gf_1, \dots, gf_N)^T\ . \tag{2.5}$$

There exist a large number of algorithms for finding minima of multi-variable functions if the first derivative is available. We favor the Broyden-Fletcher-Goldfarb-Shanno (BFGS) quasi-Newton scheme [48] for its stability and efficiency [49]. A recent review of this method is given in reference [50]. Like all quasi-Newton schemes, BFGS accumulates information about the Hessian matrix, and therefore about the shape of the enthalpy surface around the minimum. As we will show in Section 2.3, in many cases this allows to estimate the frequencies of zone-center optical phonons, elastic stiffness coefficients, and the bulk modulus.

Sufficiently close to a minimum X_{min}, the change in enthalpy $\delta\mathcal{H}$ can be approximated by:

$$\delta\mathcal{H} = \frac{1}{2}(X - X_{min}) \cdot A(X - X_{min}) \ . \tag{2.6}$$

In the vicinity of X_{min}, complete knowledge of the Hessian matrix A would allow us to find the exact (local) minimum X_{min} from the force F with one relaxation step. However, A is unknown. The key idea of the quasi-Newton schemes is to start with an initial guess for A, and improve on A successively as the relaxation proceeds. Actually, it is not A, but the inverse $H = A^{-1}$ which is being developed. In relaxation step $i + 1$, the previous position X_i is updated according to:

$$X_{i+1} = X_i + \lambda\Delta X_i \ , \tag{2.7}$$

$$\Delta X_i = H_i F_i \tag{2.8}$$

where F_i is F evaluated at X_i, and λ is the step length which is determined by an approximate line minimization along the step direction ΔX_i. The BFGS scheme takes as input an initial guess H_0 for H, and updates it according to

$$\begin{aligned} H_i &= H_{i-1} - \frac{(X_i - X_{i-1}) \otimes (X_i - X_{i-1})}{(X_i - X_{i-1}) \cdot (F_i - F_{i-1})} - \frac{(H_{i-1}(F_i - F_{i-1})) \otimes (H_{i-1}(F_i - F_{i-1}))}{(F_i - F_{i-1}) \cdot H_{i-1}(F_i - F_{i-1})} \\ &\quad + [(F_i - F_{i-1}) \cdot H_{i-1}(F_i - F_{i-1})]\, U \otimes U \ , \\ U &= \frac{(X_i - X_{i-1})}{(X_i - X_{i-1}) \cdot (F_i - F_{i-1})} - \frac{H_{i-1}(F_i - F_{i-1})}{(F_i - F_{i-1}) \cdot H_{i-1}(F_i - F_{i-1})} \ . \end{aligned} \tag{2.9}$$

If the enthalpy were perfectly quadratic in $X - X_{min}$, H_i would converge to A^{-1} after the number of relaxation steps has reached the number of degrees of freedom in the system [51]. More precisely, H_i and A^{-1} would not be identical, but have the same projection into the sampled subspace. The number of degrees of freedom equals the number of symmetry-compliant directions in configuration space, not counting rotations of the unit cell and an overall translation of the atoms. This amounts to the number of symmetric optical phonon modes at the Brillouin zone center Γ plus the number of lattice parameters.

In molecular dynamics schemes, one has to choose suitable fictitious masses and proper time steps to get fast convergence. The masses are normally determined by optimizing the dynamical coupling to the internal degrees of freedom during test runs [44]. Analogously, in the present quasi-Newton method, H_0 has to be initialized properly to assure a reasonable step size during the first few relaxation steps. It is important that H_0 does not break the symmetry when it is applied to a force vector F. Evidently, the dependence of the enthalpy on ϵ is governed by the elastic stiffness coefficients B_{ijkl} [52], or in a coarser sense, by the bulk modulus. Similarly, the optical phonon frequencies at Γ should determine the increase of the enthalpy upon displacement of the internal coordinates from the equilibrium positions.

With this in mind, we suggest to set the strain part of H_0 to the (9×9) identity matrix multiplied by $(3\Omega B_0)^{-1}$, B_0 being an estimate for the bulk modulus. Thus in the first step, the strain components of the search direction ΔX_0 will be parallel to $f^{(\epsilon)}$. For the internal coordinates, we propose to initialize H_0 as block diagonal with (3×3) matrices of the form $g_0^{-1}\bar{M}^{-1}\bar{\omega}_O^{-2}$, where $g_0 = h_0^T h_0$ is the metric tensor of the initial configuration, $\bar{M}$ is the average mass of the atoms, and $\bar{\omega}_O$ is a guess for the average of the optical phonon frequencies at the center of the Brillouin zone:

$$H_0 = \begin{pmatrix} (3\Omega B_0)^{-1} & & & & 0 \\ & \ddots & & & \\ & & (3\Omega B_0)^{-1} & & \\ & & & g_0^{-1}\bar{M}^{-1}\bar{\omega}_O^{-2} & \\ & & & & \ddots & \\ 0 & & & & & g_0^{-1}\bar{M}^{-1}\bar{\omega}_O^{-2} \end{pmatrix}. \tag{2.10}$$

The motivation for Eq. (2.10) will become more transparent when we discuss the extraction of elastic properties and optical phonon modes in Section 2.3. We show in section 2.5 that this initialization of H preserves the symmetry of the crystal during the relaxation. Note that (2.10) has only two "free" input parameters $\bar{\omega}_O$ and B_0, which makes it simple to use. There are certainly more sophisticated ways of choosing H_0, for instance with different values on the diagonal for the strain part, corresponding to strains for which the elastic stiffness coefficients are expected to differ substantially. However, this will only matter during the first few relaxation steps for a new structure. In the case that a similar relaxation has been done previously – for example the same structure, but at a different pressure – the fully built-up H of that calculation can be used with great benefit, as we will see in Section 2.4.3.

The line minimization required to find λ in Eq. (2.7) cannot be performed exactly, and one has to refrain to trial steps to find the minimum of $\mathcal{H}$ along the proposed search direction ΔX_i. It is often advantageous not to do any line minimization, and set $\lambda = 1$, because the increased number of relaxation steps required will be more than outweighed by the savings in force/stress evaluations for the line minimization. On the other hand, during the first few relaxation steps, the force F might be large due to a poor initialization of H, and an approximate line minimization is necessary to stabilize the algorithm. We find the following procedure a good compromise for several different systems. After a trial step with $\lambda = 1$, a linear fit to the forces F at $\lambda = 0$ and $\lambda = 1$ is performed. From the fit, we obtain λ_2 for which $\mathcal{H}$ should be minimal along ΔX_i. If λ_2 is smaller than 0.4 or larger than 1.6, we move by $\lambda_2 \Delta X_i$. Otherwise, we consider $\lambda = 1$ as sufficiently close to the minimum, and move by ΔX_i, thereby saving a force/stress computation. Once H is built up, the trial step with $\lambda = 1$ will be close enough to the minimum to omit the additional step with $\lambda = \lambda_2$.

In general there are several local minima in configuration space, and the algorithm can get trapped in one of those. In that sense, we present a method to relax forces and stress, *not* to find the structure for which the enthalpy is globally minimal. The location of the global enthalpy minimum still requires the intuition of a good starting point. The very same fact allows us to apply negative pressures, where the system could lower its enthalpy $\mathcal{H} = E - |p|\Omega$ arbitrarily by increasing the cell volume Ω. This indeed happens for strong negative pressures if the initial crystal structure is weakly bound, e.g. by Van der Waals forces. For moderate negative pressures, and crystals with ionic, metallic, or covalent bonds, this is not a problem though.

2.3 Optical phonon modes and elastic properties

Given a perfectly quadratic form of the enthalpy around the minimum, and assuming an exact line minimization, it can be shown [51] that H will converge to the inverse of the matrix A, and one would think that conversely a large amount of information about phonon frequencies and elastic properties can be extracted by analyzing H. However, the assumption of a quadratic form is only valid around the minimum, and we already mentioned that an accurate line minimization is expensive to do.

Also, the relaxation process might be converged long before the H-matrix is fully built up. This is especially true for a large number of degrees of freedom and if the initial configuration is close to the relaxed one. Even though it is often possible to extract information from an incomplete H, for simplicity we will assume that all degrees of freedom have been sampled.

Moreover, depending on the crystal structure, only a subspace of the full configuration space might be sampled during the relaxation process, since the crystal symmetry is preserved. Thus, we can only get the elastic properties for strains which do not break the symmetry, and the symmetry-preserving optical phonon modes at Γ. On the other hand, since isotropic scaling leaves the symmetry unchanged, the cell volume Ω is always a free parameter, and the bulk modulus is accessible irrespective of the crystal structure.

The extraction of information starts with manipulations of the H-matrix (cf. Eq. (2.9)) obtained from the last relaxation step. We first correct for the finite strain, which enters the force $f^{(\epsilon)}$ in Eq (2.3) in the form of a factor of $(1+\epsilon^T)^{-1}$. After defining the $(9+3N)\times(9+3N)$ matrix D as

$$D = \begin{pmatrix} (1+\epsilon) & & & & & 0 \\ & (1+\epsilon) & & & & \\ & & (1+\epsilon) & & & \\ & & & 1 & & \\ & & & & \ddots & \\ 0 & & & & & 1 \end{pmatrix} , \tag{2.11}$$

we arrive at the corrected $(9+3N)\times(9+3N)$ matrix

$$H' = D^{-1^T} H D^{-1} \ . \tag{2.12}$$

In Eq. (2.12), H is transformed from the coordinate system of the *initial* configuration h_0 to the coordinate system of the *relaxed* configuration h, such that H' describes the changes in enthalpy around the relaxed configuration.

We then restrict the strain around the relaxed configuration to be symmetric by projecting H' from the full (9×9) strain space to the smaller (6×6) strain space in Voigt notation, which leads to the $(6+3N)\times(6+3N)$ matrix H''.

Next we find out which directions in configuration space have been sampled by examining the update $H''_{update} = H'' - H''_0$, where H''_0 is obtained from H_0 the same way as H'' from H. The update H''_{update} has accumulated the step directions by means of the updating formula Eq. (2.9), and a singular value decomposition (SVD) of $H''_{update} = U \cdot w \cdot V^T$ (see [48]) yields a set of m orthonormal basis vectors of length $(6+3N)$ spanning the sampled subspace. We collect the basis vectors from the columns of U for which the corresponding diagonal elements of w are nonzero [48], into the columns of the $(6+3N)\times m$ matrix Y. Assuming that all directions in configuration space permitted by the symmetry constraints have been sampled, m is the number of degrees of freedom. In this case, we can choose the first m_ϵ basis vectors in Y to have components in the six-dimensional symmetric strain space only, and the other m_s basis vectors to be pure displacements of the internal coordinates. Thus we have a symmetric strain tensor $\epsilon^{(l)}$ for each of the strain-only basis vectors indexed by $l = 1, \ldots m_\epsilon$, and a set of atomic displacement vectors $s_i^{(k)}$, $i = 1, \ldots N$ for each of the other basis vectors $k = 1, \ldots m_s$. Such a decomposition is always possible, because the lattice degrees of freedom and those of the internal coordinates are independent of each other.

To determine the accessible elastic stiffness coefficients and phonon modes, it is convenient to write the distortion $\delta\epsilon$ and the atomic displacement vectors u_i, $i = 1, \ldots N$ (in Cartesian coordinates) as linear combinations of the basis vectors spanning the sampled subspace:

$$u_i = \sum_{j=1}^{m_s} \xi_j M_i^{-1/2} h s_i^{(j)} \ , \tag{2.13}$$

$$\delta\epsilon = \sum_{j=1}^{m_\epsilon} \zeta_j \epsilon^{(j)} \ . \tag{2.14}$$

Eqs. (2.13) and (2.14) define the reduced coordinates ξ and ζ. The mass M_i of the atom i in (2.13) simplifies the notation when the phonon modes are calculated later. For a compact matrix notation, we further introduce the $(6 + 3N) \times (6 + 3N)$ matrix

$$\mu = \begin{pmatrix} I_6 & & & & & & 0 \\ & M_1 & & & & & \\ & & M_1 & & & & \\ & & & M_1 & & & \\ & & & & M_2 & & \\ & & & & & \ddots & \\ 0 & & & & & & M_N \end{pmatrix} , \tag{2.15}$$

which has the (6×6) identity I_6 and the masses M_i on the diagonal. With the definitions given by Eqs. (2.13), (2.14) and (2.15), the Hessian matrix $\bar{A}$ in the reduced coordinates is

$$\bar{A} = \begin{pmatrix} \bar{A}^{(\epsilon)} & \bar{A}^{(\epsilon,s)} \\ \left(\bar{A}^{(\epsilon,s)}\right)^T & \bar{A}^{(s)} \end{pmatrix} = (Y^T \mu^{1/2} H'' \mu^{1/2} Y)^{-1} \ , \tag{2.16}$$

and the change of the enthalpy $\delta\mathcal{H}$ around the relaxed configuration (cf Eq. (2.6)) can be written as:

$$\delta\mathcal{H} = \frac{1}{2} \left(\sum_{i=1}^{m_\epsilon} \sum_{j=1}^{m_\epsilon} \zeta_i \bar{A}_{ij}^{(\epsilon)} \zeta_j + 2 \sum_{k=1}^{m_\epsilon} \sum_{l=1}^{m_s} \zeta_k \bar{A}_{kl}^{(\epsilon,s)} \xi_l + \sum_{p=1}^{m_s} \sum_{q=1}^{m_s} \xi_p \bar{A}_{pq}^{(s)} \xi_q \right) \ . \tag{2.17}$$

Eq. (2.17) gives the change in enthalpy if the internal coordinates, the unit cell shape, or both together are varied along the reduced coordinates. This information is contained in the matrices $\bar{A}^{(s)}$, $\bar{A}^{(\epsilon)}$ and $\bar{A}^{(\epsilon,s)}$, respectively.

2.3.1 Optical phonon modes

It is straightforward to extract the normal modes and frequencies of the symmetry-preserving optical phonons at Γ from $\bar{A}^{(s)}$. With a fixed unit cell shape, the enthalpy can be expressed in terms of the displacement vectors $u_i,\ i = 1, \dots N$ of the N atoms:

$$\delta\mathcal{H} = \frac{1}{2}\sum_{i,j=1}^{N} u_i^T \Phi^{(ij)} u_j, \tag{2.18}$$

where $\Phi^{(ij)}$ is the 3×3 matrix of force constants of second order [53] between atoms i and j. Its relation to the matrix $\bar{A}^{(s)}$ is

$$\bar{A}^{(s)}_{mn} = \sum_{i,j=1}^{N} (hs_i^{(m)})^T \frac{\Phi^{(ij)}}{(M_i M_j)^{1/2}} (hs_j^{(n)}) \ . \tag{2.19}$$

Thus $\bar{A}^{(s)}$ is the projection of the dynamical matrix at Γ into the subspace of symmetry-preserving displacement patterns.

To find the phonon modes and the frequencies, one substitutes (2.13) into the equations of motion for the phonons, and arrives at the generalized eigenvalue problem

$$(\omega^2 S - \bar{A}^{(s)})\xi = 0 \ , \tag{2.20}$$

where $S_{mn} = \sum_{i=1}^{N} (hs_i^{(m)})^T (hs_i^{(n)})$ is a symmetric overlap matrix between the basis vectors. The angular frequencies ω and the vectors ξ that solve Eq. (2.20) contain all the accessible information about the phonon modes. To get the displacement patterns of the phonon modes in Cartesian coordinates, we substitute the vector ξ into Eq. (2.13).

2.3.2 Elastic stiffness coefficients

A fully built-up H-matrix allows the computation of some linear combinations of the elastic stiffness coefficients B_{ijkl} for finite pressure [54] from Eq. (2.17). The B_{ijkl}'s describe how the enthalpy changes upon lattice distortions around the equilibrium configuration, assuming that the lattice distortion is accompanied by a relaxation of the internal parameters. We will now relate B_{ijkl} to $\bar{A}$, which gives the change of enthalpy along the reduced coordinates. It is not sufficient to just use $\bar{A}^{(\epsilon)}$, because the internal coordinates must be relaxed as the unit cell is deformed. The matrix $\bar{B}$ defined as

$$\bar{B}_{mn} = \bar{A}^{(\epsilon)}_{mn} - (\bar{A}^{(\epsilon,s)} \bar{A}^{(s)-1} \bar{A}^{(\epsilon,s)\,T})_{mn} \tag{2.21}$$

is the projection of B_{ijkl} into the subspace of symmetry-preserving, symmetric strains $\epsilon^{(j)},\ j = 1, \dots m_\epsilon$:

$$\Omega\, \epsilon_{ij}^{(m)} B_{ijkl} \epsilon_{kl}^{(n)} = \bar{B}_{mn} \ . \tag{2.22}$$

If m_ϵ is less than six, the knowledge of $\bar{B}$ in Eq. (2.21) does not allow one to recover all elastic stiffness coefficients B_{ijkl}. In this case, one can only get information about linear combinations of the elastic stiffness coefficients. However, the bulk modulus

$$B_0 = \left[\Omega \sum_{m,n=1}^{m_\epsilon} \mathrm{Tr}(\epsilon^{(m)}) (\bar{B}^{-1})_{mn} \mathrm{Tr}(\epsilon^{(n)})\right]^{-1} \tag{2.23}$$

can always be computed, since the cell volume Ω is a free parameter and guarantees $m_\epsilon > 0$.

2.4 Numerical tests

We show the efficiency of our method for three different silicon systems, treated within density functional theory (DFT) in the local density approximation (LDA) [15]. A norm-conserving pseudopotential [55] and a plane-wave basis set expansion up to an energy cutoff of 24 Rydbergs are used. Silicon is chosen because it is computationally simple, and because DFT in LDA is known to reproduce the experimentally observed structural parameters accurately [56], [57]. For the line minimization, we use the prescription outlined in Section 2.2.

2.4.1 Bulk modulus and phonon frequencies

The accuracy of our formulae for the bulk modulus Eq. (2.23) and the phonon frequencies Eq. (2.20) are tested by stretching the silicon bond in the two-atom cell of the diamond lattice along the (111) direction by 14% or 0.34 a.u. (1 a.u. $= 0.52918 \times 10^{-10}$m). This structure has three degrees of freedom: the angle between the lattice vectors, the bond length between the two atoms in the unit cell, and the cell volume. While for the starting configuration the angle is left at 60^o, we decrease the volume per atom from 131 to 120 a.u^3, and initialize H according to Eq. (2.10) assuming a bulk modulus of 500 GPa and an average phonon frequency of 8 THz. A Brillouin zone integration grid [37] of $8 \times 8 \times 8$ is used, and no external pressure is applied.

It takes 14 force/stress computations to reduce the stress and the forces to less than 10^{-3} GPa and 4×10^{-5} eV/a.u., respectively, thereby recovering the diamond structure. Using Eqs. (2.23) and (2.20), we compute the bulk modulus to be 90 GPa and the optical phonon frequency at Γ to be 15 THz. This is close to the 96 GPa and 15.4 THz obtained from the Murnaghan equation of state [58], and a traditional frozen-phonon calculation. We cannot expect perfect agreement because of the imperfect line minimization and the anharmonicity of the enthalpy surface at the starting point. However, the accuracy is good enough to yield a reasonable estimate, and provide insight into material properties. For example, when searching for hard materials [59], promising candidate structures can already be identified from the relaxation at ambient pressure, without going through the expensive computation of the equation of state.

2.4.2 Relaxation of a 16-atom silicon supercell

To assess the performance of the quasi-Newton algorithm for a larger system, we apply it to a 16-atom supercell of silicon in the diamond structure, where the atoms are randomly displaced from the equilibrium positions with an amplitude of 0.05 a.u. in all three spatial directions. After displacing the atoms, the tips of the lattice vectors are distorted randomly with an amplitude of 5%. Finally, the volume is increased from 131.8 to 143.75 a.u.^{3} per atom. The resulting crystal has only primitive translations as symmetry operations, resulting in $16 \times 3 - 3 + 6 = 51$ degrees of freedom to be optimized for. Brillouin zone integrations are performed on a $2 \times 2 \times 2$ grid [37]. No external pressure is applied. We initialize the H-matrix according to Eq. (2.10) with an estimated bulk modulus of 150 GPa and an average optical phonon frequency of 20 THz. Those differ intentionally from the 96 GPa and 15.4 THz of Section 2.4.1 in order to simulate realistic conditions, where the bulk modulus and the phonon frequencies are not known at the beginning of the calculation.

Fig. 2.1 shows how the average force, the "stress" $(\sum_{ij} \sigma_{ij}^2)^{1/2}$, and the error in the enthalpy δH decrease as the relaxation proceeds. Since there are 51 degrees of freedom, it will take at least 51 relaxation steps to build up H completely. Thus in most cases, it takes two force/stress computations per relaxation step to perform the approximate line minimization. For the last three relaxation steps, and also the following three steps not shown on the graph, an approximate line minimization is not necessary, indicating that H has improved.

2.4.3 Relaxation of the R8 phase of silicon

The R8 phase of silicon under pressure has been observed experimentally [46], and has been studied with *ab initio* calculations [60]. Its space group is $\mathrm{R}\bar{3}$ with eight atoms in the rhombohedral unit cell. Two of the atoms are located at the Wyckoff positions 2(c) (u, u, u), the other six are on the 6(f) (x, y, z) sites [46]. Including the unit cell volume Ω and the angle α between the rhombohedral lattice vectors, this structure has six degrees of freedom. It is thus a good example to show the performance of our method, because there are enough degrees of freedom to make a direct minimization impractical, and it is required that the symmetry of the crystal is preserved during the relaxation process. We use this test case also to demonstrate the benefits of a good starting guess for H.

We relax the R8 phase at several different pressures p, starting with $p = 8.2$ GPa, for which the experimentally observed parameters [60] are $\Omega = 902$ a.u.^{3}, $\alpha = 110.07^0$, $u = 0.2922$, $x = 0.4597$, $y = -0.0353$, and $z = 0.2641$. A $6 \times 6 \times 6$ grid [37] is used for the Brillouin zone integrations. The H-matrix is initialized assuming a bulk modulus of 100 GPa, and optical phonon frequencies of 15 THz. It takes 10 relaxation steps with a total of 16 force/stress computations to reduce the forces to less than 10^{-4} eV/a.u., and converge the components of the stress tensor to better than 10^{-3} GPa. At the relaxed position, for $p = 8.2$ GPa, we find the computed structural parameters to be $\Omega = 861$ a.u.^{3}, $\alpha = 109.99^0$, $u = 0.280$, $x = 0.462$, $y = -0.034$, and $z = 0.269$.

Starting with the computed parameters at 8.2 GPa, we increase the pressure to 16 GPa, and then to 24 GPa, relaxing after each increase in pressure. Analogously, we decrease the pressure from 8.2 GPa to 0 GPa, and from there to -8 GPa. Fig. 2.2 shows how the cell volume changes during the relaxation processes. We perform the calculations with two different initializations of H: one initialized according to Eq. (2.10) with $B_0 = 100$ GPa, $\bar{\omega}_O/(2\pi) = 15$ THz (shown as triangles), and the other one (squares) taken from the fully built-up H of the previous pressure. For example to compute the square-marked curve from 8.2 GPa to 0 GPa, the final H obtained from the relaxation at 8.2 GPa is used. The convergence criterion is such that the forces are smaller than 10^{-4} eV/a.u., and the stress is accurate to better than 10^{-3} GPa.

Fig. 2.2 shows the advantage of a superior initialization of H. Obviously, the H-matrix does not change too much with pressure, and carrying over H from a relaxation at a similar pressure cuts down the computational effort by half. Not only does a better H-matrix result in more efficient step directions, it also saves the line minimization, because the trial step of length $\lambda = 1$ in Eq. (2.7) is already sufficiently close to the minimum. With the superior starting guess for H, we find convergence after eight or fewer force/stress computations.

An analysis of H for $p = 0$, gives a bulk modulus of 95 GPa for the R8 structure, compared to 89 GPa from the Murnaghan equation of state [58]. Using Eq. (2.20), the frequencies for the symmetry-preserving A_g phonon modes at the Brillouin zone center are 4.0, 9.7, 10.7, and 14.1 THz.

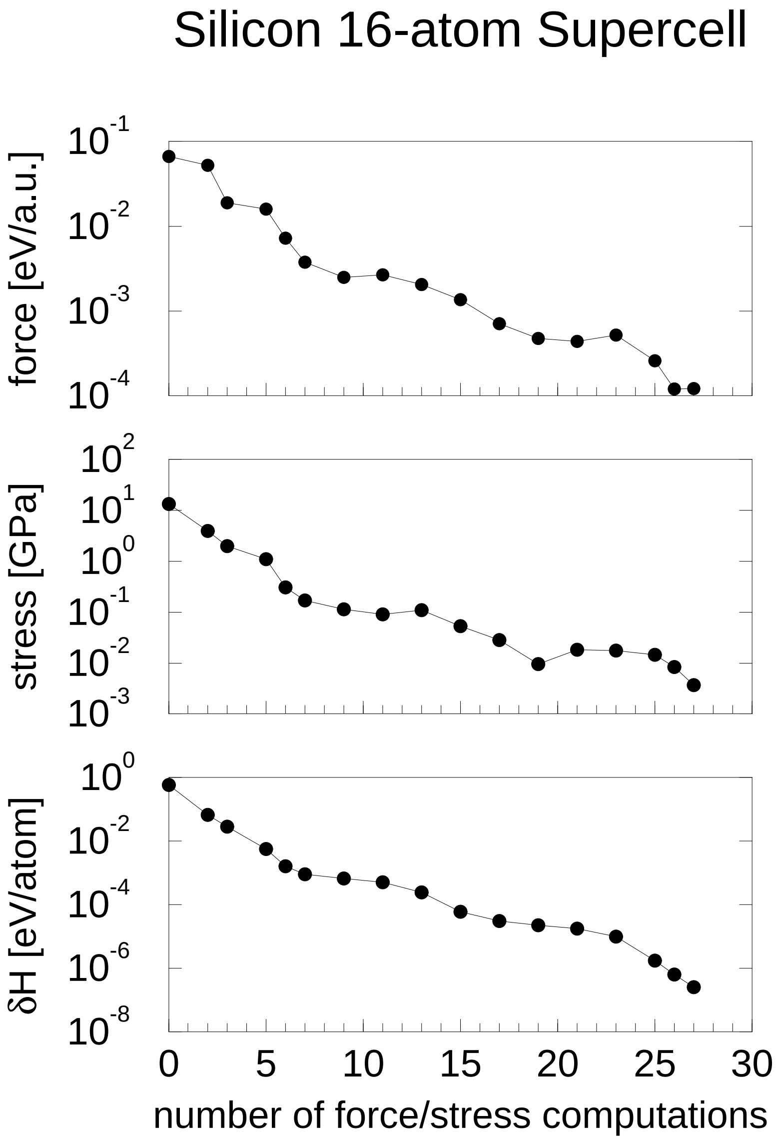

Figure 2.1: Relaxation of the 16-atom silicon supercell. The atoms and the unit cell vectors have been randomly displaced from the perfect diamond structure, resulting in a system with 51 degrees of freedom. The average force, the “stress” $(\sum_{ij} \sigma_{ij}^2)^{1/2}$ and the error in the enthalpy δH are shown as a function of the number of force/stress computations. Each symbol represents a relaxation step, and most of the time it needs two force/stress computations to perform a relaxation step because of the line minimization.

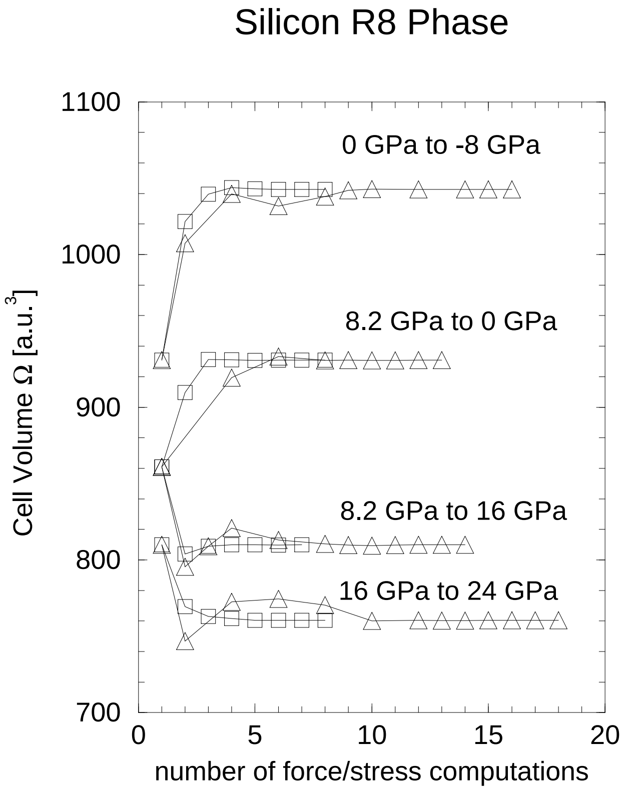

Figure 2.2: Relaxation of the R8 phase of silicon, which has a total of six degrees of freedom. One of them – the unit cell volume – is shown as a function of the number of force/stress computations for relaxations at different pressures. Starting from the relaxed structural parameters obtained at 8.2 GPa, relaxations at 0 GPa and and 16 GPa are performed. In the same way, relaxations from 0 GPa to -8 GPa, and from 16 GPa to 24 GPa are carried out. The triangles show how the volume develops if H is initialized with $B_0 = 100$ GPa and $\omega_O/(2\pi) = 15$ THz. The relaxation is about twice as efficient if the H matrix of the starting point is used (squares). Each symbol represents a relaxation step, but with the inferior initialization of H (triangles), it often takes several force/stress computations per relaxation step, because the approximate line minimization has to be performed. This is especially the case during the first few relaxation steps, when H is not built up yet.

2.5 Symmetry conservation

In this section, we show that a relaxation with the BFGS scheme as outlined in Section 2.2 indeed preserves the symmetry of the crystal if H is properly initialized (2.10).

Let us first examine how a symmetry-compliant point X in configuration space must transform under a crystal symmetry operation $\{\alpha|\tau\}$, α being a unitary mirror-rotation matrix, and τ a non-primitive translation vector. The first nine components of X are just the strain components ϵ, which have to remain invariant under the point symmetry operations:

$$\epsilon' = \alpha^{-1}\epsilon\alpha = \epsilon \tag{2.24}$$

if the symmetry should be preserved. The other components of X are the positions s_i of the atoms in lattice coordinates, and they transform according to

$$s_i' = (h^{-1}\alpha h)\ s_i + h^{-1}\tau\ . \tag{2.25}$$

Since the symmetry operation $\{\alpha|\tau\}$ leaves the crystal invariant, it is always possible to find the permutation matrix P_{ij} which gives the index of the atom j into which atom i has been mapped:

$$s_i' = \sum_j P_{ij} s_j\ . \tag{2.26}$$

If the components of a configuration space point transform according to Eqs. (2.24) and (2.26), we shall call it *symmetric*.

The derivative F of the enthalpy with respect to X in Eq. (2.5) is *not* symmetric, but the step direction $\Delta X = HF$ is, as we will show below. The first nine components $f^{(\epsilon)}$ of F are invariant under point symmetry operations according to Eqs. (2.3) and (2.5). The force f_i in lattice coordinates transform like the positions in Eq. (2.26):

$$f_i' = \sum_j P_{ij} f_j\ , \tag{2.27}$$

and is symmetric, but it is gf_i which forms the components of F, and this entity is not symmetric.

To show that ΔX is indeed symmetric at each step, we first notice that H can be decomposed into

$$H = H_0 + H^{(update)}\ , \tag{2.28}$$

where the $H^{(update)}$ is the sum of all updates (2.9). For HF to be symmetric, it is sufficient that the product of H_0 with the force vector F is symmetric. Given that, $H^{(update)}F$ will be a linear combination of symmetric vectors by virtue of the updating formula given by Eq. (2.9), and so will be HF.

It remains to show that H_0F is always symmetric for our choice of H_0. According to Eq. (2.10), the stress components of F do not mix with the force components, nor do the forces on different atoms mix with each other when H_0 is applied. Since we initialize the strain components of H to be a multiple of the identity matrix, the strain part of H_0F will trivially be symmetric. So are the atomic-position components Δs_i of H_0F, as we see from their transformation behavior under a symmetry operation $\{\alpha|\tau\}$. Because $h^{-1}\alpha h$ commutes with $g_0^{-1}g$, we have

$$\Delta s_i' = h^{-1}\alpha h \bar{M}^{-1}\bar{\omega}_O^{-2}(g_0^{-1} g f_i) = \sum_j P_{ij}\bar{M}^{-1}\bar{\omega}_O^{-2} g_0^{-1} g f_j = \sum_j P_{ij}\Delta s_i\ , \tag{2.29}$$

and hence H_0F is symmetric.

2.6 Conclusion

In conclusion, an efficient quasi-Newton algorithm is proposed to simultaneously relax the internal coordinates and lattice parameters of a crystal while preserving its symmetry. As a byproduct, elastic properties and some of the optical phonon modes can be estimated. The efficiency of the quasi-Newton method is demonstrated for silicon in a 16-atom diamond supercell and the R8 phase.

Chapter 3

Silicon in the R8 structure

3.1 Introduction

The technological importance of silicon has motivated much work on its high-pressure phase diagram. Upon compression to about 10-12.5 GPa [61, 62, 63, 64], silicon transforms from the diamond structure (Si I) to the metallic β-Sn phase (Si II). When unloaded, it does not convert back to the diamond phase, but assumes the BC8 structure (Si III), a body-centered cubic phase with an eight-atom basis [61], which is metastable at ambient pressure. Annealing of BC8 silicon produces yet another metastable form of silicon, which is of the hexagonal diamond type [61] (Si IV). On very fast pressure release from 12 and 15 GPa to ambient pressure, two other metastable phases with tetragonal symmetry have been reported [65] (Si VIII and Si IX), although their structure could not be completely determined. At pressures above $\sim$ 13 GPa [63], the β-Sn phase is distorted to the Imma structure (Si XI) [66], which connects the β-Sn phase continuously with the simple hexagonal Si V observed at $\sim$ 16 GPa [62, 63]. When applying even higher pressures, silicon assumes a yet unidentified structure [62, 67, 68] at $\sim$ 38 GPa (Si VI) before it converts to the hexagonal close-packed Si VII at $\sim$ 42GPa [68]. Finally, at a pressure of $\sim$ 79 GPa, silicon is found to be in the face-centered cubic structure [67, 68] (Si X).

Recently, with silicon XII another metastable phase has been discovered [46, 60] and has been named R8, because of its rhombohedral lattice with eight atoms in the basis. The present chapter will focus mostly on this phase, and discuss its structural and electronic properties in comparison with the closely related BC8 phase. We repeat and extend a previous *ab initio* study by Piltz *et al.* [60], but find significant discrepancies regarding the zero-pressure volume and energy of R8. Attention will be devoted to the density of states (DOS) of the R8 phase, as it is the first crystalline silicon phase with five-membered rings, which have been predicted to affect the electronic properties [69].

3.2 Structures

All of the structures addressed here have already been described previously [60, 70]. Therefore, we will focus on those structural features which are relevant in the present context.

The diamond structure O_h^7 (Fd3m) has an fcc lattice with a two-atom basis at the Wyckoff 8(a) positions. Each atom is surrounded by four equidistant neighbors at the corners of a regular tetrahedron. A tetragonal distortion transforms the diamond structure into the β-Sn structure, which has a body-centered tetragonal unit cell (space group D_{4h}^{19} (I4/amd)) with a two-atom basis on the 4(a) positions. At a pressure of 10.3 GPa, the unit cell parameters are [66] a=4.665(1) Å, c=2.572(1) Å. Each atom has four nearest neighbors at 2.42 Å, and two second-nearest neighbors at an only slightly larger distance of 2.57 Å. The angles between the bonds to the four nearest neighbors are 149^0 and 94^0, largely deviating from the ideal tetrahedral angle of 109.47^0.

Fig. 3.1 shows the more complex BC8 phase. It has a bcc lattice with an eight-atom basis located

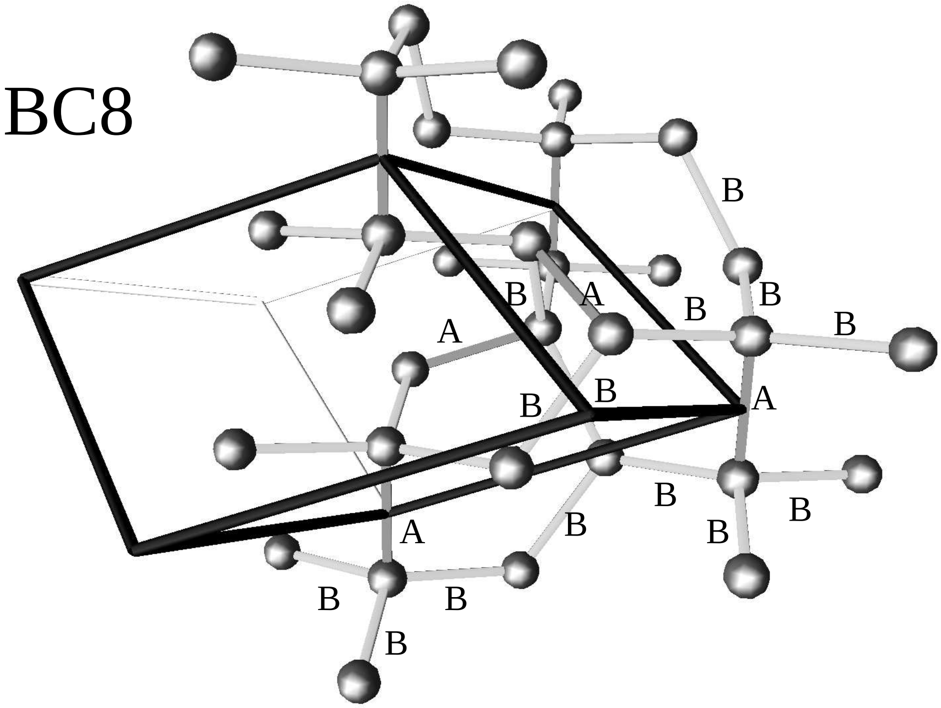

Figure 3.1: Ball and stick model of the BC8 phase of silicon. The primitive unit cell for the bcc lattice is shown with bold lines. At its corners, a basis with the shape of a vertically oriented ethane molecule is attached. The two different bond lengths are labeled A and B.

at the 16(c) sites, and is classified by the space group T_h^7 (Ia$\bar{3}$). We can think of the structure as composed of building blocks with the shape of ethane molecules. The crystal structure is obtained by attaching this building block to the bcc lattice vertices, oriented in the (111) direction. In Fig. 3.1 the bcc primitive unit cell is shown, with the basis attached to only four of the eight corners of the unit cell in order to avoid cluttering. Due to the high symmetry of the structure, there is only one internal degree of freedom, which is the parameter x_0 for the atoms at the 16(c) sites. At ambient pressure, it is measured to be [60] $x_0 = 0.1003(8)$. Fig. 3.1 also shows the two distinct bond lengths labeled A and B following Biswas *et al.* [70]. At ambient pressure, experiment [60] finds the A bond (2.31Å) to be significantly shorter than the B bond (2.39Å). The angle between two B bonds is 117.6^0, whereas the AB angle is 99.0^0. Both angles differ substantially from the ideal tetrahedral angle of 109.47^0.

The R8 structure (Fig. 3.2) is characterized [46] by the space group C_{3i}^2 (R$\bar{3}$). The angle α between the basis vectors of the rhombohedral lattice is [60] $110.07(3)^0$, which brings the lattice very close to the bcc lattice of the BC8 structure, where α=109.47^0. Due to the reduced symmetry, R8 has four parameters specifying the eight-atom basis. At a pressure of 8.2 GPa they are [60] $u = 0.2922(9)$ for the atoms at the 2(c) site, and $x = 0.4597(8)$, $y = -0.0353(7)$, $z = 0.2641(7)$ for

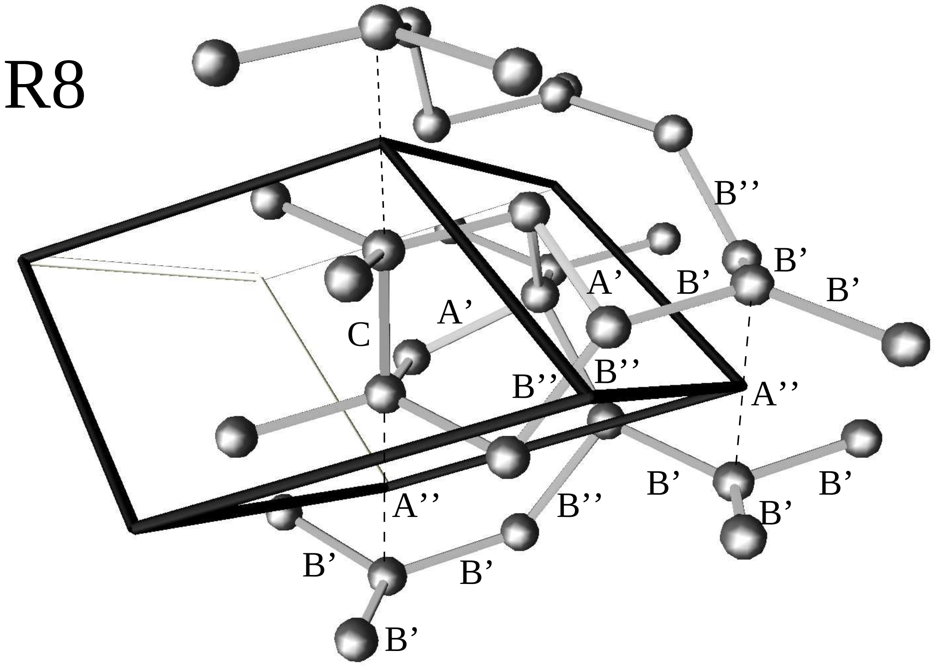

Figure 3.2: Ball and stick model of the R8 phase of silicon. The R8 phase has a rhombohedral unit cell which is a slightly distorted bcc cell. The four distinct bond lengths are labeled A', B', B", and C. One can go from BC8 to R8 by breaking the central bond of the BC8 basis, and reconnecting it along the dashed lines (labeled A") with the next basis unit along the *c* axis, resulting in the C bond.

the atoms at the 6(f) sites. Notice that the R8 phase coincides with BC8 if we choose $\alpha = 109.47^0$, $u = 2x_0$, $x = 0.5$, $y = 0$, and $z = 0.5 - 2x_0$. We label the four distinct bonds of the R8 structure with A$'$,B$'$,B$''$ and C. A range of bond angles is present. About the 2(c) site, the bond angles are 117.9^0 and 98.5^0, whereas the 6(f) atoms see bond angles of 92.1^0, 93.0^0, 103.1^0, 105.0^0, 114.9^0, and 136.8^0. The BC8 and R8 phases are related in a simple way, as can be seen from Figs. 3.1 and 3.2. To convert from BC8 to R8, one merely has to break the A bond of each BC8 building block, and reconnect it in the opposite direction to form the C bond in the R8 phase (see Fig. 3.2). We can see that the A$'$ bond of R8 is reminiscent of the A bond of BC8, and likewise B$'$ and B$''$ in R8 correspond to the B bond of BC8. This fact will become important when we compare the structural properties of the two phases. The distance labeled A$''$ (shown with a thin, dashed line in Fig. 3.2) originates from a BC8 A bond, but has now become a second-nearest neighbor distance in the R8 phase.

3.3 Method

Our *ab initio* calculations are done within the framework of density functional theory (DFT) in the local density approximation (LDA) using the parameterization of the Ceperley-Alder functional [15] by Perdew and Zunger [16]. The interaction of the valence electrons with the ionic cores is represented with a separable [71], norm-conserving, nonlocal Troullier-Martins [55] pseudopotential. We expand the wave functions in plane waves [39] up to a cutoff energy of 24 Rydbergs. For sampling the Brillouin zone, Monkhorst-Pack [37] grids of the following sizes are used: $8 \times 8 \times 8$ for the diamond phase, $10 \times 10 \times 10$ for β-Sn , and $6 \times 6 \times 6$ for BC8 and R8. With these parameters, the total energy is accurate to better than 0.2 mRy per atom. For all structures considered, the internal degrees of freedom as well as the lattice parameters are relaxed simultaneously with the quasi-Newton method [72] described in chapter 2.

3.4 Stability of four-fold coordinated phases of silicon

Fig. 3.3 shows the results of our DFT-LDA total energy calculations. Plotted is the enthalpy difference in Rydbergs per atom with respect to the diamond phase as a function of pressure. When the pressure exceeds 8.5 GPa, the β-Sn phase becomes lower in enthalpy than the diamond phase. Diamond anvil cell experiments find this transition to happen at a pressure of about 10 to 12.5 GPa [61, 62, 63, 64]. The transition pressure we find is in agreement with recent all-electron calculations (8.0 GPa) [73], and other pseudopotential plane-wave calculations (7.8 GPa) [74], (8.4 GPa) [75]. Since the experiments only measure the transition upon compression, any hysteresis will bias the observed transition pressure to larger values. A more detailed discussion and assessment of the accuracy with which the present theory reproduces this phase transition can be found in references [73] and [74].

A direct β-Sn to diamond transition upon decompression is not observed in experiment, but rather a conversion to the R8 phase at pressures of about 8.2-10.1 GPa [46, 60]. Our calculations predict this transition at 7.4 GPa.

In experiment [46], the R8 phase transforms reversibly to the metastable BC8 structure at ~ 2 GPa. From Fig. 3.3, we can see that the pressure dependence of the enthalpy of the two phases is very similar. Using a fit to the Murnaghan equation of state [58], we find the bulk modulus of the R8 phase to be 89 GPa, which is close to the 92 GPa we calculate for BC8. The similar bulk moduli and the small differences in volume between the R8 and the BC8 phase make it difficult to determine the transition pressure from our calculation. The enthalpy curves of R8 and BC8 in Fig. 3.3 cross at -1.9 GPa. However, an inaccuracy of only 1 mRy/atom in our enthalpy calculation would make the computed transition pressure vary by about 9 GPa. The convergence with respect to the k-point mesh for the enthalpy of the BC8 and R8 phases is accurate to 0.05 mRy/atom. When using different pseudopotentials, we see the enthalpy differences between R8 and BC8 vary by 0.15 mRy/atom. Even though an accurate determination of the transition pressure is not possible, we note that the qualitative behavior is correct: on decompression β-Sn first transforms to R8, and then to BC8. Despite the small enthalpy differences between the two phases, the transition need not show a large hysteresis. This is because the transformation can be accomplished by breaking only one out of 16 bonds.

The quasi-Newton scheme we use to relax the structure yields information about phonon frequencies at the Γ point [72]. At all pressures, we find R8 and BC8 to have purely real phonon

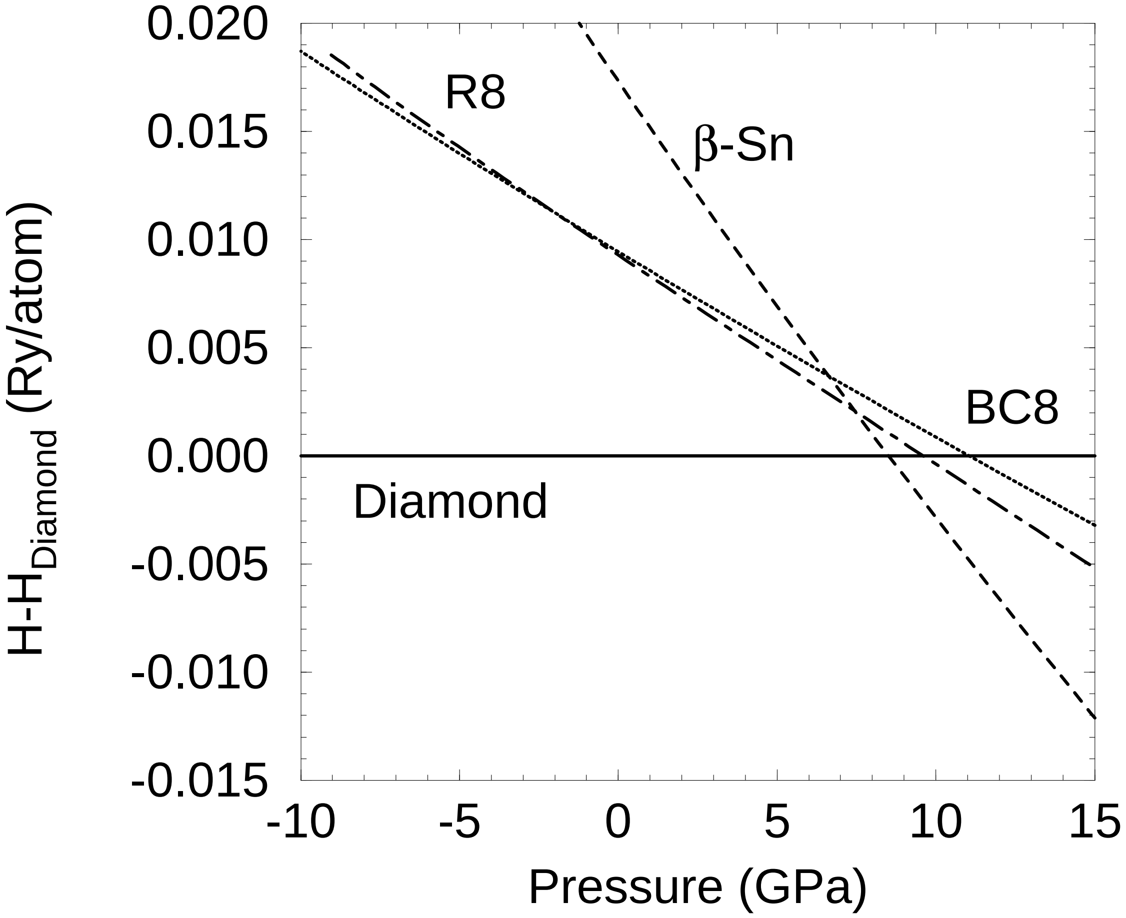

Figure 3.3: Enthalpy (in Rydbergs) of tetrahedral phases of silicon as a function of pressure (in GPa). The enthalpy is given with respect to the diamond phase. Above 8.5 GPa the β-Sn phase is more stable than the diamond phase. BC8 and R8 are both unstable, and have a very similar bulk modulus. At higher pressure, R8 is more stable, whereas at lower pressures, BC8 is favored. The calculated transition pressure between β-Sn and BC8 is 7.4 GPa.

frequencies and therefore they are locally stable. In other words there is a persistent energy barrier between the two phases. Therefore, the phase transition is of first order, in agreement with experiment [60]. A softening of the optical phonon modes at Γ is not found within the pressure range studied.

3.5 Structural properties of the BC8 and R8 phase

In the present section, we will discuss the structural properties of the R8 and BC8 phases of silicon, focusing especially on the variation of the structure when external pressure is applied.

In Fig. 3.4, we show the dependence of the crystal lattice parameters of the R8 and BC8 phase as a function of pressure. The experimental data points are from Piltz *et al.* [60]. We find good agreement between theory and experiment. The phase transition from BC8 to R8 is of first order, and is accompanied by a discontinuous change in volume. Although our calculations yield an overall underestimation of the volume as it is typical for LDA calculations [76], we find good agreement for the volume differences. With respect to the density at the phase transition, we compute the R8 phase to be denser by 1.2%, which is a rather small change, and is close to the 2.1% determined by X-ray diffraction [60]. The agreement is even better if we take into account that, due to the limited X-ray intensity and the few lines observed, the volume of the R8 phase is uncertain by about ±0.7%. Our findings are in disagreement with previous DFT/LDA calculations [60], where the jump in volume appears to be about 7%.

The equations of state of BC8 and R8 in Fig. 3.4 are similar because equilibrium volume and the bulk moduli are similar. This is not surprising, since BC8 can be obtained from R8 by breaking and reconnecting only one out of 16 bonds. Moreover, both phases have a comparable density and are characterized by distorted sp^3-type bonding.

Also in agreement with experiment [60], we find the rhombohedral angle α to open as the pressure on the R8 phase is increased (Fig. 3.4). By opening α, the second-nearest neighbor distance A$''$ between the atoms on the 2(c) sites is decreased, bringing them closer to a five-fold coordination. However, even at a pressure of 8.2 GPa, the calculated second-nearest neighbor distance is about 30% larger than the nearest neighbor distance, and the system is clearly four-fold coordinated.

Fig. 3.5 shows the change of the R8 internal parameters u, x, y and z as a function of pressure. Good agreement between theory and experiment [60] is observed for x,y, and z (experiment [60] at 8.2 GPa: $x = 0.4597(8)$, $y = -0.0353(7)$, $z = 0.2641(7)$). The computed u however is smaller by 4% than the $u = 0.2922(9)$ found in experiment. Within the $\sim 2-10$ GPa stability range of the R8 phase, the variation of the internal parameters is comparable to the experimental uncertainty in the published intensity data [60], and will be difficult to observe. At elevated pressure, the u parameter related to the second-nearest neighbor distance A$''$ ceases to change, along with the rhombohedral angle α. This means that upon pressure increase, at lower pressures the second-nearest neighbor distance decreases strongly to facilitate the volume reduction, while above 10 GPa, it merely reduces according to an isotropic volume scaling.

To get a better understanding of the behavior of the R8 phase under compression, we plot in Fig. 3.6 the various bond lengths as a function of pressure. Evidently, those R8 bonds which are reminiscent of the BC8 bonds behave like their counterparts. Under pressure, the A$'$ bond of R8 resembles the A bond of BC8, and so do the B$'$ and B$''$ bonds mimic the B bond. The C bond on the other hand behaves rather differently. Under compression, it changes little while the pressure is below about 10 GPa. In this pressure region, most of the volume reduction is accomplished by

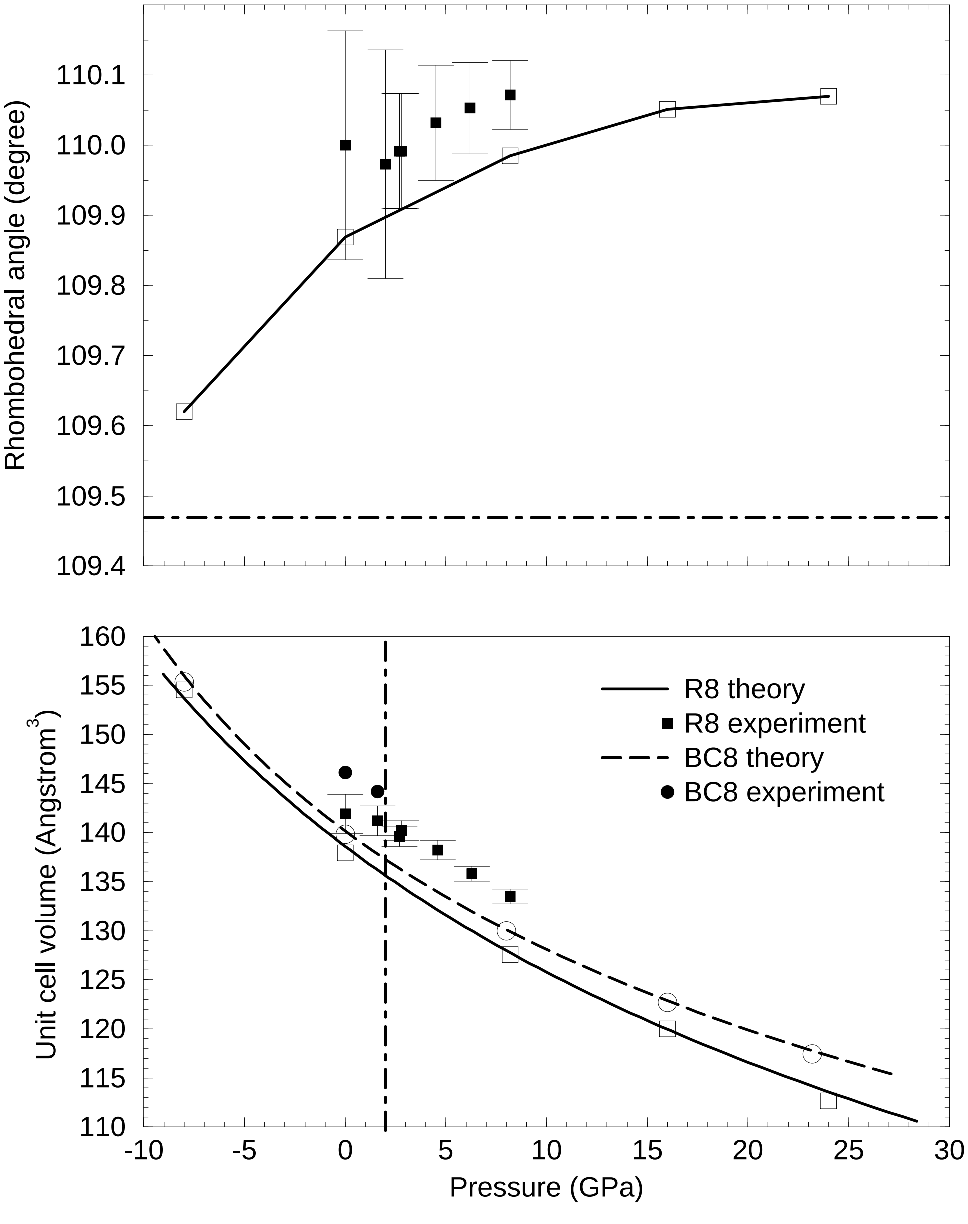

Figure 3.4: Volume and rhombohedral angle α of the silicon R8 and BC8 phases as a function of pressure. The experimental data points for R8 (solid squares) and BC8 (bullets) are from Reference [60]. The theoretical data points (open symbols) for the volume are connected with a fit to the Murnaghan equation of state, whereas for the rhombohedral angle, the line is a guide for the eyes only. The rhombohedral angle of BC8 is fixed by symmetry to 109.47^0.

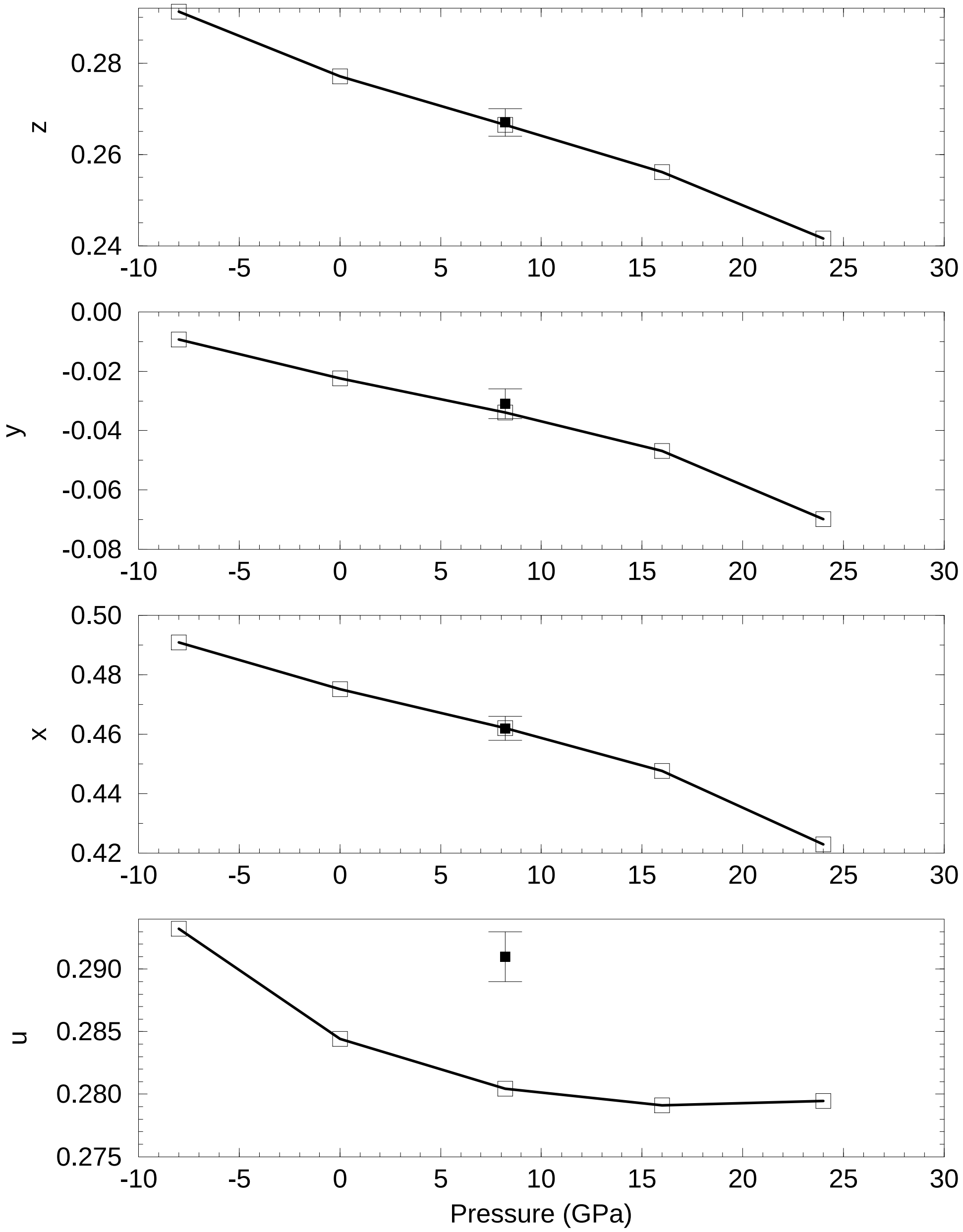

Figure 3.5: Internal degrees of freedom of R8 silicon as a function of pressure. The coordinates of the 2(c) atoms relative to the lattice vectors are (u, u, u), while the 6(f) atoms are located at (x, y, z). The experimental data points are from Reference [60].

diminishing the second-nearest neighbor distance A''. When reaching higher pressure, this process stops, and the C bond starts to shorten.

3.6 Electronic properties of the BC8 and R8 phases

Already the discoverers [46] of the R8 phase pointed out the presence of five-membered rings, and indicated that they should affect the electronic properties of the R8 phase [69]. While silicon in the BC8 phase is known to be semi-metallic [77], the electrical properties of R8 have not been measured yet. In this section, we will extend the *ab initio* study of the electronic structure done previously [60].

Fig. 3.7 shows the DFT/LDA band structures of silicon in the R8 and BC8 phases at zero pressure with the relaxed structural parameters from our calculation. For ease of comparison, both are plotted in the rhombohedral Brillouin zone (BZ) shown in the inset. In agreement with experiment [77], we find BC8 to be a semi-metal, with a direct band overlap of 0.8 eV at the rhombohedral T point, which is the H point in the bcc BZ. Turning to the R8 band structure, we see the most interesting changes occuring around the T point. Here the threefold degeneracy at the top of the BC8 valence band is split into a doublet and a singlet, and no direct band overlap is found in R8. Rather, in the R8 phase there is a small indirect band overlap between the T and L point of about 0.3 eV. This is somewhat less than the 0.5eV found by Piltz *et al.* [60]. It is important to mention that LDA tends to predict too small gaps in most semiconductors. For silicon in the diamond structure, an indirect gap of 0.52 eV is found, compared to 1.17 eV from experiment [78]. An accurate prediction of the metallicity of R8 silicon would require for instance a quasiparticle energy calculation [78]. Thus, although we find R8 silicon to be a semi-metal, it could well be a small-gap semiconductor.

Model calculations on a tetrahedrally bonded fictitious phase of silicon with five-membered rings have revealed a number of interesting properties [69] of the density of states (DOS). The most striking feature is a sharpening of the valence band edge, as it is seen in amorphous silicon. In Table 3.1 we list the ring count for the diamond, BC8 and R8 structure. On the average, an R8 atom is participating in $3\frac{3}{4}$ five-membered rings. We show in Fig. 3.8 the DOS for BC8 and R8 as computed within LDA, using the relaxed structural parameters from our calculation. It is interesting to see that indeed the DOS of R8 (solid line) shows a sharper valence band edge than that of BC8 (dashed line). With respect to BC8, apparently weight is transferred from the high peak at -2.3 eV (Region 2) to the top of the valence band (Region 3) at around -1.5 eV. The peak at -2.3 eV has been attributed [69] to the wurtzite-like eclipsed tetrahedral units present in BC8. In fact, when R8 is formed from BC8 by the rebonding process discussed earlier, eclipsed tetrahedral units involving the 2(c) atoms get converted into strongly distorted staggered diamond-like configurations.

To gain a better understanding of some of the features in the R8 DOS, we examine the charge density contributions from the states in the Regions 1, 2, and 3 marked with boxes in Fig. 3.8. We find the states in Region 1 to be more localized between the 2(c) atoms, where they form an s-type bond. This is also evident from the local and angular-momentum resolved DOS shown in Figs. 3.9 and 3.10 for the 2(c) and 6(f) atoms, respectively. There, the peak in Region 1 is stronger on the 2(c) than on the 6(f) site, and has mainly s character. Region 3, on the other hand, is predominantly p-type, and the states here have also most of their amplitude between the 2(c) atoms. This is consistent with our examination of the charge contributions originating from states in Region 3. To make sure that this is not an artifact of using the LDA-relaxed structure, we repeated our analysis

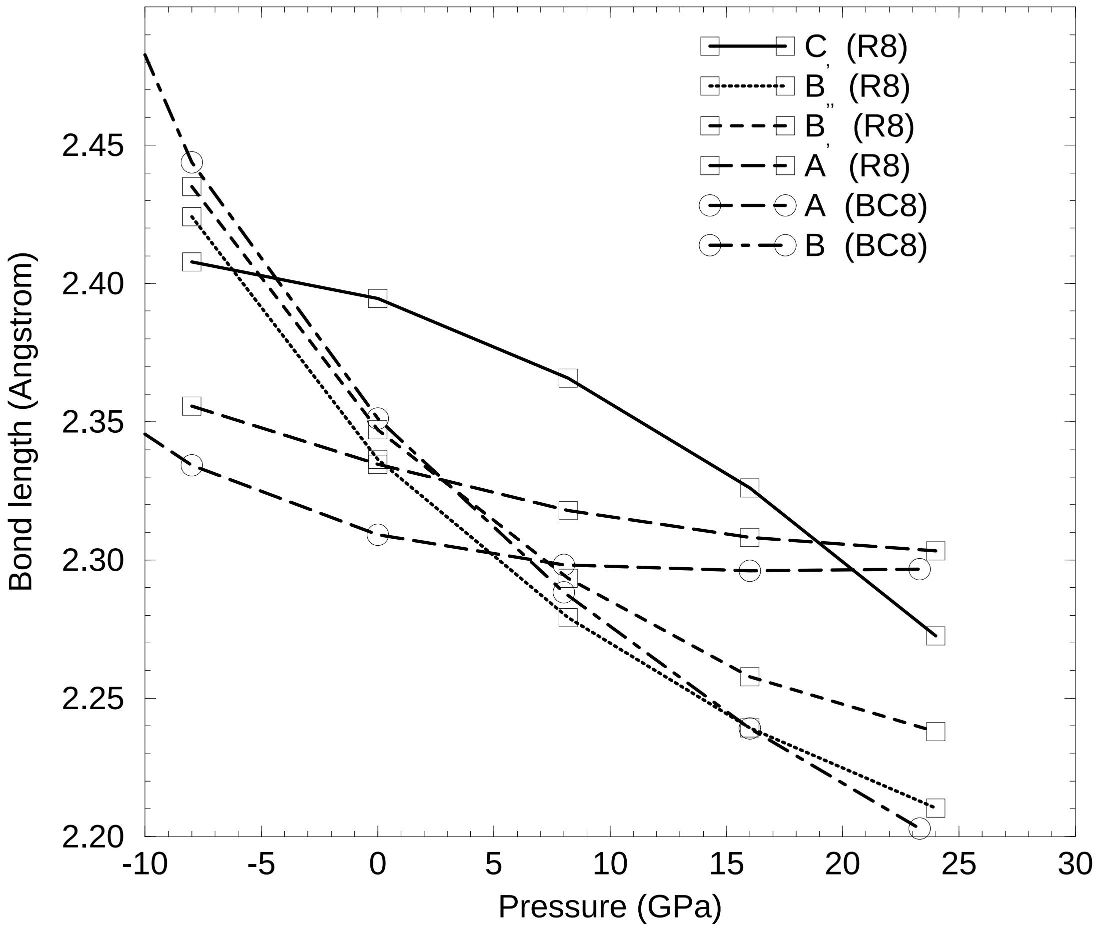

Figure 3.6: The bond lengths of the R8 and BC8 structures as a function of pressure. The squares indicate R8 bond lengths; the circles mark BC8 bonds. R8 has four distinct bond lengths labeled C (solid line), B′ (dotted), B″ (dashed), and A′ (long dashed). Also shown are the two bond lengths present in the BC8 phase, labeled A (long dashed) and B (dot-dashed). For labeling of the bonds see Figs. 3.1 and 3.2.

structure	atoms/cell	5-memb.	6-memb.	8-memb.
diamond	2	0	12	24
BC8	8	0	9	36
2(c) atom of R8	2	6	3	21
6(f) atom of R8	6	3	5	25
R8 (average)	8	$3\frac{3}{4}$	$4\frac{1}{2}$	24

Table 3.1: The number of five-, six-, and eight-membered rings per atom is shown in the last three columns. Seven-membered rings are absent in all of the structures considered here. The R8 phase is the only one with five-membered rings. There, each 2(c) atom is included in twice as many five-membered rings as a 6(f) atom.

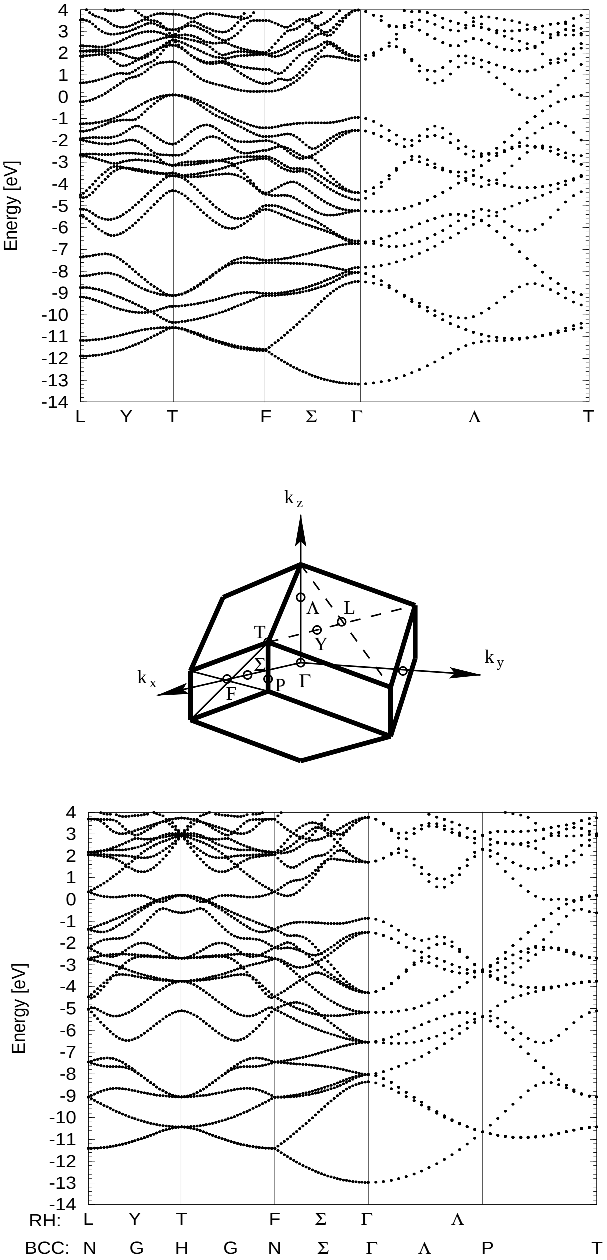

Figure 3.7: Band structure of silicon in the R8 phase (top graph) and the BC8 phase (bottom graph). The structural parameters are from our calculation at zero pressure. To facilitate comparison, both band structures are plotted along special lines in the rhombohedral BZ. Note the characteristic differences in the vicinity of the T point.

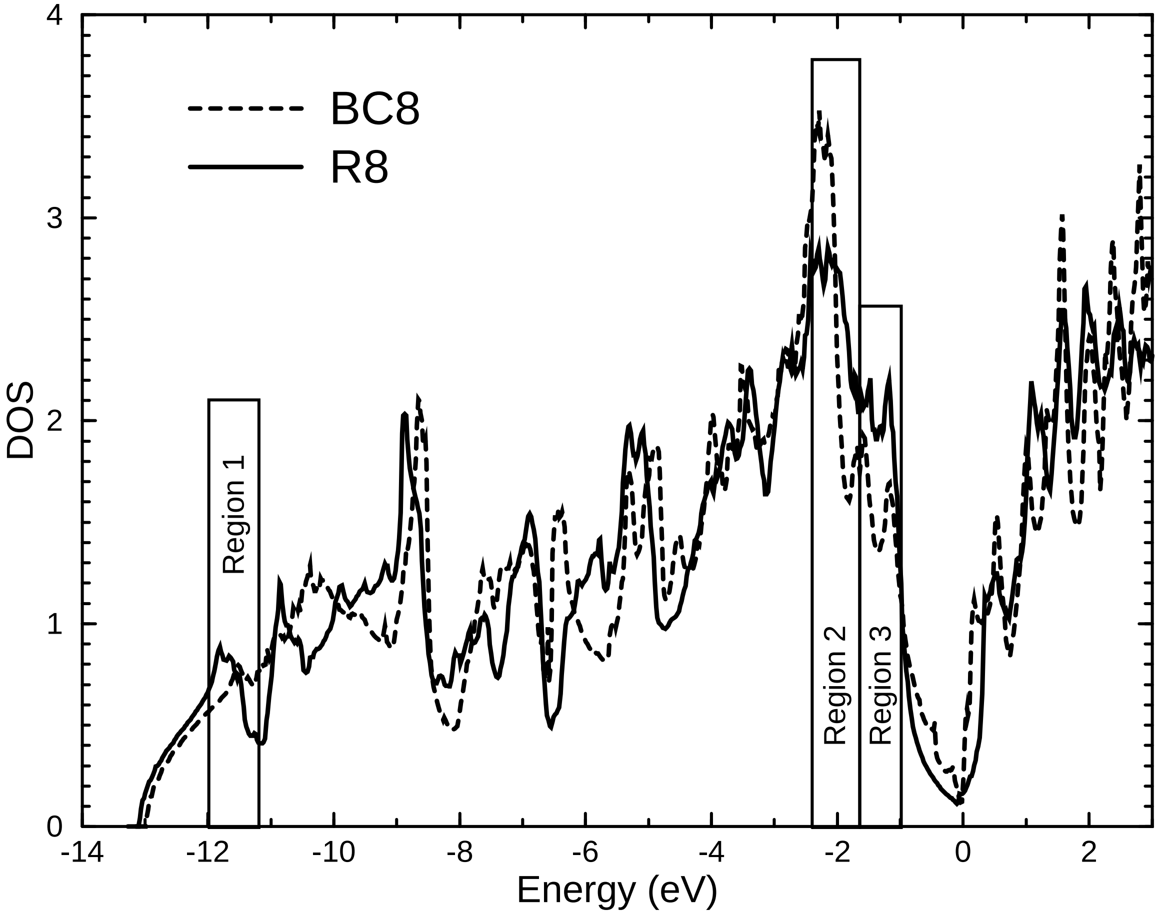

Figure 3.8: Density of states per unit cell, per spin, and per eV for silicon in the R8 (solid line) and BC8 (dashed line) phase. For both, the relaxed geometry from our calculation at zero pressure is assumed. The energy is given with respect to the Fermi level. Note the sharper valence band edge (Region 3) of R8, and the less pronounced peak in Region 2.

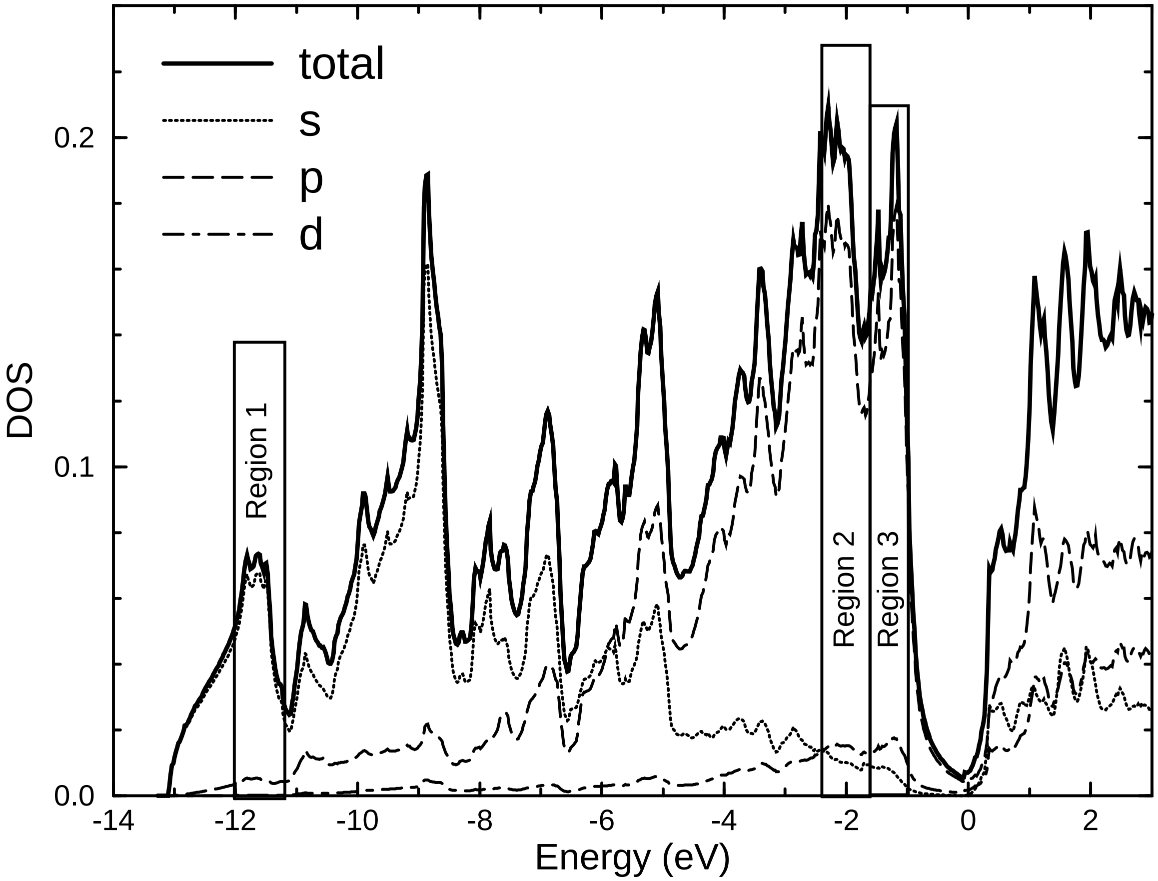

Figure 3.9: Local density of states per unit cell, per spin, and per eV for the 2(c) atoms of R8 silicon. The radius of the integration spheres is chosen such that for the shortest bond they just touch. Also shown is the local projection onto angular momentum eigenfunctions with *s* (dotted line), *p* (dashed line) and *d* (dot-dashed line) character. The characteristic features of R8 in the Regions 1 and 3 are strongly pronounced.

using the experimental structural parameters for R8 at 8.2 GPa, but aside from minor changes due to the different pressure, the features are the same. In summary, the characteristic differences in the DOS of BC8 and R8 are visible in the local DOS of both the 2(c) and 6(f) sites, but are more pronounced for the 2(c) atoms.

It is not clear whether the sharpening of the valence band edge (Region 3) can be directly associated with five-membered rings. However, the local DOS of the 2(c) atoms shows this feature stronger than the 6(f) atoms, while at the same time there are twice as many five-membered rings running through the 2(c) sites than through the 6(f) sites (Table 3.1). Perhaps it is more intuitive to interpret the sharpening of the valence band edge as a result of the distortion from the ideal tetrahedral angle, leading to high-energy *p*-type states at the top of the valence band, and low-energy *s*-type levels at the valence band bottom.

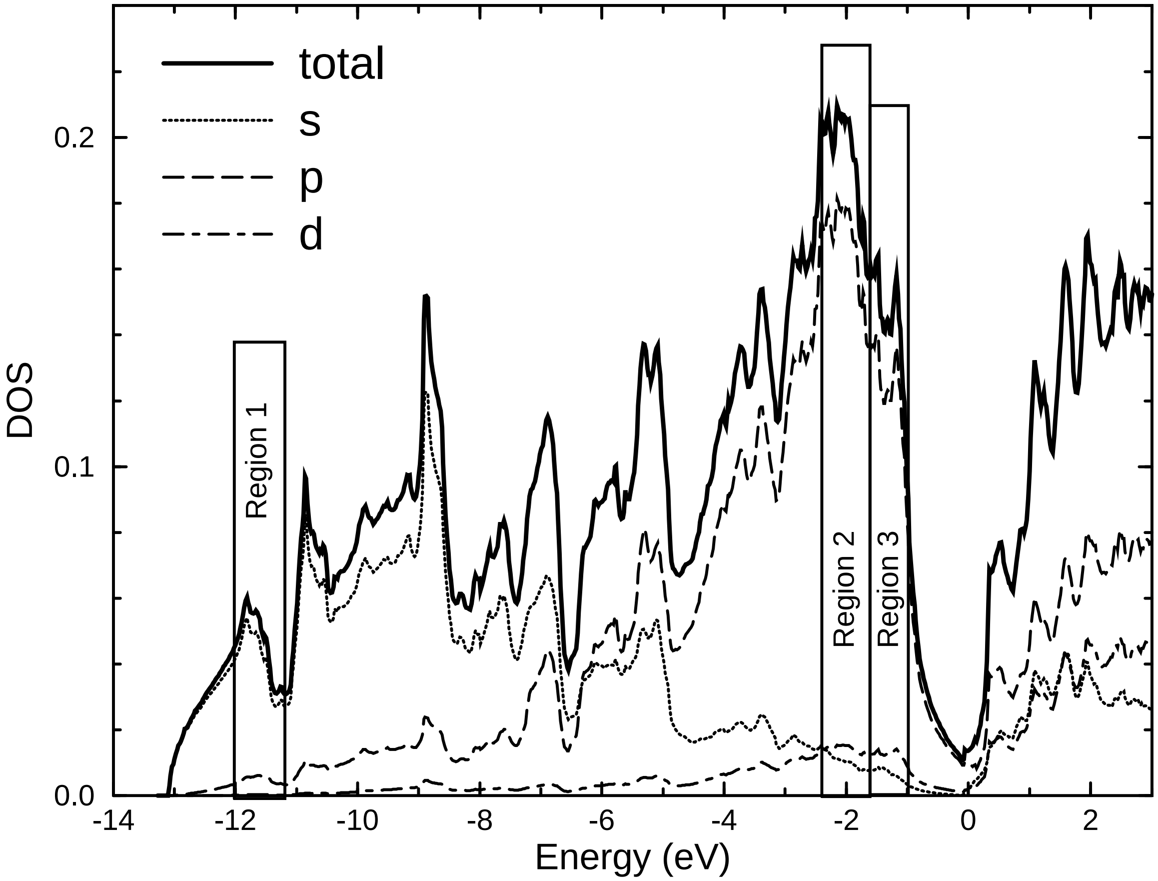

Figure 3.10: Same as in Fig. 3.9, but for the 6(f) atoms of R8. The *s*-type peak in Region 1 and the *p*-type peak in Region 3 are similar to the ones seen for the 2(c) atoms, but less pronounced.

3.7 Conclusion

In our *ab initio* DFT/LDA calculation, we find the energetics and unit cell volume of the R8 phase of silicon to be very similar to the one of the BC8 phase. This is reflected in their similar bulk moduli of 89 GPa (R8) and 92 GPa (BC8), and makes it difficult to compute the transition pressure between these two phases. At higher pressures, R8 becomes more stable than BC8, in agreement with experiment [46]. Both BC8 and R8 are found to be metastable with respect to the diamond or β-Sn structure. They are separated by a finite energy barrier over a large pressure range, and thus the BC8→R8 phase transition is of first order.

With increasing pressure, the rhombohedral angle α of the R8 phase opens, thereby reducing the second-nearest neighbor distance to accommodate the volume reduction. Our calculated lattice parameters and the internal degrees of freedom x, y, and z of the R8 phase agree well with the available experimental data, but our u parameter comes out to be 4% smaller.

The LDA band structure shows R8 silicon to be a semimetal with a 0.3 eV indirect band overlap between the T and L point. This is different from BC8, where a direct band overlap of 0.8 eV is found at the T-point. Due to the inaccuracies of LDA band structures, R8 silicon could also be a semiconductor with a small, indirect gap.

Similar to amorphous silicon, the DOS of R8 shows a sharpening of the valence band edge in R8 silicon. The states right at the edge are dominantly p-type, and have more weight on the 2(c) sites. A strong peak in the BC8 DOS, which has been attributed before to wurtzite-type eclipsed configurations [69], is less pronounced in R8. This coincides with the disappearance of eclipsed configurations when BC8 is transformed to R8.

Chapter 4

Structure and geochemistry of xenon at high pressures

4.1 Introduction

Xenon as a noble gas is characterized by its reluctance to form chemical bonds. However, Xe can form compounds [79, 80], and even becomes a hexagonal close-packed (hcp) metal at high pressures [81, 82, 83]. At the same time, a relative depletion of Earth's atmospheric Xe compared with meteoritic and solar abundances is observed [84, 85, 86] (the "missing Xe problem"), suggesting that significant amounts of Earth's primordial Xe could have formed a compound with the iron in the core [87].

Motivated by this idea, Sander Caldwell, Jeff Nguyen, and Raymond Jeanloz from the Department of Geology and Geophysics at Berkeley performed diamond-anvil cell high-pressure experiments on a sample containing a mixture of Xe and Fe. Under pressures of up to 70 GPa, a laser was used to heat the sample to peak temperatures of 3000K, in an effort to simulate the core's pressure of about 140-360 GPa and temperature of about 3500-6000K [88]. No evidence of a Xe-Fe compound was found, but new features of the high-pressure phase diagram of Xe were discovered. Earlier experimental work by Jephcoat *et al.* [89] had shown that Xe is stable in the face-centered cubic (fcc) phase up to 14 GPa and in the hcp phase above 75 GPa up to at least 137 GPa, but the diffraction pattern and crystal structure were not well resolved at intermediate pressures, and speculatively the experimental data was attributed to an intermediate phase [89]. Using laser heating, Caldwell, Nguyen, and Jeanloz could bracket the fcc↔hcp transition to about 18 to 24 GPa, and the intermediate phase was found to be a mixture of hcp and fcc Xe. They also found the fcc↔hcp to be extremely sluggish.

In this chapter, an *ab initio* study of Xe under pressure is presented. Two points are addressed. First, the energetics of the fcc↔hcp transition is studied in order to understand its sluggishness. Second, the possibility of Xe-Fe compounds is investigated by means of total energy calculations for a set of model compounds.

All calculations presented here are static-lattice calculations, corresponding to zero temperature and no zero-point vibrations. For the fcc↔hcp transition of Xe, neglecting entropy effects might not be a big error since the phonon spectra of the hcp and fcc phases are very similar. For the Xe-Fe compounds, the calculated enthalpies of formation are large enough to allow at least a qualitative assessment of the thermodynamic stability that is unlikely to change due to entropy effects. Our calculations are performed within the framework of density functional theory in the local density approximation (LDA) [16]. The electrons in the Xe and Fe cores are assumed to be inert, and are modeled by norm-conserving pseudopotentials [55] in the Kleinman-Bylander form [71]. A fairly large energy cutoff of 80 Ry is used for the representation of the valence electron wave functions with plane-waves. Such a large cutoff is necessary to accurately describe the localized Fe $3d$ electrons. At a given pressure, the internal coordinates of the structures and the lattice parameters are relaxed with the quasi-Newton method [72] described in chapter 2.

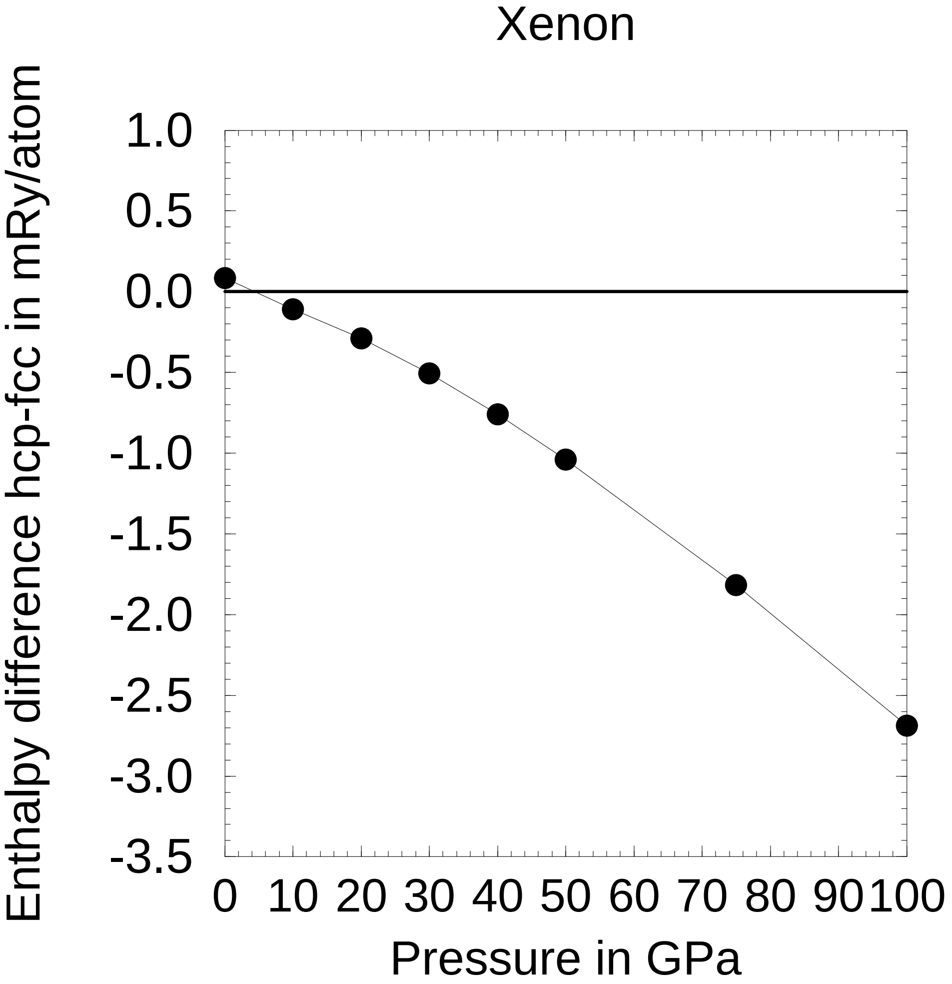

Figure 4.1: *Ab initio* enthalpy differences (in mRy) per atom between the hcp and fcc phases of xenon as a function of pressure. The hcp-fcc phase transition occurs at about 5 GPa.

4.2 Xenon under high pressure

The fcc and hcp phases are energetically very similar. Therefore, a fine k-point mesh of 60 and 70 special points is used for the fcc and hcp phases, respectively. With this choice of parameters, the inaccuracy in the enthalpy due to k-point sampling is less than 0.2 mRyd/atom. Fig. 4.1 shows the difference in enthalpy between the hcp and the fcc phase of Xe as a function of pressure. In agreement with experiment, the fcc phase is stable at lower pressures, whereas the hcp phase is favored at high pressure. The calculated transition pressure of about 5 GPa has to be taken with a grain of salt, since the enthalpy differences are very small, and the calculation might suffer from the shortcomings of the LDA. Thus, the general agreement with the experimental transition pressure of about 18-24 GPa found by Caldwell and coworkers [2] might be fortuitous. However, the small enthalpy differences observed in our calculation offer a good explanation for the observed sluggishness of the fcc-hcp transition.

As far as the structural properties are concerned, the agreement with experiment is quite good.

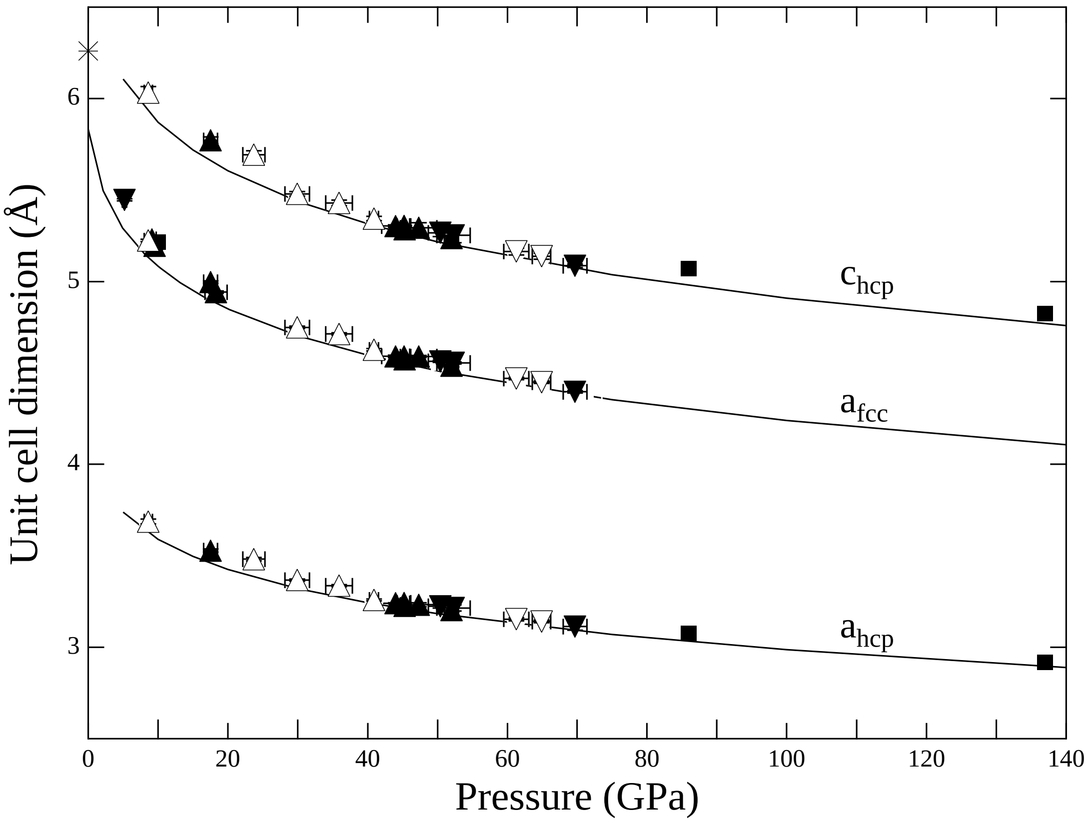

Figure 4.2: Unit cell parameters for the fcc (a) and hcp (a,c) phases of Xe plotted against pressure. Lines are from theory, whereas symbols indicate experimental results from Jephcoat *et al.* [89] (solid squares) and Caldwell *et al.* [2] (all other symbols).

Fig. 4.2 shows the calculated unit cell parameters (solid line) along with X-ray diffraction results (symbols). The c/a ratio of hcp Xe is also in close agreement with experiment as Fig. 4.3 shows. With increasing pressure, c/a deviates from the ideal $c/a = \sqrt{8/3} = 1.633$, indicating that the picture of close-packed hard spheres becomes less founded. As Fig. 4.3 demonstrates, the measured c/a ratio is close to the theoretical one, but it is difficult to measure the c/a ratio with high enough accuracy to discern an increase of c/a with rising pressure.

Although the bonding in Xe, like the other noble gases, has often been modeled through the use of pair potentials, the relatively low fcc-hcp transition pressure illustrates a deviation from such a simple model for the interatomic forces at high pressures. The transition pressure is predicted to be about 64 GPA in such models, even when three-body interaction terms are included [90]. Our *ab initio* calculation as well as the experimental findings of Caldwell *et al.* suggest that the three-body terms need to be corrected to yield a lower transition pressure.

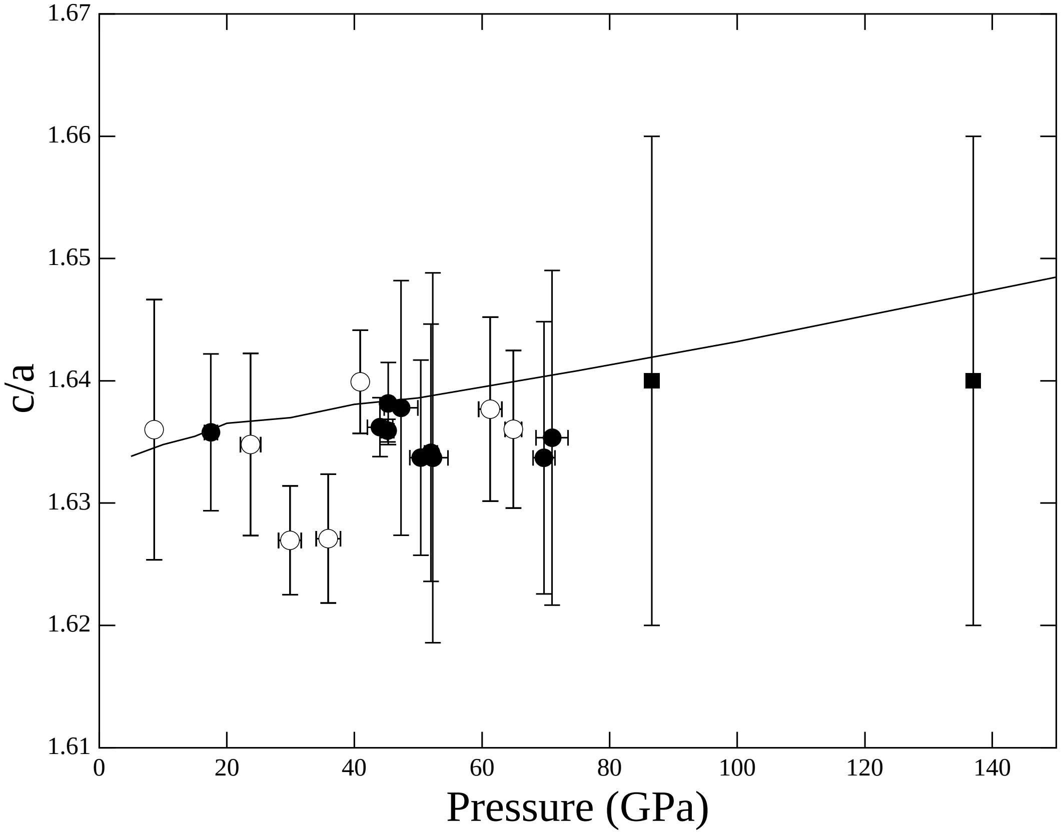

Figure 4.3: Comparison of the experimentally and theoretically determined c/a parameter of hcp Xe, plotted as a function of pressure. The solid line is from theory, whereas symbols indicate experimental results from Jephcoat *et al.* [89] (solid squares) and Caldwell *et al.* [2] (all other symbols).

Pressure (GPa)	XeFe $P\bar{3}m1$	Xe_2Fe $P\bar{6}m2$	$XeFe_2$ $P\bar{6}m2$	$XeFe_2$ hex. Laves
0	5.2	5.7	4.9	-
50	3.7	4.3	4.4	-
100	3.0	3.6	4.2	-
150	2.6	3.2	3.9	3.1
500	1.0	1.4	2.8	0.9

Table 4.1: Formation enthalpies of XeFe compounds in eV per formula unit. Quoted is the enthalpy of the compound minus the enthalpy of the separate elements.

4.3 Stability of xenon-iron compounds

In this section, four model compounds are used to explore the possibility of Xe and Fe forming a chemical bond:

- hcp XeFe, i.e. ABAB... stacking with alternating layers of Xe and Fe (space group $P\bar{6}m2$),
- hcp Xe_2Fe, with ABCABC... stacking, where A and B are Xe layers, and C is an iron layer (space group $P\bar{3}m1$),
- hcp $XeFe_2$, as before but with Fe A and B layers, and a Xe C layer (space group $P\bar{3}m1$),
- $XeFe_2$ in the hexagonal Laves phase (space group $P6_3/mmc$). The Laves phases are close-packed structures of differently-sized hard spheres. From the theoretically derived unit cell volume of hcp Fe and Xe, we calculated a ratio of 1.288 for the atomic radii of Xe/Fe at 150 GPa. For comparison, 138 out of 164 experimentally observed Laves phases have a ratio of atomic radii between 1.1 and 1.4 [91], showing that Xe and Fe are plausible candidates for forming a Laves phase at pressures above 100 GPa.

For pressures up to 500 GPa, we computed the enthalpy of the separated phases, Xe and Fe, and of the model compounds. Table 4.1 presents the enthalpy differences between the compounds and the separated phases. At any pressure, the compounds are energetically highly unfavorable. Even the least unstable model, the Laves phase, has a respectable 0.9 eV positive enthalpy of formation at 500 GPa.

Fig. 4.4 shows the electron density isosurface of $XeFe_2$ in the hexagonal Laves phase, corresponding to a value of 0.76 electrons/$Å^3$. While bonds between the Fe atoms (smaller spheres) are visible, no bond is formed between the Xe atoms (big spheres) and Fe. In fact, the charge density distribution around the Xe atoms is close to spherical. Thus, any incipient Xe-Fe bonding is so weak that it does not compensate for the energetic cost of breaking the strong Fe-Fe bond in iron, even at 150 to 500 GPa. The energetics are so unfavorable, that this conclusion is likely to be true for other structures and Fe/Xe stoichiometries than those we have considered.

In conclusion, our *ab initio* calculations indicate that Xe and Fe are unlikely to form a compound, even at high pressures. This does not necessarily mean the Xe could not be trapped in Earth's core. In fact, from our calculations, we find that for pressures larger than about 80 GPa, hcp Xe has a higher mass density than hcp Fe (see Fig. 4.5), and could therefore reside in the core. However,

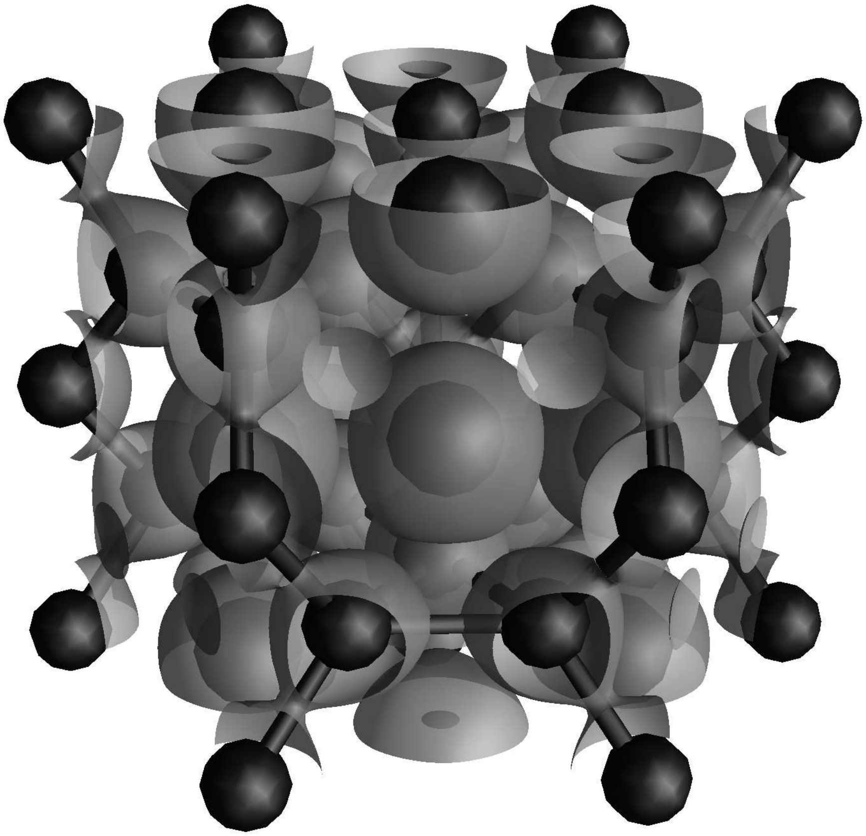

Figure 4.4: Electron density isosurface of $XeFe_2$ in the hexagonal Laves phase at 150 GPa, corresponding to a charge density of 0.76 electrons/Å^3. The larger spheres are Xe, the smaller ones are Fe. While bonds are visible between iron atoms, there is no bond between Xe and Fe.

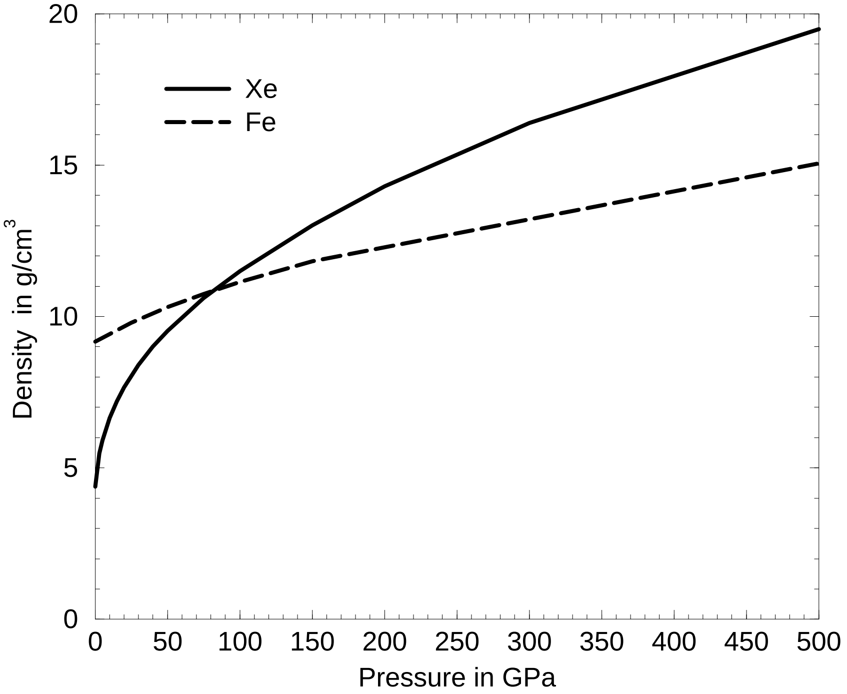

Figure 4.5: Computed density (in g/cm^3) of hcp Xe and Fe as a function of pressure. Above about 80 GPa, Xe has a higher density than Fe.

more research is necessary to determine if this observation can lead to a credible explanation of the missing xenon.

Chapter 5

Ab initio calculation of the NMR chemical shift

5.1 Introduction

Nuclear magnetic resonance (NMR) is one of the most widely used experimental techniques in structural chemistry. In particular, the measured chemical shift (σ) spectra are a fingerprint of the molecular geometry and the chemical structure of the material under study. Although the interpretation of these spectra generally relies on empirical rules, *ab initio* calculations of σ for molecules have led in many cases to an unambiguous determination of the microscopic structure [92]. Moreover, it is nowadays possible to measure σ also in solids with the resolution required for structural determinations [93, 94]. E.g., σ-spectra have been used for the characterization of amorphous carbon [95].

In NMR experiments, a uniform magnetic field $\mathbf{B}_{\text{ext}}$ is applied to a sample. The external field induces a magnetic field $\mathbf{B}_{\text{ind}}(\mathbf{r})$, such that the total local magnetic field is $\mathbf{B}(\mathbf{r}) = \mathbf{B}_{\text{ext}} + \mathbf{B}_{\text{ind}}(\mathbf{r})$. If there is a nucleus in the sample at position $\mathbf{r}_N$ with a spin of e.g. 1/2, and an associated magnetic moment μ_N, the nuclear spin up and down states are separated by an energy $2|\mathbf{B}(\mathbf{r}_N)|\mu$. The nuclear state for which the magnetic moment is parallel to $\mathbf{B}$ has lower energy, and is more populated than the other state. An incoming electromagnetic wave at the resonance frequency $\omega = 2|\mathbf{B}(\mathbf{r}_N)|\mu/\hbar$, typically in the MHz regime, will introduce transitions between the nuclear spin levels, and will be absorbed. Thus, by measuring the frequency of maximum absorption, one can determine the magnetic field at the position of the nucleus. The induced field $\mathbf{B}_{\text{ind}}(\mathbf{r}_N)$ depends on the electronic structure in the vicinity of the probed nucleus, and therefore a characteristic shift (called the chemical shift) of the resonance frequency will be observed when the same nucleus is probed in different chemical environments. Many other interesting quantities can be measured with NMR, for instance the spin relaxation times T_1 and T_2 and, by quadrupole resonance, electric field gradients at the nucleus [96, 97]. In this chapter, only a single aspect will be considered, which is the NMR chemical shift of insulators.

Several distinct effects contribute to the induced magnetic field: the alignment of electronic and nuclear magnetic moments along $\mathbf{B}_{\text{ext}}$, and the induced orbital motion of the electrons. For insulators, the electronic spin does not contribute to the chemical shift, as the rather small $\mathbf{B}_{\text{ext}}$ does not lead to a net electronic spin. The induced magnetic field due to nuclear spin alignment is either very small, or deliberately suppressed by special experimental techniques such as magic angle spinning (MAS) or multi-pulse sequences [98]. Under these circumstances, $\mathbf{B}_{\text{ind}}$ arises solely from induced electron motion. In this chapter, a new *ab initio* method [99, 100, 101] is presented to calculate the induced field due to electronic orbital motion. Such calculations were possible for finite systems before, and in fact have been carried out for atoms and molecules since the mid seventies[102]. However, with the new method presented below, infinite periodic systems can now be treated for the first time. This has clear advantages for crystals, amorphous solids, and liquids, where large cluster simulations are expensive, and complicated by artificial surface effects.

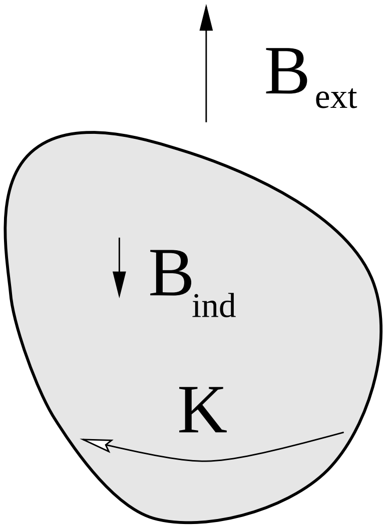

Figure 5.1: An applied external magnetic field $\mathbf{B}_{\text{ext}}$ causes a macroscopic surface current density $\mathbf{K}$, which leads to a contribution to the induced field $\mathbf{B}_{\text{ind}}$ deep inside the sample.

5.2 NMR chemical shift tensor and magnetic susceptibility

The goal of NMR chemical shift calculations is to compute the induced magnetic field $\mathbf{B}_{\text{ind}}(\mathbf{r})$. For the relatively small magnetic fields used in experiments, say, a few Teslas, there is a linear relationship between the external field $\mathbf{B}_{\text{ext}}$ and the induced field:

$$\mathbf{B}_{\text{ind}}(\mathbf{r}) = -\overleftrightarrow{\sigma}(\mathbf{r})\mathbf{B}_{\text{ext}} \; . \tag{5.1}$$

Here, $\overleftrightarrow{\sigma}$ is the chemical shift tensor or shielding tensor, which will be computed below. NMR experiments measure only the symmetric part $\frac{1}{2}(\overleftrightarrow{\sigma} + \overleftrightarrow{\sigma}^T)$, or often just the isotropic shift $\sigma = \frac{1}{3}\text{Tr}(\overleftrightarrow{\sigma})$. One peculiar aspect of $\overleftrightarrow{\sigma}$ is its dependence on the shape of the sample. As is well known from classical magnetostatics [103], $\mathbf{B}_{\text{ext}}$ gives rise to a macroscopic current density $\mathbf{K}$ on the surface of the sample, which in turn yields a sample-shape-dependent contribution to $\mathbf{B}_{\text{ind}}$, even deep inside the sample. This is depicted in Fig. 5.1. As a consequence, when $\overleftrightarrow{\sigma}$ is calculated in Fourier space:

$$\overleftrightarrow{\sigma}(\mathbf{r}) = \sum_{\mathbf{G}} \overleftrightarrow{\tilde{\sigma}}(\mathbf{G}) e^{i\mathbf{G}\cdot\mathbf{r}} \; , \tag{5.2}$$

for a periodic system with reciprocal lattice vectors $\mathbf{G}$, then $\overleftrightarrow{\tilde{\sigma}}(\mathbf{G})$ is a bulk property for $\mathbf{G} \neq \mathbf{0}$, i.e. it is independent of the sample shape. On the other hand, $\overleftrightarrow{\tilde{\sigma}}(\mathbf{0})$ depends on the sample shape for the reasons mentioned above. In NMR experiments, only a few sample shapes are typically used: a cylindrical sample parallel or perpendicular to the external field, or a spherical sample. By convention, the chemical shift tensor is quoted for a spherical sample shape, but given the magnetic susceptibility, one can easily convert from one sample shape to the other. Assuming an isotropic magnetic susceptibility χ, one finds the diagonal components of $\overleftrightarrow{\tilde{\sigma}}(\mathbf{0})$ to be $-\frac{8\pi}{3}\chi$ for a sphere, or $-2\pi\chi$ and $-4\pi\chi$ for a cylinder perpendicular and parallel to $\mathbf{B}_{\text{ext}}$, respectively.

5.3 Chemical shift tensor as an energy derivative

Given a microscopic current density $\mathbf{J}(\mathbf{r})$ due to $\mathbf{B}_{\text{ext}}$, the induced magnetic field is

$$\mathbf{B}_{\text{ind}}(\mathbf{r}) = \frac{1}{c}\int \mathbf{J}(\mathbf{r}') \times \frac{\mathbf{r}-\mathbf{r}'}{|\mathbf{r}-\mathbf{r}'|^3} \mathrm{d}^3 r' \ . \tag{5.3}$$

Fourier transforming the entities in (5.3), and excluding the $\mathbf{G} = \mathbf{0}$ case for the moment, one arrives at

$$\mathbf{B}_{\text{ind}}(\mathbf{G}) = \left(\frac{4\pi i}{c}\right) \frac{\mathbf{G}}{|\mathbf{G}|^2} \times \mathbf{J}(\mathbf{G}) \ . \tag{5.4}$$

Furthermore, $\mathbf{J}$ can be related to the first derivative of the energy with respect to the magnetic field. To see this, a vector potential $\mathbf{A}$ is introduced in the special form:

$$\mathbf{A}_{\mathbf{s}} = c B_{\mathbf{s}} \mathbf{a}_{\mathbf{s}} e^{i\mathbf{s}\cdot\mathbf{r}} \ , \tag{5.5}$$

where

$$\mathbf{a}_{\mathbf{s}} = \left(\frac{i}{c}\right) \frac{\mathbf{s} \times \hat{\mathbf{b}}_{\mathbf{s}}}{|\mathbf{s}|^2} \ . \tag{5.6}$$

Taking the curl of $\mathbf{A}_{\mathbf{s}}$, one obtains a magnetic field with scalar amplitude $B_{\mathbf{s}}$ in the direction of the unit length vector $\hat{\mathbf{b}}_{\mathbf{s}}$, modulated with a wave vector $\mathbf{s}$:

$$\mathbf{B}_{\mathbf{s}} = B_{\mathbf{s}} \hat{\mathbf{b}}_{\mathbf{s}} e^{i\mathbf{s}\cdot\mathbf{r}} \ . \tag{5.7}$$

The energy density depends on the vector potential through the full many-body Hamiltonian $\mathcal{H}$, which is, using atomic units ($\hbar = m = e = 1$):

$$\begin{aligned} \mathcal{H} &= \sum_{\alpha} \int \mathrm{d}^3 r \ \psi_{\alpha}^{\dagger}(\mathbf{r}) \left[\frac{1}{2}(-i\nabla + \frac{1}{c}\mathbf{A})^2 + V_{\text{ext}}(\mathbf{r})\right] \psi_{\alpha}(\mathbf{r}) \\ &\quad + \frac{1}{2}\sum_{\alpha\beta} \int \mathrm{d}^3 r \int \mathrm{d}^3 r' \frac{\psi_{\alpha}^{\dagger}(\mathbf{r})\psi_{\beta}^{\dagger}(\mathbf{r}')\psi_{\beta}(\mathbf{r}')\psi_{\alpha}(\mathbf{r})}{|\mathbf{r}-\mathbf{r}'|} \ . \end{aligned}$$

Here, V_{ext} is the external potential generated by the atomic nuclei, and ψ is the field operator. The indices α and β denote spin quantum numbers. To arrive at the energy density, the Hamiltonian is bracketed between the many-body ground state $|g\rangle$:

$$E = \frac{1}{\Omega}\langle g|\mathcal{H}|g\rangle \ . \tag{5.8}$$

Ω denotes the total volume of the system. Notice that $|g\rangle$ itself also depends on the vector potential, as the ground state depends on the Hamiltonian.

The many-body expression for the electric current density of an electron system is

$$\mathbf{J}(\mathbf{r}) = -\frac{1}{2}\langle g| \sum_{\alpha} \psi_{\alpha}^{\dagger}(\mathbf{r})(-i\nabla + \frac{1}{c}\mathbf{A}(\mathbf{r}))\psi_{\alpha}(\mathbf{r}) + \left[(-i\nabla + \frac{1}{c}\mathbf{A}(\mathbf{r}))\psi_{\alpha}(\mathbf{r})\right]^{\dagger} \psi_{\alpha}(\mathbf{r})|g\rangle \ . \tag{5.9}$$

That the current is a derivative of the energy density with respect to the magnetic field can be seen by starting from Eq. (5.8), substituting the vector potential from Eq. (5.5), and choosing the periodicity of the magnetic field to be $\mathbf{s} = -\mathbf{G}$. One immediately finds that

$$\frac{\partial E}{\partial B_{-\mathbf{G}}} = -\left(\frac{i}{c}\right) \frac{\hat{\mathbf{b}}_{-\mathbf{G}} \cdot (\mathbf{G} \times \mathbf{J}(\mathbf{G}))}{|\mathbf{G}|^2}, \tag{5.10}$$

and hence with Eq. (5.4)

$$\frac{\partial E}{\partial B_{-\mathbf{G}}} = -\frac{1}{4\pi} \hat{\mathbf{b}}_{-\mathbf{G}} \cdot \mathbf{B}_{\text{ind}}(\mathbf{G}) \ . \tag{5.11}$$

Finally, the chemical shift tensor can be calculated by taking the derivative of the Fourier-transformed Eq. (5.1),

$$\mathbf{B}_{\text{ind}}(\mathbf{G}) = -\overset{\leftrightarrow}{\tilde{\sigma}}(\mathbf{G}) \mathbf{B}_{\text{ext}} \ , \tag{5.12}$$

with respect to a constant external field, $\mathbf{B}_{\text{ext}} = B_{\mathbf{0}} \hat{\mathbf{b}}_{\mathbf{0}}$. Thus combining (5.12) and (5.11), one finds

$$\left. \frac{\partial^2 E}{\partial B_{-\mathbf{G}} \partial B_{\mathbf{0}}} \right|_{\mathbf{B}=\mathbf{0}} = \frac{1}{4\pi} \hat{\mathbf{b}}_{-\mathbf{G}} \cdot \overset{\leftrightarrow}{\tilde{\sigma}}(\mathbf{G}) \cdot \hat{\mathbf{b}}_{\mathbf{0}}. \tag{5.13}$$

Evidently, $\overset{\leftrightarrow}{\tilde{\sigma}}$ is directly proportional to the $\mathbf{G}' = \mathbf{0}$ column of the susceptibility matrix $\overset{\leftrightarrow}{\chi}(\mathbf{G}, \mathbf{G}')$, which is defined as

$$-\left. \frac{\partial^2 E}{\partial B_{-\mathbf{G}} \partial B_{-\mathbf{G}'}} \right|_{\mathbf{B}=\mathbf{0}} = \hat{\mathbf{b}}_{-\mathbf{G}} \cdot \overset{\leftrightarrow}{\chi}(\mathbf{G}, \mathbf{G}') \cdot \hat{\mathbf{b}}_{-\mathbf{G}'} \ . \tag{5.14}$$

As mentioned in the beginning of this section, $\overset{\leftrightarrow}{\tilde{\sigma}}(\mathbf{0})$ must be treated separately, taking into account the sample shape. The following section will outline the calculation of the second energy derivative in Eq. (5.14).

5.4 Perturbation theory

It has been shown in Section 5.3 that $\overset{\leftrightarrow}{\sigma}$ is closely related to the magnetic susceptibility via Eqs. (5.13) and (5.14). In this section, a calculation of $\overset{\leftrightarrow}{\chi}(\mathbf{G}, \mathbf{0})$ by means of perturbation theory is presented.

To calculate the second derivatives in (5.13), some assumptions must be made about the dependence of the energy on the vector potential. We work within the Kohn-Sham density functional formalism, and assume that the energy density depends on the vector potential and the single-particle ground-state orbital wave functions $|\psi_i\rangle$ via

$$\begin{aligned} E \ = \ & \frac{1}{\Omega} \left\{ 2 \sum_{i \in \mathcal{O}} \langle \psi_i | \frac{1}{2} (\mathbf{p} + \frac{1}{c} \mathbf{A})^2 | \psi_i \rangle + \int \mathrm{d}^3 r \rho(\mathbf{r}) V_{\text{ext}}(\mathbf{r}) \right. \\ & \left. + \frac{1}{2} \int \mathrm{d}^3 r \int \mathrm{d}^3 r' \frac{\rho(\mathbf{r}) \rho(\mathbf{r}')}{|\mathbf{r} - \mathbf{r}'|} + E_{xc}[\rho] \right\} \ . \end{aligned} \tag{5.15}$$

Because of spin degeneracy, the sum over the occupied ($\mathcal{O}$) orbital wave functions runs only over half the number of electrons in the system. The momentum operator is denoted with $\mathbf{p} = -i\nabla$. Notice that the exchange-correlation energy E_{xc} depends only on the electron density, which is computed from the wave functions in the usual way, $\rho(\mathbf{r}) = 2\sum_{i\in\mathcal{O}} |\langle\psi_i|\mathbf{r}\rangle|^2$.

Introducing the vector potential into the energy functional as in (5.15) is an approximation. To be exact, one should use current density functional theory, where the exchange-correlation energy depends not just on ρ, but on the current as well. Indeed, approximate current density functionals have been proposed, which take this into account [104]. For the systems considered in this thesis, the effects are small though [105], and thus Eq. (5.15) is a good approximation for the evaluation of the energy derivatives with respect to $\mathbf{B}$ up to second order.

Particular care must be taken when perturbation theory is applied to infinite systems in a magnetic field. For instance, the expectation value of the square of the vector potential for a constant magnetic field in the symmetric gauge, $\langle\psi|(\frac{1}{2}\mathbf{B}_{\text{ext}} \times \mathbf{r})^2|\psi\rangle$, diverges if the wave function $|\psi\rangle$ becomes an infinitely extended Bloch function. To make the divergences manageable, the external magnetic field is modulated with a finite wave vector $\mathbf{q}$. Later, the limit of $\mathbf{q} \to 0$ is performed to recover the limit of a uniform field. Since in (5.13) there are derivatives with respect to magnetic fields of wave vector $\mathbf{0}$ (the external field), and $-\mathbf{G}$ (the "probe" field), a vector potential of the form:

$$\mathbf{A}(\mathbf{r}) = cB_{\mathbf{q}}\mathbf{a}_{\mathbf{q}}e^{i\mathbf{q}\cdot\mathbf{r}} + cB_{-\mathbf{G}-\mathbf{q}}\mathbf{a}_{-\mathbf{G}-\mathbf{q}}e^{-i(\mathbf{G}+\mathbf{q})\cdot\mathbf{r}} \tag{5.16}$$

is chosen. Here, $\mathbf{a}_{\mathbf{q}}$ and $\mathbf{a}_{-\mathbf{G}-\mathbf{q}}$ are defined as in (5.6). Taking the curl of $\mathbf{A}$ in (5.16) shows that the corresponding magnetic field is

$$\mathbf{B}(\mathbf{r}) = B_{\mathbf{q}}\hat{\mathbf{b}}_{\mathbf{q}}e^{i\mathbf{q}\cdot\mathbf{r}} + B_{-\mathbf{G}-\mathbf{q}}\hat{\mathbf{b}}_{-\mathbf{G}-\mathbf{q}}e^{-i(\mathbf{q}+\mathbf{G})\cdot\mathbf{r}} \ , \tag{5.17}$$

which in the limit $q \to 0$ turns into the sum of a constant field and a field with wave vector $-\mathbf{G}$. One has to modulate the second field with $-(\mathbf{G}+\mathbf{q})$ rather than just $-\mathbf{G}$ in order to get appropriate behavior for finite $\mathbf{q}$. With this particular form (5.16) of the vector potential, the energy derivative in Eq. (5.14) is now computed from the energy functional (5.15):

$$\begin{aligned} \left.\frac{\partial^2 E}{\partial B_{\mathbf{q}}\partial B_{-\mathbf{G}-\mathbf{q}}}\right|_{\mathbf{B}=\mathbf{0}} &= \frac{2}{\Omega}\sum_{i\in\mathcal{O}}\Bigg[\langle\psi_i|\frac{\partial^2 H}{\partial B_{\mathbf{q}}\partial B_{-\mathbf{G}-\mathbf{q}}}|\psi_i\rangle \\ &\quad + \langle\psi_i|\frac{\partial H}{\partial B_{-\mathbf{G}-\mathbf{q}}}\frac{\partial|\psi_i\rangle}{\partial B_{\mathbf{q}}} + \frac{\partial\langle\psi_i|}{\partial B_{\mathbf{q}}}\frac{\partial H}{\partial B_{-\mathbf{G}-\mathbf{q}}}|\psi_i\rangle\Bigg]\Bigg|_{\mathbf{B}=\mathbf{0}} \ . \end{aligned} \tag{5.18}$$

Here, the single-particle Kohn-Sham Hamiltonian H has been introduced, which is defined as

$$\frac{\partial E}{\partial\langle\psi_i|} = H|\psi_i\rangle \ . \tag{5.19}$$

It follows from (5.16) and (5.15) that the derivatives of the Hamiltonian H are:

$$\begin{aligned} H'_{\mathbf{q}} := \left.\frac{\partial H}{\partial B_{\mathbf{q}}}\right|_{\mathbf{B}=\mathbf{0}} &= \frac{1}{2}\left[e^{i\mathbf{q}\cdot\mathbf{r}}\mathbf{a}_{\mathbf{q}}\cdot\mathbf{p} + \mathbf{a}_{\mathbf{q}}\cdot\mathbf{p}\ e^{i\mathbf{q}\cdot\mathbf{r}}\right] \\ H'_{-\mathbf{G}-\mathbf{q}} := \left.\frac{\partial H}{\partial B_{-\mathbf{G}-\mathbf{q}}}\right|_{\mathbf{B}=\mathbf{0}} &= \frac{1}{2}\left[e^{-i(\mathbf{G}+\mathbf{q})\cdot\mathbf{r}}\mathbf{a}_{-\mathbf{G}-\mathbf{q}}\cdot\mathbf{p} + \mathbf{a}_{-\mathbf{G}-\mathbf{q}}\cdot\mathbf{p}\ e^{-i(\mathbf{G}+\mathbf{q})\cdot\mathbf{r}}\right] \\ H''_{\mathbf{q},-\mathbf{G}-\mathbf{q}} := \left.\frac{\partial^2 H}{\partial B_{\mathbf{q}}\partial B_{-\mathbf{G}-\mathbf{q}}}\right|_{\mathbf{B}=\mathbf{0}} &= \left[\mathbf{a}_{\mathbf{q}}\cdot\mathbf{a}_{-\mathbf{G}-\mathbf{q}}e^{-i\mathbf{G}\cdot\mathbf{r}}\right] \ . \end{aligned} \tag{5.20}$$

Notice that when computing (5.20), we have neglected the dependence of the Hamiltonian on the electron density (which in turn depends on the magnetic field). This is not an approximation, because the electron density is a scalar under time inversion [103], but the magnetic field changes sign, and hence by time reversal symmetry, the electron density cannot depend on the magnetic field to first order.

Calculating the derivative of the wave functions by first order perturbation theory, and assuming the wave functions to be Bloch functions $|\psi^i_{\mathbf{k}}\rangle$ of energy $\epsilon^i_{\mathbf{k}}$, labeled with a band index i and crystal momentum $\mathbf{k}$, one finds:

$$\left.\frac{\partial^2 E}{\partial B_{\mathbf{q}} \partial B_{-\mathbf{G}-\mathbf{q}}}\right|_{\mathbf{B}=0} = \frac{2}{\Omega}\left[\Omega \int \frac{\mathrm{d}^3 k}{(2\pi)^3} \sum_{i\in\mathcal{O}} \langle \psi^i_{\mathbf{k}} | H''_{\mathbf{q},-\mathbf{G}-\mathbf{q}} | \psi^i_{\mathbf{k}}\rangle \right. \tag{5.21}$$

$$\left. + \Omega^2 \int \frac{\mathrm{d}^3 k}{(2\pi)^3} \int \frac{\mathrm{d}^3 k'}{(2\pi)^3} \sum_{\substack{i\in\mathcal{O}\\ j\neq i}} \left(\frac{\langle \psi^i_{\mathbf{k}} | H'_{\mathbf{q}} | \psi^j_{\mathbf{k}'}\rangle \langle \psi^j_{\mathbf{k}'} | H'_{-\mathbf{G}-\mathbf{q}} | \psi^i_{\mathbf{k}}\rangle}{\epsilon^i_{\mathbf{k}} - \epsilon^j_{\mathbf{k}'}} + \frac{\langle \psi^i_{\mathbf{k}} | H'_{-\mathbf{G}-\mathbf{q}} | \psi^j_{\mathbf{k}'}\rangle \langle \psi^j_{\mathbf{k}'} | H'_{\mathbf{q}} | \psi^i_{\mathbf{k}}\rangle}{\epsilon^i_{\mathbf{k}} - \epsilon^j_{\mathbf{k}'}} \right) \right] .$$

Notice that the sum with index j covers the full spectrum. Because of the computational cost of computing the full spectrum $\epsilon^j_{\mathbf{k}}$, Eq. (5.21) is mostly for didactic purposes. As will be shown later, the derivative of the wave function can be obtained without a sum over "excited" states. But first, the periodicity $|\psi^j_{\mathbf{k}}\rangle = e^{i\mathbf{k}\cdot\mathbf{r}}|u_{\mathbf{k},j}\rangle$ of the Bloch states and (5.20) are used to arrive at:

$$\left.\frac{\partial^2 E}{\partial B_{\mathbf{q}} \partial B_{-\mathbf{G}-\mathbf{q}}}\right|_{\mathbf{B}=\mathbf{0}} = 2\, \mathbf{a}_{\mathbf{q}} \cdot \mathbf{a}_{-\mathbf{G}-\mathbf{q}} \int \frac{\mathrm{d}^3 k}{(2\pi)^3} \sum_{i\in\mathcal{O}} \langle u_{\mathbf{k},i} | e^{-i\mathbf{G}\cdot\mathbf{r}} | u_{\mathbf{k},i}\rangle + f(\mathbf{a}_{\mathbf{q}}, \mathbf{a}_{-\mathbf{G}-\mathbf{q}}, \mathbf{G}, \mathbf{q}) \ , \tag{5.22}$$

where for convenience, a function f has been defined as:

$$f(\mathbf{a}_{\mathbf{q}}, \mathbf{a}_{-\mathbf{G}-\mathbf{q}}, \mathbf{G}, \mathbf{q}) := \tag{5.23}$$

$$2 \int \frac{\mathrm{d}^3 k}{(2\pi)^3} \sum_{\substack{i\in\mathcal{O}\\ j\neq i}} \left[\frac{\langle u_{\mathbf{k},i} | \mathbf{a}_{\mathbf{q}} \cdot (-i\nabla + \mathbf{k} - \mathbf{q}/2) | u_{\mathbf{k}-\mathbf{q},j}\rangle \langle u_{\mathbf{k}-\mathbf{q},j} | e^{-i\mathbf{G}\cdot\mathbf{r}} \mathbf{a}_{-\mathbf{G}-\mathbf{q}} \cdot (-i\nabla + \mathbf{k}) | u_{\mathbf{k},i}\rangle}{\epsilon^i_{\mathbf{k}} - \epsilon^j_{\mathbf{k}-\mathbf{q}}} \right.$$

$$\left. + \frac{\langle u_{\mathbf{k},i} | e^{-i\mathbf{G}\cdot\mathbf{r}} \mathbf{a}_{-\mathbf{G}-\mathbf{q}} \cdot (-i\nabla + \mathbf{k} + \mathbf{q}) | u_{\mathbf{k}+\mathbf{q},j}\rangle \langle u_{\mathbf{k}+\mathbf{q},j} | \mathbf{a}_{\mathbf{q}} \cdot (-i\nabla + \mathbf{k} + \mathbf{q}/2) | u_{\mathbf{k},i}\rangle}{\epsilon^i_{\mathbf{k}} - \epsilon^j_{\mathbf{k}+\mathbf{q}}} \right] .$$

Now, a few definitions are necessary to show how (5.23) can be calculated efficiently. First, the perturbed wave function $|u^{\mathbf{q},\mathbf{a}_{\mathbf{q}}}_{\mathbf{k},i}\rangle$ is defined as:

$$|u^{\mathbf{q},\mathbf{a}_{\mathbf{q}}}_{\mathbf{k},i}\rangle := \sum_{j\in\mathcal{E}} \frac{|u_{\mathbf{k}+\mathbf{q},j}\rangle \langle u_{\mathbf{k}+\mathbf{q},j} | \mathbf{a}_{\mathbf{q}} \cdot (-i\nabla + \mathbf{k} + \mathbf{q}/2) | u_{\mathbf{k},i}\rangle}{\epsilon^i_{\mathbf{k}} - \epsilon^j_{\mathbf{k}+\mathbf{q}}} \ . \tag{5.24}$$

Notice the sum over all unoccupied ("empty") states ($\mathcal{E}$), which is expensive to compute. However, $|u^{\mathbf{q},\mathbf{a}_{\mathbf{q}}}_{\mathbf{k},i}\rangle$ can be obtained much faster by solving the following system of linear equations:

$$(\epsilon^i_{\mathbf{k}} - H_{\mathbf{k}+\mathbf{q}}) |u^{\mathbf{q},\mathbf{a}_{\mathbf{q}}}_{\mathbf{k},i}\rangle = \left[1 - \sum_{m\in\mathcal{O}} |u_{\mathbf{k}+\mathbf{q},m}\rangle \langle u_{\mathbf{k}+\mathbf{q},m}| \right] \mathbf{a}_{\mathbf{q}} \cdot (-i\nabla + \mathbf{k} + \mathbf{q}/2) | u_{\mathbf{k},i}\rangle \ , \tag{5.25}$$

using e.g. a conjugate gradient algorithm. Armed with $|u^{\mathbf{q},\mathbf{a}_{\mathbf{q}}}_{\mathbf{k},i}\rangle$, straight forward algebra leads from (5.23) to

$$f(\mathbf{a}_{\mathbf{q}}, \mathbf{a}_{-\mathbf{G}-\mathbf{q}}, \mathbf{G}, \mathbf{q}) = \int \mathrm{d}^3 r\, e^{-i\mathbf{G}\cdot\mathbf{r}} \left[h(\mathbf{a}_{\mathbf{q}}, \mathbf{a}_{-\mathbf{G}-\mathbf{q}}, \mathbf{r}, \mathbf{q}) + h^*(\mathbf{a}^*_{\mathbf{q}}, \mathbf{a}^*_{-\mathbf{G}-\mathbf{q}}, \mathbf{r}, -\mathbf{q}) \right] \ , \tag{5.26}$$

where h is defined as:

$$\begin{aligned} h(\mathbf{a}_\mathbf{q}, \mathbf{a}_{-\mathbf{G}-\mathbf{q}}, \mathbf{r}, \mathbf{q}) &= \int \frac{\mathrm{d}^3k}{(2\pi)^3} \sum_{i\in\mathcal{O}} \Big[\langle u_{\mathbf{k},i}|\mathbf{r}\rangle\langle\mathbf{r}|\mathbf{a}_{-\mathbf{G}-\mathbf{q}} \cdot (-i\nabla + \mathbf{k} + \mathbf{q})|u_{\mathbf{k},i}^{\mathbf{q},\mathbf{a}_\mathbf{q}}\rangle \\ &\qquad + \langle u_{\mathbf{k},i}|\mathbf{a}_{-\mathbf{G}-\mathbf{q}} \cdot (-i\nabla + \mathbf{k})|\mathbf{r}\rangle\langle\mathbf{r}|u_{\mathbf{k},i}^{\mathbf{q},\mathbf{a}_\mathbf{q}}\rangle \Big] \ . \end{aligned} \tag{5.27}$$

It is evident from (5.26) that once $h(\mathbf{a}_\mathbf{q}, \mathbf{a}_{-\mathbf{G}-\mathbf{q}}, \mathbf{r}, \mathbf{q})$ and $h^*(\mathbf{a}^*_\mathbf{q}, \mathbf{a}^*_{-\mathbf{G}-\mathbf{q}}, \mathbf{r}, -\mathbf{q})$ are computed, $f(\mathbf{a}_\mathbf{q}, \mathbf{a}_{-\mathbf{G}-\mathbf{q}}, \mathbf{G}, \mathbf{q})$ is readily calculated with a Fast Fourier Transform.

5.5 Handling divergences with the sum rule

Although it is now clear that $f(\mathbf{a}_\mathbf{q}, \mathbf{a}_{-\mathbf{G}-\mathbf{q}}, \mathbf{G}, \mathbf{q})$ can be computed efficiently, one still has to deal with the divergences from which Eq. (5.22) suffers. In fact, for $\mathbf{G} \neq \mathbf{0}$, both the first and the second term diverge individually like $\sim \frac{1}{q}$ as $q \to 0$, but their sum is finite. It turns out that a sum rule can be used to recast the first term into a more convenient form. First, consider $f(\mathbf{a}_\mathbf{q}, \mathbf{a}_{-\mathbf{G}-\mathbf{q}}, \mathbf{G}, \mathbf{q} = \mathbf{0})$, i.e. $\mathbf{q} = \mathbf{0}$ only for the last argument of f. Then, by $(\mathbf{k}\cdot\mathbf{p})$-perturbation theory, the perturbed wave function is just the derivative with respect to $\mathbf{k}$:

$$\sum_{j\neq i} \frac{|u_{\mathbf{k},j}\rangle\langle u_{\mathbf{k},j}|\mathbf{a}_\mathbf{q} \cdot (-i\nabla + \mathbf{k})|u_{\mathbf{k},i}\rangle}{\epsilon^i_\mathbf{k} - \epsilon^j_\mathbf{k}} = \mathbf{a}_\mathbf{q} \cdot \frac{\mathrm{d}|u_{\mathbf{k},i}\rangle}{\mathrm{d}\mathbf{k}} \ . \tag{5.28}$$

Inserting (5.28) into the definition of f in Eq. (5.23) one finds:

$$\begin{aligned} f(\mathbf{a}_\mathbf{q}, \mathbf{a}_{-\mathbf{G}-\mathbf{q}}, \mathbf{G}, \mathbf{0}) &= \int \frac{\mathrm{d}^3k}{(2\pi)^3} \sum_{i\in\mathcal{O}} \Big[\langle u_{\mathbf{k},i}|e^{-i\mathbf{G}\cdot\mathbf{r}} \mathbf{a}_{-\mathbf{G}-\mathbf{q}} \cdot (-i\nabla + \mathbf{k}) \ \mathbf{a}_\mathbf{q} \cdot \frac{\mathrm{d}|u_{\mathbf{k},i}\rangle}{\mathrm{d}\mathbf{k}} \\ &\quad + \langle u_{\mathbf{k},i}|\mathbf{a}_{-\mathbf{G}-\mathbf{q}} \cdot (-i\nabla + \mathbf{k}) e^{-i\mathbf{G}\cdot\mathbf{r}} \ \mathbf{a}_\mathbf{q} \cdot \frac{\mathrm{d}|u_{\mathbf{k},i}\rangle}{\mathrm{d}\mathbf{k}} \\ &\quad + \frac{\mathrm{d}\langle u_{\mathbf{k},i}|}{\mathrm{d}\mathbf{k}} \cdot \mathbf{a}_\mathbf{q} \ \mathbf{a}_{-\mathbf{G}-\mathbf{q}} \cdot (-i\nabla + \mathbf{k}) e^{-i\mathbf{G}\cdot\mathbf{r}} |u_{\mathbf{k},i}\rangle \\ &\quad + \frac{\mathrm{d}\langle u_{\mathbf{k},i}|}{\mathrm{d}\mathbf{k}} \cdot \mathbf{a}_\mathbf{q} \ e^{-i\mathbf{G}\cdot\mathbf{r}} \mathbf{a}_{-\mathbf{G}-\mathbf{q}} \cdot (-i\nabla + \mathbf{k})|u_{\mathbf{k},i}\rangle \Big] \ . \end{aligned} \tag{5.29}$$

An integration by parts then leads to

$$f(\mathbf{a}_\mathbf{q}, \mathbf{a}_{-\mathbf{G}-\mathbf{q}}, \mathbf{G}, \mathbf{0}) = -2 \int \frac{\mathrm{d}^3k}{(2\pi)^3} \sum_{i\in\mathcal{O}} \langle u_{\mathbf{k},i}|e^{-i\mathbf{G}\cdot\mathbf{r}} \mathbf{a}_{-\mathbf{G}-\mathbf{q}} \cdot \mathbf{a}_\mathbf{q}|u_{\mathbf{k},i}\rangle \ . \tag{5.30}$$

Using (5.30), one can rewrite (5.22) as:

$$\left.\frac{\partial^2 E}{\partial B_0 \partial B_{-\mathbf{G}}}\right|_{\mathbf{B}=\mathbf{0}} = \lim_{q\to 0} \left[f(\mathbf{a}_\mathbf{q}, \mathbf{a}_{-\mathbf{G}-\mathbf{q}}, \mathbf{G}, \mathbf{q}) - f(\mathbf{a}_\mathbf{q}, \mathbf{a}_{-\mathbf{G}-\mathbf{q}}, \mathbf{G}, \mathbf{0}) \right] \ . \tag{5.31}$$

Still, the two terms in (5.31) diverge, since f is linear in the divergent arguments $\mathbf{a}_\mathbf{q}$ and $\mathbf{a}_{-\mathbf{G}-\mathbf{q}}$. However, the divergences can be handled by using the linearity in the first two arguments, and Eq. (5.6):

$$\begin{aligned} \left.\frac{\partial^2 E}{\partial B_0 \partial B_{-\mathbf{G}}}\right|_{\mathbf{B}=\mathbf{0}} &= \lim_{q\to 0} \frac{1}{c^2|\mathbf{q}||\mathbf{G}+\mathbf{q}|^2} \Big[f(\hat{\mathbf{q}} \times \hat{\mathbf{b}}_\mathbf{q}, (\mathbf{G}+\mathbf{q}) \times \hat{\mathbf{b}}_{-\mathbf{G}-\mathbf{q}}, \mathbf{G}, \mathbf{q}) \\ &\qquad - f(\hat{\mathbf{q}} \times \hat{\mathbf{b}}_\mathbf{q}, (\mathbf{G}+\mathbf{q}) \times \hat{\mathbf{b}}_{-\mathbf{G}-\mathbf{q}}, \mathbf{G}, \mathbf{0}) \Big] \ , \end{aligned} \tag{5.32}$$

or, for $\mathbf{G} \neq \mathbf{0}$, this can be written as a first derivative:

$$\left.\frac{\partial^2 E}{\partial B_{\mathbf{0}} \partial B_{-\mathbf{G}}}\right|_{\mathbf{B}=\mathbf{0}} = \left.\frac{\partial}{c^2 G^2 \partial q} f(\hat{\mathbf{q}} \times \hat{\mathbf{b}}_{\mathbf{0}}, \mathbf{G} \times \hat{\mathbf{b}}_{-\mathbf{G}}, \mathbf{G}, q\hat{\mathbf{q}})\right|_{q=0} . \tag{5.33}$$

In the current implementation, the derivative is computed by finite differences using the following numerically convenient form:

$$\begin{aligned} &\left.\frac{\partial^2 E}{\partial B_{\mathbf{0}} \partial B_{-\mathbf{G}}}\right|_{\mathbf{B}=\mathbf{0}} = \\ &\lim_{q \to 0} \frac{1}{2c^2 |\mathbf{q}||\mathbf{G}|^2} \left[f(\hat{\mathbf{q}} \times \hat{\mathbf{b}}_{\mathbf{0}}, \mathbf{G} \times \hat{\mathbf{b}}_{-\mathbf{G}}, \mathbf{G}, q\hat{\mathbf{q}}) - f(\hat{\mathbf{q}} \times \hat{\mathbf{b}}_{\mathbf{0}}, \mathbf{G} \times \hat{\mathbf{b}}_{-\mathbf{G}}, \mathbf{G}, -q\hat{\mathbf{q}}) \right] . \end{aligned} \tag{5.34}$$

Likewise, the $\mathbf{G} = \mathbf{0}$ component is obtained by taking the limit:

$$\begin{aligned} \left.\frac{\partial^2 E}{\partial B_{\mathbf{0}} \partial B_{\mathbf{0}}}\right|_{\mathbf{B}=\mathbf{0}} &= \lim_{q \to 0} \frac{1}{2c^2 |\mathbf{q}|^2} \Big[f(\hat{\mathbf{q}} \times \hat{\mathbf{b}}_{\mathbf{0}}, \hat{\mathbf{q}} \times \hat{\mathbf{b}}_{\mathbf{0}}, \mathbf{0}, q\hat{\mathbf{q}}) + f(\hat{\mathbf{q}} \times \hat{\mathbf{b}}_{\mathbf{0}}, \hat{\mathbf{q}} \times \hat{\mathbf{b}}_{\mathbf{0}}, \mathbf{0}, -q\hat{\mathbf{q}}) \\ &\qquad - 2 f(\hat{\mathbf{q}} \times \hat{\mathbf{b}}_{\mathbf{0}}, \hat{\mathbf{q}} \times \hat{\mathbf{b}}_{\mathbf{0}}, \mathbf{0}, \mathbf{0}) \Big] \\ &= \left.\frac{\partial^2}{2c^2 \partial q^2} f(\hat{\mathbf{q}} \times \hat{\mathbf{b}}_{\mathbf{0}}, \hat{\mathbf{q}} \times \hat{\mathbf{b}}_{\mathbf{0}}, \mathbf{0}, q\hat{\mathbf{q}})\right|_{q=0} . \end{aligned} \tag{5.35}$$

By using the sum rule (5.30), the "diamagnetic" first and "paramagnetic" second term in (5.22) are treated on an equal footing, thereby removing the gauge-invariance problems that have plagued some of the early quantum chemistry calculations. If the diamagnetic and paramagnetic terms were treated separately, numerical errors due to e.g. insufficient basis set convergence could affect the diamagnetic and paramagnetic terms differently, resulting in a dependence on the gauge.

5.6 Implementation using pseudopotentials and plane waves

The preceding theory is rather general, and applies to any system described by a density functional of the form (5.15). For the calculations presented in this thesis, only the magnetic response of valence electrons will be considered. The ionic cores are described by norm conserving pseudopotentials [55] in the Kleinman-Bylander form [71]. This approximation does not affect σ of the nuclei without core electrons, such as H, but those containing core electrons. In the latter case σ computed with pseudopotentials differs from the one computed with an all-electron scheme by three different terms: i) the diamagnetic core contribution, which is independent of the chemical environment; ii) a contribution due to the transitions from valence states to core states [99]; iii) a contribution due to the difference between the all-electron valence wave functions and the pseudo wave functions in the core region. By numerical experiment, one finds that, for first row atoms, the terms ii) and iii) are usually much smaller than the range of variation of σ with the chemical environment. Finally, in pseudopotential calculations, the operator $(-i\nabla + \mathbf{k} + \mathbf{q}/2)$ in Eq. (5.25) is replaced by $(\mathbf{v}^p_{\mathbf{k}} + \mathbf{v}^p_{\mathbf{k}+\mathbf{q}})/2$, where $\mathbf{v}^p_{\mathbf{k}} = (d/d\mathbf{k}) H^p_{\mathbf{k}}$ is the velocity operator, and $H^p_{\mathbf{k}}$ is the pseudo-Hamiltonian. By trial and error, this turned out to give improved agreement with quantum-chemistry all-electron calculations. Work on a better theoretical foundation for handling the nonlocal pseudopotential operator is in progress.

	σ-theory (ppm)	σ-experiment (ppm)
H_2	25.9	26.2[a]
CH_4	30.7	30.61[a]
C_2H_6	29.7	29.86[b]
C_2H_4	24.5	25.43[b]
C_2H_2	28.6	29.26[b]

Table 5.1: Computed and measured H chemical shifts (σ) in parts per million (ppm) for a set of free molecules. [a]Ref.[106], [b]Ref.[107].

With the usual plane-wave expansion of the wave functions, the computational cost to compute σ is comparable to the effort of computing the total energy in LDA-DFT. Both schemes scale with the third power in the number of atoms in the unit cell.

5.7 Test calculations on molecules

In order to test the new method, the hydrogen chemical shifts for a set of small molecules are computed. A local pseudopotential of the Kerker type [36] with a cutoff radius of $r_c = 1.0$ a.u. is used for hydrogen. For carbon, a Troullier-Martins [55] pseudopotential with $r_c = 1.1$ a.u. and a non-local s-projector of the Kleinman-Bylander type [71] is employed. An energy cutoff of 70 Ry for the plane wave expansion is sufficient. To simulate the molecules as periodic systems, a supercell geometry is used, and the size of the supercell is increased until the error in σ due to the periodic replica is less than 0.1 parts per million (ppm).

The results for a set of molecules are reported in Table 5.1. All the computed values are in excellent agreement with experimental data. The discrepancies are larger for C_2H_4 and C_2H_2, in which a double and a triple C-C bond exist, respectively. This could indicate a relatively larger inaccuracy of LDA in describing these types of bonds. Similar agreement with experiments for the hydrogen σ in molecules was found in previous quantum-chemistry calculations [106, 105].

Chapter 6

NMR chemical shift of diamond and amorphous carbon

6.1 Introduction

Polycrystalline diamond thin films, grown by chemical vapor deposition (CVD), and diamond-like amorphous carbon thin films possess the outstanding physical properties of bulk diamond, such as high thermal conductivity, hardness, chemical inertness, and optical transparency in the infrared region. Their possible applications include wear-resistant coatings and thin-film semiconductor devices. E.g., diamond-like amorphous carbon is currently used as a protective layer in magnetic disks. Considerable efforts have been undertaken to understand the microscopic structure of these films. Nuclear magnetic resonance (NMR) is becoming increasingly important in this investigation; especially for the characterization of amorphous carbon [95, 108, 109, 110, 111, 112, 113, 114, 115], but also for the study of CVD diamond [116, 117, 118]. In this chapter we present the first *ab initio* calculations of carbon chemical shifts in crystalline and amorphous solids. We compute the chemical shift spectra of diamond, CVD diamond, and diamond-like amorphous carbon with and without hydrogen. Our results are in excellent agreement with experiments, and are useful for the interpretation of NMR spectra in terms of the microscopic structure of the materials.

6.2 Notation and tests

The isotropic chemical shift $\sigma = \mathrm{Tr}[\overleftrightarrow{\sigma}]/3$ is calculated as described in chapter 5. We denote with H σ the chemical shifts at the hydrogen nuclei, and with C σ the chemical shifts at the carbon nuclei. A norm-conserving pseudopotential [55] in the Kleinman-Bylander form [71] with a cut-off radius of $r_c = 1.1$ a.u. is used. For H, we adopt a purely local pseudopotential whereas for C, a non-local s-projector augments the local potential. The plane-wave basis energy cutoff is 70 Ry. Following the experimental convention, we will quote chemical shifts relative to the standard reference system of liquid tetramethylsilane TMS at room temperature,

$$\delta_{\mathrm{TMS}}(\mathrm{sample}) = -[\sigma(\mathrm{sample}) - \sigma(\mathrm{TMS})], \tag{6.1}$$

where σ is the absolute chemical shift measured for a spherical shape. Because of the pseudopotential approximation used, we do not compute σ(TMS), but rather for the H δ_{TMS}, we use the experimental value of H $\sigma(\mathrm{TMS}) = 30.97$ ppm, and, for the C δ_{TMS}, we fix C σ(TMS) by imposing that the computed value of C δ_{TMS} for gas CH_4 is equal to the experimental value of -11 ppm [119]. H σ(TMS) can be obtained from H σ of gas CH_4, [120] from the relative shift between gas CH_4 and gas TMS [121], and from the relative shift between gas TMS and liquid TMS [122].

The accuracy of our method for the H σ has been shown in chapter 5. In Table 6.1 we validate our approach for the C δ_{TMS} in a set of free hydrocarbons. The molecular structures are taken from experiments. In C_6H_6 $r_{\mathrm{CH}} = 1.101$ Å, $r_{\mathrm{CC}} = 1.399$ Å. For the other geometries see [100]. Table 6.1 shows that the chemical shift is sensitive to the C hybridization. The agreement between theory

	δ_{TMS}-theory [ppm]	δ_{TMS}-experiment [ppm]
C_2H_6	5.3	3.2
C_2H_4	109.4	119.6
C_2H_2	60.6	66.9
C_6H_6	110.0	126.9

Table 6.1: Computed and measured [119] C chemical shifts (δ_{TMS}) for a set of hydrocarbons in the gas phase.

V (a.u.^{3})	δ_{TMS}-theory [ppm]	δ_{TMS}-experiment [ppm]
67	19.37	
70	24.52	
73	29.69	
76.761	36.17	34.54
79	40.00	

Table 6.2: Computed and measured [116] C chemical shifts (δ_{TMS}) for the diamond crystal as a function of the unit cell volume V. The experimental equilibrium V is 76.761 a.u.^{3}.

and experiment indicates that in C the error due to the pseudopotential approximation is minor. Similar results for these *finite* systems have been obtained in Ref. [106].

6.3 CVD diamond

In Table 6.2 we present our results for C δ_{TMS} in crystalline diamond as a function of the unit cell volume (V). At the equilibrium volume, the experimental and theoretical data are in excellent agreement. Within the range considered, δ_{TMS} varies linearly with the volume, and $\mathrm{d}\delta_{\mathrm{TMS}}/\mathrm{d}V = 1.72$ ppm/a.u.^{3}. From the value of the bulk modulus in diamond, we obtain the variation of δ_{TMS} with the applied pressure P, $\mathrm{d}\delta_{\mathrm{TMS}}/\mathrm{d}P = 0.30$ppm/GPa. With this information, δ_{TMS} could be used as a pressure gauge in diamond.

Our results are useful to determine the mechanism for the NMR and Raman line-width in polycrystalline CVD diamond, where the Raman shift (Ω) measures the optical phonon frequency at the zone center. The Raman line-width ($\Delta\Omega$) is often used to characterize the quality of the CVD diamond films. Indeed, a correlation between $\Delta\Omega$ and the size, the regularity and the optical transparency of the films [123, 116], have been observed. Alternatively, one can use the NMR line-width ($\Delta\delta_{\mathrm{TMS}}$) since a strong correlation between the two line-widths has also been observed [116] (see Fig. 6.1). The microscopic source of these line broadenings is still unclear. Two mechanisms have been proposed [123, 116]:

1. The broadenings are related to the presence of defects; $\Delta\Omega^{-1}$ is proportional to the phonon lifetime which is reduced by the scattering with the defects, and $\Delta\delta_{\mathrm{TMS}}$ is determined by the paramagnetic perturbation given by the defects.

2. The broadenings are due to local fluctuations in the stress (ΔP). In this case both $\Delta\Omega$ and $\Delta\delta_{\mathrm{TMS}}$ would be proportional to ΔP, and $\Delta\Omega = c\Delta\delta_{\mathrm{TMS}}$, where $c = |\mathrm{d}\Omega/\mathrm{d}P||\mathrm{d}\delta_{\mathrm{TMS}}/\mathrm{d}P|^{-1}$.

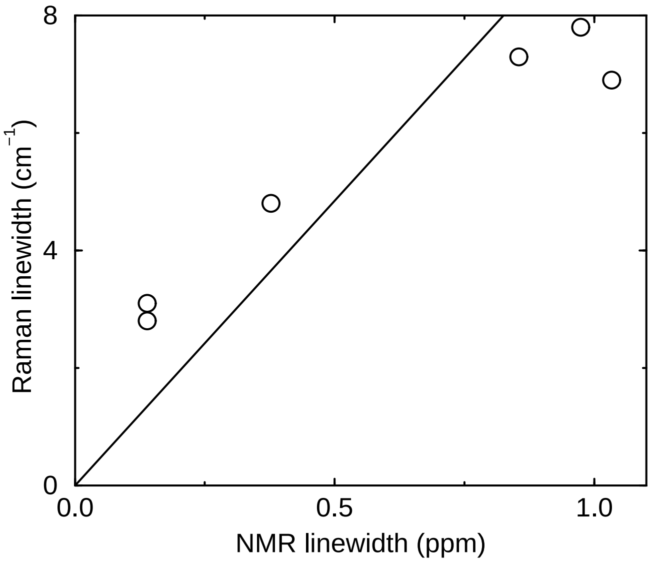

Figure 6.1: Raman versus NMR line width in CVD diamond. The circles are experimental points obtained for different samples [116]. The line is the result of our theoretical model based on stress/volume fluctuations.

While we cannot rule out mechanism 1), we can verify *quantitatively* if mechanism 2) is a possible explanation. In this case, using the value for $\mathrm{d}\Omega/\mathrm{d}P$ from Ref. [124], we obtain $\Delta\Omega = \Delta\delta_{\mathrm{TMS}} \times 9.7\mathrm{cm}^{-1}/\mathrm{ppm}$. This linear relationship is shown in Fig. 6.1, along with the experimental data. The agreement between the theoretical data and experiment supports that stress fluctuations are the dominant source of line broadening for NMR and Raman experiments. Here we have assumed that the stress fluctuations are hydrostatic. Note that in diamond (a cubic crystal), a pure shear fluctuation would broaden the Raman line but not the NMR line. Indeed, a pure shear splits the three-fold degenerate Raman line, but does not shift δ_{TMS} up to linear order in the deformation.

6.4 Amorphous carbon

Finally, we discuss our results for amorphous C. To compute the NMR spectra of amorphous C we use atomic geometries generated by *ab initio* molecular dynamics simulations. We consider two different samples: a hydrogenated sample, at a density of 2.2 g/cm^3, with 64 C atoms and 12 H atoms (16 at.%) in a cubic supercell [125], and a pure-C sample, at a density of 2.9 g/cm^3, with 64 C atoms [126]. Note that the value of the density given in reference [125] is miscomputed. We compute H and C δ_{TMS}, and compare our results with experimental data obtained on two similar samples: a hydrogenated sample, at a density of 1.8 g/cm^3, with 35 at.% of H [95], and a pure-C sample at a density of 2.9 g/cm^3 [108]. From the amount of 4-fold coordinated C and the H content, these samples qualify as hard diamond-like films. To obtain continuous spectra, we use a Gaussian broadening with a standard deviation of 1 ppm and 6 ppm for H and C, respectively.

The experimental [95] and theoretical H δ_{TMS} spectra for the hydrogenated samples are presented in Fig. 6.2. In the experimental spectrum two distinct types of H have been identified [95]. The two types are characterized by two different nuclear relaxation times, and are spatially separated. The experimental spectra, decomposed into slowly and fast relaxing H, are also shown in Fig. 6.2. In Ref. [95], the fast relaxing H, which have an average δ_{TMS} of $\sim$ 5 ppm, have been assigned to H groups in a *sp*^{2}-*sp*^{3} C network. The slowly relaxing H, with an average δ_{TMS} of $\sim$ 2 ppm, have been assigned to polymeric $(\mathrm{CH}_2)_{\mathrm{n}}$ chains. A two component spectrum has also been measured in Ref. [109]. However, here the peaks at 5 ppm and 2 ppm have been attributed to H bonded to *sp*^{2} and *sp*^{3} C, respectively. These assignments are based on a comparison with the H δ_{TMS} of hydrocarbons. Our theoretical spectrum is in excellent agreement with the experimental spectrum of the fast relaxing H. Our sample does not contain CH_2 groups; the C are instead arranged in a *sp*^{2}-*sp*^{3} C network in which 11 H are bonded to *sp*^{3} C and 1 H is bonded to a *sp*^{2} C. Thus our results *support* the assignments of Ref. [95]. They are *incompatible* with the assignments of Ref. [109], which would predict for our sample a peak at 2 ppm.

In Fig. 6.3, we show the C δ_{TMS} spectrum for the hydrogenated sample, which we compare with the experimental data [95]. We decompose the theoretical spectrum into contributions coming from the 3-fold (*sp*^{2}) and 4-fold (*sp*^{3}) coordinated atoms, with and without a bond to a H. A cut-off distance of 1.9 Å and of 1.4 Å is used to define a C-C and a C-H bond, respectively. This decomposition confirms the general expectation [95, 108, 109] that *sp*^{2} C atoms experience a larger δ_{TMS} than the *sp*^{3} C atoms. Notice however that the position of the *sp*^{3} peak is at 75 ppm, substantially deviating from the diamond resonance at 36 ppm. Within the *sp*^{3} peak, we can further distinguish the contribution due to hydrogenated C atoms, which exhibit a smaller δ_{TMS}. Hence increasing hydrogenation will move the *sp*^{3} peak peak to smaller δ_{TMS}. We have excellent agreement between theory and experiment in the location and in the shape of the peaks. The relative weight of the peaks is different because the theoretical and experimental samples have a different H content and *sp*^{2}/*sp*^{3} ratio.

For the pure C samples, we show the experimental and theoretical C δ_{TMS} spectra in Fig. 6.4. As for the hydrogenated sample, we decompose the theoretical spectrum into contributions from *sp*^{2} and *sp*^{3} bonded atoms. Again we observe good agreement between theory and experiment. However, in the experimental spectrum, there is a shoulder for $\delta_{\mathrm{TMS}} > 150$, which is not present in the theoretical pure C spectrum nor in the hydrogenated spectra.

In the theoretical spectra of the two samples, there is a small isolated peak at about 200 ppm. In the hydrogenated sample this peak stems from an *sp*^{2} atom bonded to three *sp*^{3} neighbors. In the pure carbon sample the peak is caused by a *sp*^{2} atom bonded to two *sp*^{3} neighbors and to one *sp*^{2} neighbor with its *sp*^{2} plane tilted by 90^0. In both cases the peaks originate from *sp*^{2} atoms where the *p* orbital does not contribute to a π bond. This leads to a localized defect level in the gap with a paramagnetic shift. The immediate neighbors also experience a paramagnetic shift, but

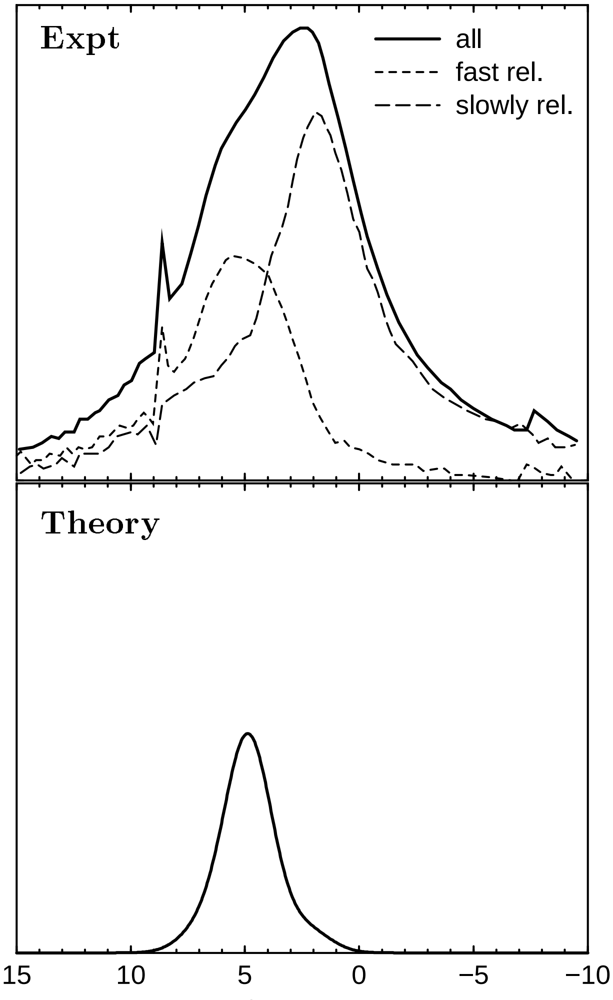

Figure 6.2: H chemical shift spectra in hydrogenated amorphous carbon. The upper panel shows the experimental data from Ref. [95]. Along with the raw spectrum, in which all the H are probed (all), the spectrum of the fast relaxing H (fast rel.), and the spectrum of slowly relaxing H (slowly rel.) are depicted. The lower panel shows the results of our *ab initio* calculation.

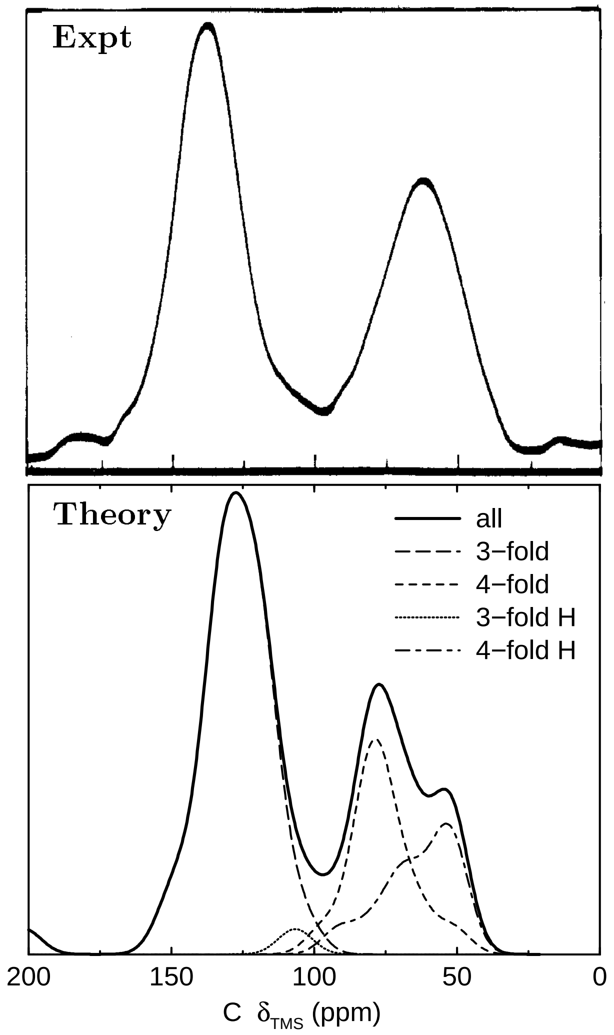

Figure 6.3: C chemical shift spectra in hydrogenated amorphous carbon. The upper panel shows the experimental data [95]. The lower panel shows the calculated spectrum. We decompose the theoretical spectrum (all), into contributions from the 3-fold and 4-fold coordinated atoms not bonded to an H (3-fold and 4-fold), and the atoms bonded to an H (3-fold H and 4-fold H).

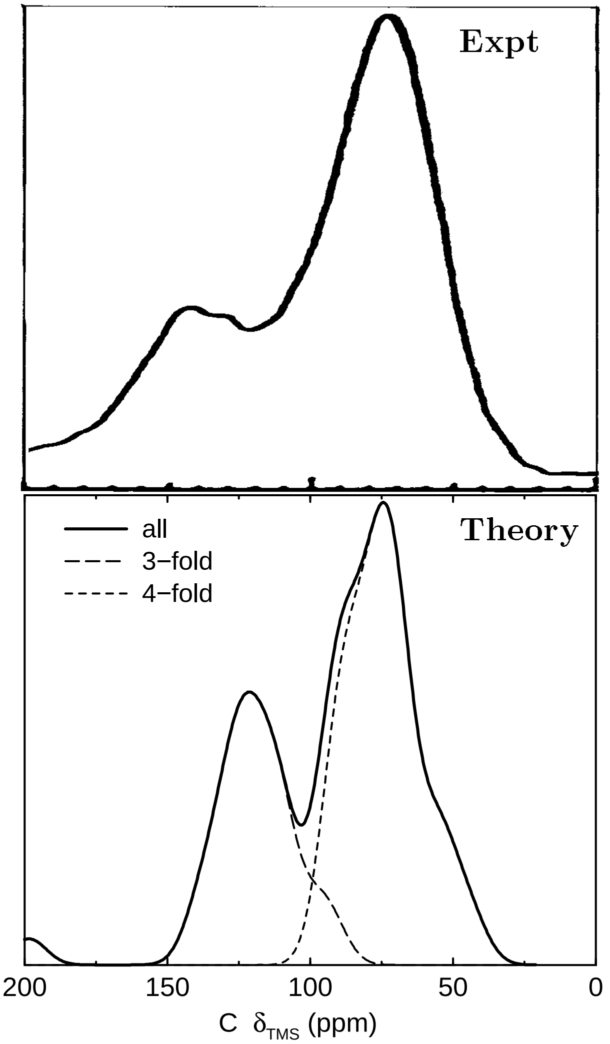

Figure 6.4: C chemical shift spectra in pure amorphous carbon. The upper panel shows the experimental data [108]. The lower panel shows the calculated spectrum. We decompose the theoretical spectrum (all), into contributions from the 3-fold and 4-fold coordinated atoms (3-fold and 4-fold).

already the second shell atoms are affected only marginally, demonstrating the locality of δ_{TMS} in the amorphous phase. Finally in the hydrogenated sample there is one twofold-coordinated atom with an even more paramagnetic shift of $\delta_{\mathrm{TMS}} = 326$ ppm (not shown in Fig. 6.3).

6.5 Conclusion

In conclusion, for the first time, a NMR chemical shift spectra calculation of real materials in the crystalline and amorphous phases has been performed. The excellent agreement of the calculated spectra with experiments, and the size of the samples that can be studied, establish the method presented in chapter 5 as a useful tool for the interpretation of NMR spectra in solid state physics, chemistry and material science. We show that the Raman and NMR line broadening in polycrystalline CVD diamond can be attributed to stress fluctuations. For hydrogenated amorphous carbon, the computed H spectrum indicates that an assignment of H chemical shifts based on a comparison with the hydrocarbon spectra is incorrect. Instead, we support a heterogeneous model[95], according to which the experimental amorphous samples are a mixture of two spatially separated phases; a sp^2-sp^3 C network and a polymeric $(\mathrm{CH}_2)_\mathrm{n}$ chain structure. Finally, we confirm that like in molecules, the C chemical shifts in the amorphous phase are mostly determined by the C coordination.

Chapter 7

Surface state effects on the NMR chemical shift

7.1 Introduction

In the bulk of a crystal, as a general consequence of lattice periodicity, the electronic states are extended. At a surface however, the translational symmetry of the crystal is broken, and localized electronic states, which are forbidden in the bulk, can exist. These surface states decay exponentially from the surface into the bulk, and play an important role in the electronic, chemical, and structural properties of the surface. They can be detected by surface-sensitive experimental techniques, e.g. with X-ray photoemission spectroscopy, ultraviolet photoelectron spectroscopy, or scanning tunneling microscopy. However, to our knowledge, only indirect experimental observations of the surface states' decay have been reported [127]. In this chapter we present an *ab initio* calculation of the ^{13}C nuclear magnetic resonance (NMR) chemical shifts of a diamond surface, using the theory developed in chapter 5. In the atomic layers close to the surface, we find surprisingly strong variations of the chemical shift, which are proportional to the probability density of an unoccupied surface state decaying into the bulk. Using this effect, it is then possible to measure directly the decay length of the surface state with NMR.

The relevance of our theoretical findings is further enhanced by recent experimental advances in surface NMR. To study surfaces with NMR, one needs to selectively amplify the signal from surface atoms. This has been accomplished using optically pumped hyperpolarized gases. The NMR signal is proportional to the population difference in nuclear spin levels. At thermal equilibrium, this difference is usually less than 1 in 10^5, but with optical pumping, it is possible to reach values which are close to unity. These techniques have been used to increase the NMR signal of ^{129}Xe in the gas and solid phases [128], or adsorbed on surfaces [129, 130]. Via cross polarization, the ^{129}Xe polarization can be transfered to other nuclei, such as ^{1}H or ^{13}C [131, 132, 133, 134, 135]. In the case of ^{129}Xe adsorbed on a surface, the polarization is preferentially transfered to the nuclei close to the surface, whose signal is enhanced by many orders of magnitude [132, 133, 134]. Moreover, one can probe nuclei at different distances from the surface by changing the contact time, and thereby the penetration depth of the spin polarization [133, 134].

7.2 NMR chemical shifts on surfaces

A uniform, external magnetic field $\mathbf{B}_{\text{ext}}$ applied to a sample of matter induces an electronic current density $\mathbf{J}(\mathbf{r})$, which gives rise to a non-uniform induced magnetic field, $\mathbf{B}_{\text{ind}}(\mathbf{r})$. As explained in chapter 5, even deep inside the bulk, the chemical shift tensor $\overset{\leftrightarrow}{\sigma}(\mathbf{r})$, depends on the shape of the sample and on the orientation of the external magnetic field. This effect is a signature of macroscopic surface currents. In classical magnetostatics, the surface current is $\mathbf{K} = c\chi\mathbf{B}_{\text{ext}} \times \hat{\mathbf{n}}_{\perp}$, where c is the speed of light, $\hat{\mathbf{n}}_{\perp}$ is the outwardly directed normal to the surface, and χ is the macroscopic magnetic susceptibility [103]. For a flat surface, $K = 0$, if $\mathbf{B}_{\text{ext}}$ is normal to the surface, and $K = c\chi B_{\text{ext}}$, if the field is parallel. As a result, in the bulk far from the surface, the shift differs from that of the standard spherical sample (σ_{sp}); $\sigma_\perp(bulk) = \sigma_{\mathrm{sp}}(bulk) + \frac{8}{3}\pi\chi$, and $\sigma_{||}(bulk) = \sigma_{\mathrm{sp}}(bulk) - \frac{4}{3}\pi\chi$. The subscripts $\perp$ and $||$ denote the diagonal component of $\overleftrightarrow{\sigma}$ in the directions normal and parallel to the surface, respectively. It is an important consistency check for our atomic-scale calculations that inside the bulk, we indeed recover the behavior expected from macroscopic magnetostatics. We are interested here in the *microscopic* surface effects, and therefore focus on the deviation from these asymptotic bulk values at a distance z below the surface,

$$\begin{aligned} \delta_\perp(z) &= \sigma_\perp(z) - \sigma_\perp(bulk), \\ \delta_{||}(z) &= \sigma_{||}(z) - \sigma_{||}(bulk)\ . \end{aligned} \tag{7.1}$$

By symmetry, for the ideal C(111):H surface, $\overleftrightarrow{\sigma}$ is a diagonal tensor when expressed in basis vectors parallel and perpendicular to the surface. For an arbitrary surface, the off-diagonal elements need not vanish.

7.3 Results for the hydrogenated diamond (111) surface

We now consider a particular surface, which is the ideal, hydrogen terminated (111) surface of diamond, C(111):H. The computational procedure is outlined in chapter 5. For C and H, the same pseudopotentials are used as in chapter 6. The wave functions are expanded in plane waves up to an energy cut-off of 70 Ry. For Brillouin-zone integrations, we use 15 special k-points in the irreducible wedge of the Brillouin zone. To model the surface, a periodically repeated diamond slab of 20 C layers is used, with a (111) hydrogenated ideal surface on each side. The unit cell is hexagonal and contains twenty C atoms and two H atoms. The length of the hexagonal lattice constant a is equal to 2.503 Å, such that the C bond lengths in the center of the slab are equal to the computed bond length of bulk diamond (1.533 Å). After relaxing the slab by minimizing its total energy, the distance between the H and C layer is 1.116 Å. The distance between the first and second C layer contracts to 0.479 Å, which is 6% less than the corresponding bulk value. Negligible relaxations of less than 1% are observed for the deeper layers.

The results of our calculation for the slab are presented in Fig. 7.1, where for each C layer we plot $\delta_{||}(z)$ and $\delta_\perp(z)$ as a function of the distance z from the H layer. With increasing z into the crystal, the shift approaches the bulk value, and $\delta_{||}(z)$ and $\delta_\perp(z)$ converge to zero. As Fig. 7.1 shows, $\delta_\perp(z)$ is positive, i.e. a diamagnetic shift, and decays rapidly. When the field is parallel to the surface, the results are different and quite unexpected. We find that $\delta_{||}$ is negative, i.e. a paramagnetic shift, and decays to zero much more slowly. Even five C layers deep into the bulk, $\delta_{||}$ is still -1.9 parts per million (ppm), a magnitude which can be detected experimentally. The large $\delta_{||}$ for the subsurface layers can *not* be explained by a structural relaxation mechanism, since just the first C layer relaxes significantly. We also note that $\delta_{||}$ of the even layers is essentially zero, and only the odd layers show a slowly decaying $\delta_{||}$. Finally, at the first layer, the change in the isotropic shift $\delta = (2\delta_{||} + \delta_\perp)/3$ is -18.9 ppm. This paramagnetic shift is contrasted by trends observed in saturated hydrocarbons and in amorphous carbon, where a replacement of a C-C single bond by a C-H bond moves the isotropic shift by between +2 and +13 ppm [136, 106], i.e. in the opposite direction.

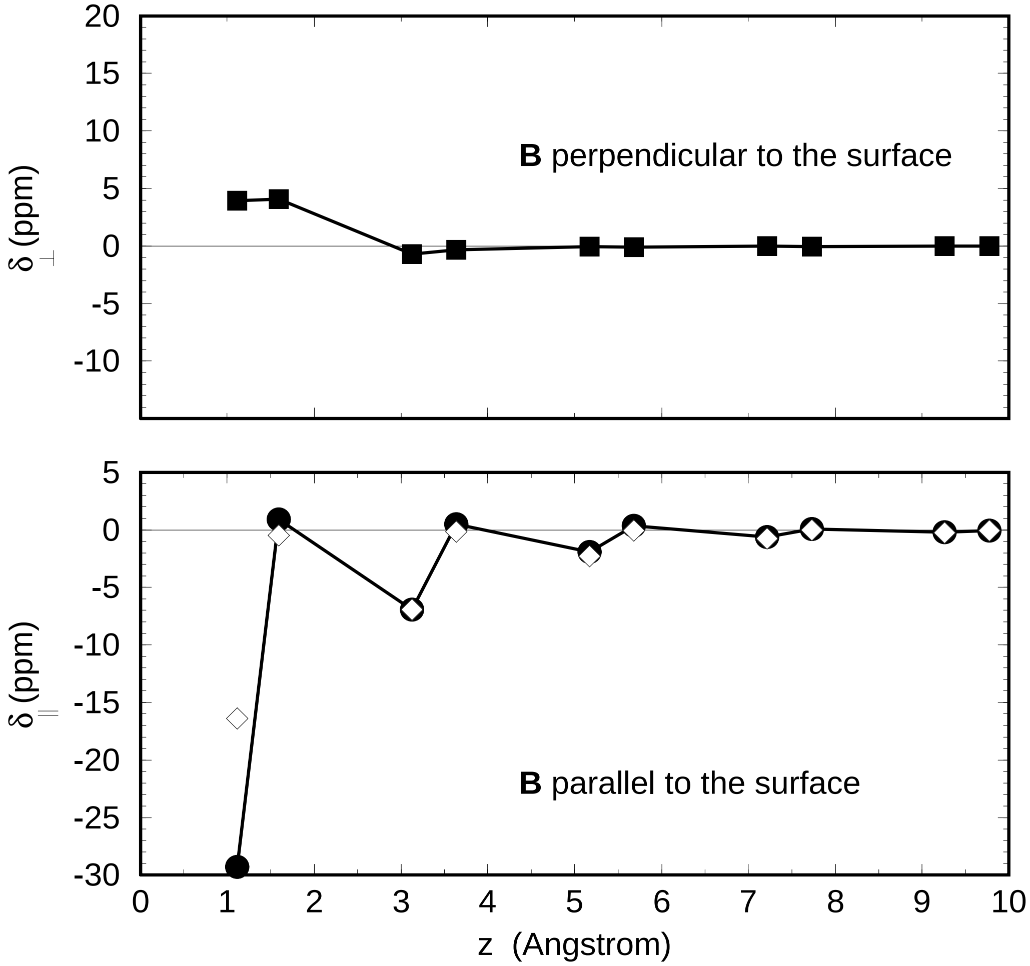

Figure 7.1: The deviations of the chemical shift from the bulk value, $\delta_{||}(z)$ (circles) and $\delta_{\perp}(z)$ (squares) are plotted for each C layer as a function of the distance z from the H layer. We also plot $-\rho(z)$ (diamonds), where $\rho(z)$ is the square amplitude of the surface state at the Γ point, integrated over an atomic sphere centered at each C site. The scale for ρ is chosen in such a way that, at the third layer, $-\rho(z)$ and $\delta_{||}(z)$ coincide. Notice the close agreement between the two quantities. The lines are guides for the eye.

7.4 Analysis

To understand these surprising results, we consider the current density induced by an external magnetic field parallel to the surface. To isolate the effect of the surface, we plot in Fig. 7.2 the difference $\Delta\mathbf{J}(\mathbf{r})$ between the slab and the bulk current density. The bulk $\mathbf{J}(\mathbf{r})$ is generated by taking the current density from the central two layers, and periodically replicating it everywhere. From the figure we see that $\Delta\mathbf{J}(\mathbf{r})$ is localized on circular orbits around the atoms. Moreover, we find $\Delta\mathbf{J}(\mathbf{r})$ to be negligible on all the odd layers, in coincidence with a vanishing $\delta_{||}(z)$. These observations indicate that $\delta_{||}(z)$ for a given atom is mostly determined by induced currents around that same atom.

The trends observed for $\delta_{\perp}(z)$, $\delta_{||}(z)$, and $\Delta\mathbf{J}(\mathbf{r})$ are related to the electronic structure of the surface. Experimentally, the C(111):H surface exhibits a negative electron affinity [137], i.e. the conduction band minimum is found to be 0.7 eV above the vacuum level. DFT-LDA reproduces this property [138]. In our calculation, the conduction band minimum and the valence band maximum are 0.76 eV above and 3.41 eV below the vacuum level, respectively (the DFT-LDA fundamental gap being 4.17 eV). Furthermore, we find a non-degenerate, empty surface state band with a minimum at the Γ point of the Brillouin zone, 0.80 eV below the vacuum level. No occupied surface states are present. These results are depicted in Fig. 7.3. The plane in which the surface state density reaches its largest value is *not* located on a surface atom, but in the vacuum, 1.4 Å away from the H plane. Indeed the surface band originates from vacuum free electron states that are attracted by the tail of the potential near the surface. This kind of surface states are a general feature of negative electron affinity surfaces, and are also observed in BN graphitic sheets [139].

To understand the role of the surface states, we analyze the chemical shift by partitioning it into a diamagnetic and a paramagnetic term [106], $\sigma_{\hat{\mathbf{n}}} = \sigma^{\mathrm{d}}_{\hat{\mathbf{n}}} + \sigma^{\mathrm{p}}_{\hat{\mathbf{n}}}$, where $\sigma_{\hat{\mathbf{n}}}$ is the diagonal element of the tensor $\overset{\leftrightarrow}{\sigma}$ in the direction $\hat{\mathbf{n}}$, and

$$\sigma^{\mathrm{d}}_{\hat{\mathbf{n}}} = \frac{e^2}{mc^2}\sum_i^{\mathrm{occ}}\langle\psi_i|\frac{r^2-(\mathbf{r}\cdot\hat{\mathbf{n}})^2}{r^3}|\psi_i\rangle \tag{7.2}$$

$$\sigma^{\mathrm{p}}_{\hat{\mathbf{n}}} = -\frac{2e^2}{m^2c^2}\sum_i^{\mathrm{occ}}\sum_j^{\mathrm{emp}}\frac{\langle\psi_i|\hat{\mathbf{n}}\cdot\mathbf{L}|\psi_j\rangle\langle\psi_j|r^{-3}\hat{\mathbf{n}}\cdot\mathbf{L}|\psi_i\rangle}{\varepsilon_j-\varepsilon_i}. \tag{7.3}$$

Here $|\psi_k\rangle$ are the eigenstates of the Hamiltonian for the electrons with eigenenergies ε_k, the indices i and j run over the empty and occupied states, respectively, and $\mathbf{r}$ and $\mathbf{L}$ are the position and the angular momentum operators relative to the nucleus for which σ is computed. In principle, Eqs. (7.2) and (7.3) hold only in a finite system, since in an infinite solid $\sigma^{\mathrm{d}}_{\hat{\mathbf{n}}}$ and $\sigma^{\mathrm{p}}_{\hat{\mathbf{n}}}$ individually diverge due to the contributions at large r. However, we have shown that the deviation of $\sigma_{||}(z)$ from its bulk value for a given atom originates from variations of the current density, $\Delta\mathbf{J}(\mathbf{r})$, localized around that same atom. This justifies an estimation of $\sigma(z) - \sigma(bulk)$ by means of Eqs. (7.2) and (7.3), with the spatial integrations restricted to the vicinity of the atom for which $\sigma(z)$ is measured. The diamagnetic term $\sigma^{\mathrm{d}}_{\hat{\mathbf{n}}}$ is always positive, whereas $\sigma^{\mathrm{p}}_{\hat{\mathbf{n}}}$ is usually negative. The presence of empty surface states in the gap increases the paramagnetic term $\sigma^{\mathrm{p}}_{\hat{\mathbf{n}}}$, since the surface states lie below the bulk conduction band, and hence the energy denominators in Eq. (7.3) become smaller. In particular, for the extra surface state contributions, the numerator of Eq. (7.3) would be roughly proportional to the square amplitude of the surface states on the atomic site. The diamagnetic term $\sigma^{\mathrm{d}}_{\hat{\mathbf{n}}}$, which depends on occupied orbitals only, is not affected by empty surface states.

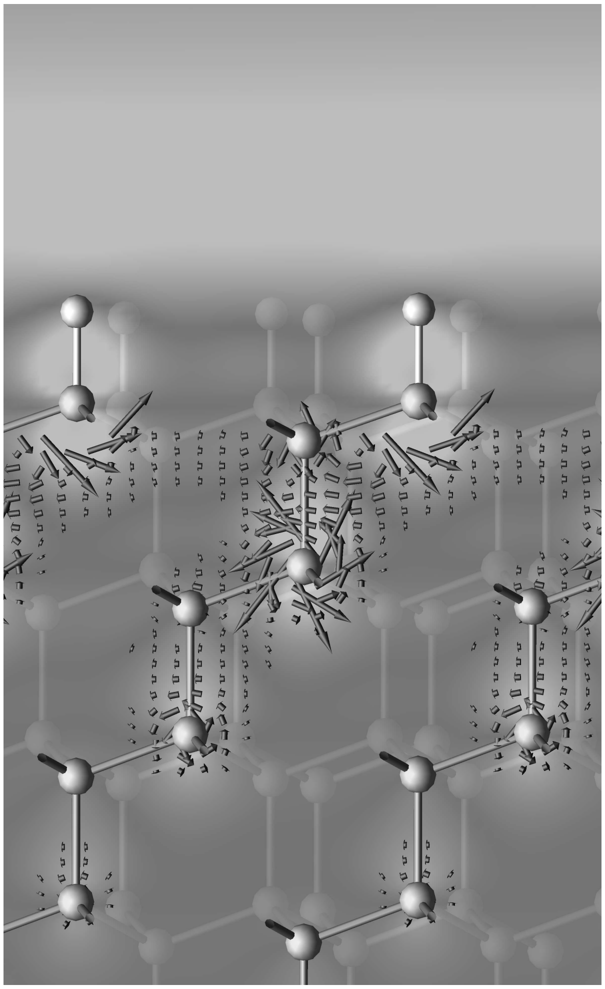

Figure 7.2: Current density induced by an external magnetic field $\mathbf{B}_{\text{ext}}$ parallel to the surface in the $(11\bar{2})$ direction (coming out of the page). We show the current density in the $(1\bar{1}0)$ plane containing the H atoms. Plotted is the difference $\Delta\mathbf{J}(\mathbf{r})$ between the slab and the bulk $\mathbf{J}(\mathbf{r})$. $\Delta\mathbf{J}(\mathbf{r})$ is not shown above the top C layer, which experiences a different chemical environment since it is bonded to the H layer. The grey scale coded density plot visualizes the square modulus of the surface state at the Γ point. Dark corresponds to low and bright to high density. One can recognize the characteristic p_z shape of this state, which leads to the different behavior of $\delta_{\perp}(z)$ and $\delta_{||}(z)$ shown in Fig. 7.1. Notice that $\Delta\mathbf{J}(\mathbf{r})$ is larger around the atoms on which the surface state resides.

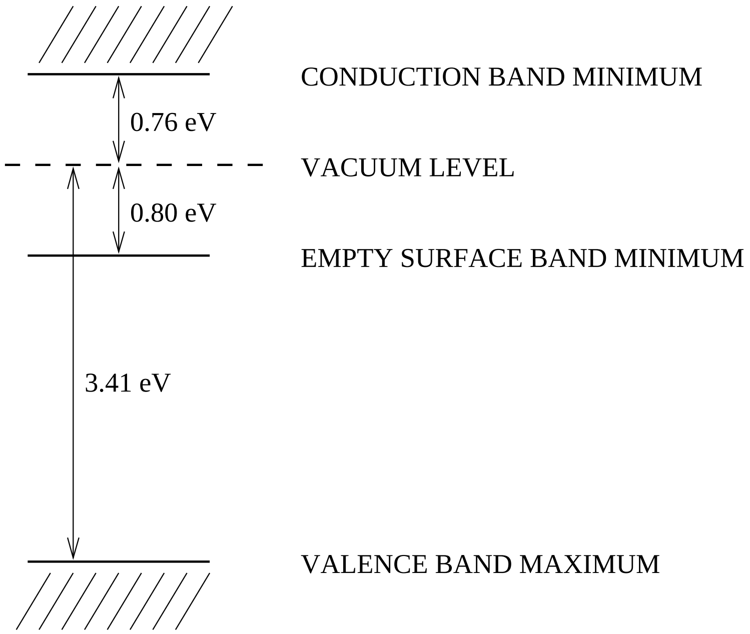

Figure 7.3: Positions of the bulk and surface bands with respect to the vacuum level, computed within DFT-LDA.

For illustration, we single out the state at the Γ point, $|\psi^{\Gamma}_{\text{surf}}\rangle$, which has the lowest energy, and should have the strongest effect on $\sigma^{\text{p}}_{\hat{\mathbf{n}}}$ according to Eq. (7.3). In Fig. 7.2, we show as a grey scale coded density plot the square modulus of $|\psi^{\Gamma}_{\text{surf}}\rangle$. Indeed, $\Delta\mathbf{J}(\mathbf{r})$ is larger where the surface state prevails. In Fig. 7.1 we plot $-\rho(z)$, where $\rho(z)$ is the integral of the square amplitude of $|\psi^{\Gamma}_{\text{surf}}\rangle$ over an atomic sphere of radius 0.42 Å, centered at each C site. The scale for ρ is chosen in such a way that, at the third layer, $-\rho(z)$ and $\delta_{||}(z)$ coincide. The close agreement between $-\rho(z)$ and $\delta_{||}(z)$ indicates that $\delta_{||}$ is indeed proportional to the square amplitude of the surface state. The agreement is not perfect for the first C layer, which experiences a different chemical environment since it is bonded to the H layer. Finally, because of the symmetry of the C(111):H surface, the expression $(\hat{\mathbf{n}}_{\perp} \cdot \mathbf{L})|\psi^{\Gamma}_{\text{surf}}\rangle$ in Eq. (7.3) vanishes. This explains why the surface state does not contribute to $\sigma^{\text{p}}_{\hat{\mathbf{n}}}$ if the field direction $\hat{\mathbf{n}}$ is perpendicular to the surface.

To understand why $(\hat{\mathbf{n}}_{\perp} \cdot \mathbf{L})|\psi^{\Gamma}_{\text{surf}}\rangle$ in Eq. (7.3) vanishes, we decompose $|\psi^{\Gamma}_{\text{surf}}\rangle$ in spherical harmonics Y^{l}_{m} inside the atomic spheres, where l and m are integer, $l \geq 0$, $-l \leq m \leq l$, and the axis of quantization is $\hat{\mathbf{n}}_{\perp}$. The surface possesses a 120° rotation symmetry along $\hat{\mathbf{n}}_{\perp}$ about the center of a H atom. By this symmetry, the spherical harmonics coefficients of a non-degenerate eigenstate at the Γ point are zero, if $m \neq 3k$, where k is an integer. Furthermore, in carbon the spherical harmonics coefficients with $l > 2$ are known to be negligible, for states near the gap. Under this assumption, the only non-zero coefficients would be those with $m = 0$, i.e. $(\hat{\mathbf{n}}_{\perp} \cdot \mathbf{L})|\psi^{\Gamma}_{\text{surf}}\rangle = 0$. The density plot in Fig. 7.2 confirms this observation, since $|\psi^{\Gamma}_{\text{surf}}\rangle$ has the characteristic shape of a p_z (Y^{1}_{0}) state.

7.5 Conclusion

In summary, we have shown that the presence of electronic surface states has a strong impact on the NMR chemical shift of atoms near the surface. Unoccupied surface states cause a paramagnetic deshielding proportional to their square amplitude. This effect may be used as a means to measure the spatial extent of surface states. We have illustrated the phenomenon for a flat surface, but a similarly strong effect can occur also for different geometries, e.g. in semiconductor nanocrystals, or zeolites, whenever surface states are present.

Bibliography

[1] J. Zhu, Ph.D. thesis, University of California at Berkeley, 1990.

[2] W. Caldwell *et al.*, Science **277**, 930 (1997).

[3] V. I. Anisimov, J. Zaanen, and O. K. Andersen, Phys. Rev. B **44**, 943 (1991).

[4] M. Czyżyk and G. Sawatzky, Phys. Rev. B **49**, 14211 (1994).

[5] A. Svane and O. Gunnarsson, Phys. Rev. Lett. **65**, 1148 (1990).

[6] A. Liechtenstein, V. Anisimov, and J. Zaanen, Phys. Rev. B **52**, R5467 (1995).

[7] P. Wei and Z. Q. Qi, Phys. Rev. B **49**, 10864 (1994).

[8] I. Mazin and V. Anisimov, Phys. Rev. B **55**, 12822 (1997).

[9] I. Solovyev, N. Hamada, and K. Terakura, Phys. Rev. B **53**, 7158 (1996).

[10] J. Perdew, in *Electronic Structure of Solids '91*, edited by P. Ziesche and H. Eschrig (Akademie Verlag, Berlin, 1991), pp. 11–20.

[11] H. Sawada, N. Hamada, and K. Terakura, Physica B **237-238**, 46 (1997).

[12] P. Dufek, P. Blaha, V. Sliwko, and K. Schwarz, Phys. Rev. B **49**, 10170 (1994).

[13] D. Singh and W. Pickett, Phys. Rev. B **44**, 7715 (1991).

[14] H. Sawada, N. Hamada, K. Terakura, and T. Asada, Phys. Rev. B **53**, 12742 (1996).

[15] D. Ceperley and B. Alder, Phys. Rev. Lett. **45**, 566 (1980).

[16] J. Perdew and A. Zunger, Phys. Rev. B **23**, 5048 (1981).

[17] N. Chen, E. Sterer, and I. Silvera, Phys. Rev. Lett. **76**, 1663 (1996).

[18] P. Loubeyre *et al.*, Nature **383**, 702 (1996).

[19] S. Weir, A. Mitchell, and W. Nellis, Phys. Rev. Lett. **76**, 1860 (1996).

[20] W. Kohn and L. Sham, Phys. Rev. **140**, A1133 (1965).

[21] R. Dreizler and E. Gross, *Density Functional Theory* (Springer-Verlag, Berlin, 1990).

[22] J. Perdew *et al.*, Phys. Rev. B **46**, 6671 (1992).

[23] O. Gunnarsson, M. Jonson, and B. Lundqvist, Phys. Rev. B **20**, 3136 (1979).

[24] C. Umrigar and X. Gonze, Phys. Rev. A **50**, 3827 (1994).

[25] C. Umrigar and X. Gonze, in *High performance computing and its applications in the physical sciences: proceedings of the Mardi Gras '93 conference*, edited by D. A. Browne *et al.* (World Scientific, River Edge, NJ, 1993).

[26] J. Slater, Phys. Rev. **82**, 538 (1951).

[27] J. Hubbard, Proc. Roy. Soc. A **276**, 238 (1963).

[28] J. Brandow, Advances in Physics **26**, 651 (1977).

[29] N. F. Mott, *Metal Insulator Transitions* (Taylor and Francis, London, 1974).

[30] N. F. Mott, Proc. Phys. Soc. **62**, 416 (1949).

[31] J. H. Rose, H. Shore, and L. Sander, Phys. Rev. B **21**, 3037 (1980).

[32] L. Sander, H. Shore, and J. H. Rose, Phys. Rev. B **24**, 4879 (1981).

[33] B. Min, T. Oguchi, H. Jansen, and A. Freeman, Phys. Rev. B **33**, 324 (1986).

[34] V. Moruzzi and P. Marcus, Phys. Rev. B **43**, 825 (1991).

[35] X. W. Wang, J. Zhu, S. G. Louie, and S. Fahy, Phys. Rev. Lett. **65**, 2414 (1990).

[36] K. Ho, C. Elsässer, C. Chan, and M. Fähnle, J. Phys.: Condens. Matter **4**, 5189 (1992).

[37] H. J. Monkhorst and J. D. Pack, Phys. Rev. B **13**, 5188 (1976).

[38] S. G. Louie, in *Electronic Structure, Dynamics, and Quantum Structural Properties of Condensed Matter*, edited by J. T. Devreese and P. Van Camp (Plenum Press, New York, 1985), p. 335.

[39] J. Ihm, A. Zunger, and M. L. Cohen, J. Phys. C **12**, 4409 (1979).

[40] O. H. Nielsen and R. M. Martin, Phys. Rev. A **32**, 3792 (1985).

[41] R. Car and M. Parrinello, Phys. Rev. Lett. **55**, 2471 (1985).

[42] R. M. Wentzcovitch, J. L. Martins, and G. D. Price, Phys. Rev. Lett. **70**, 3947 (1993).

[43] M. Parrinello and A. Rahman, Phys. Rev. Lett. **45**, 1196 (1980).

[44] R. M. Wentzcovitch, Phys. Rev. B **43**, 2358 (1991).

[45] J. Furthmüller, J. Hafner, and G. Kresse, Phys. Rev. B **50**, 15606 (1994).

[46] J. Crain *et al.*, Phys. Rev. B **50**, 13043 (1994).

[47] S. Nosé and M. Klein, Mol. Phys. **50**, 1055 (1983).

[48] W. Press, S. Teukolsky, W. Vetterling, and B. Flannery, *Numerical Recipes*, 2nd ed. (Cambridge University Press, New York, 1992).

[49] D. F. Shanno, Math. Oper. Res. **3**, 244 (1978).

[50] V. Eyert, J. Comp. Phys. **124**, 271 (1996).

[51] E. Polak, *Computational Methods in Optimization* (Academic Press, New York, 1971).

[52] J. Wang and S. Yip, Phys. Rev. Lett. **71**, 4182 (1993).

[53] A. A. Maradudin, in *Dynamical Properties of Solids*, edited by G. K. Horton and A. A. Maradudin (North-Holland, Amsterdam, 1974).

[54] D. C. Wallace, *Thermodynamics of Crystals* (Wiley, New York, 1972).

[55] N. Troullier and J. L. Martins, Phys. Rev. B **43**, 1993 (1991).

[56] M. T. Yin and M. L. Cohen, Phys. Rev. Lett. **50**, 1172 (1983).

[57] J. Crain *et al.*, Phys. Rev. B **49**, 5329 (1994).

[58] F. D. Murnaghan, Proc. Nat. Acad. Sci. USA **30**, 244 (1944).

[59] M. Côté and M. L. Cohen, Phys. Rev. B **55**, 5684 (1997).

[60] R. O. Piltz *et al.*, Phys. Rev. B **52**, 4072 (1995).

[61] R. H. Wentorf and J. S. Kasper, Science **139**, 338 (1963).

[62] H. Olijnyk, S. K. Sikka, and W. B. Holzapfel, Phys. Lett. A **103**, 137 (1984).

[63] J. Z. Hu and I. L. Spain, Solid State Comm. **51**, 263 (1984).

[64] J. Z. Hu, L. Merkle, C. Menoni, and I. L. Spain, Phys. Rev. B **34**, 4679 (1986).

[65] Y.-X. Zhao, F. Buehler, J. Sites, and I. Spain, Solid State Comm. **59**, 379 (1986).

[66] M. I. McMahon and R. J. Nelmes, Phys. Rev. B **47**, 8337 (1993).

[67] S. J. Duclos, Y. K. Vohra, and A. L. Ruoff, Phys. Rev. Lett **58**, 775 (1987).

[68] S. J. Duclos, Y. K. Vohra, and A. L. Ruoff, Phys. Rev. B **41**, 12021 (1990).

[69] J. Joannopoulos and M. L. Cohen, in *Solid State Physics*, edited by H. Ehrenreich, F. Seitz, and D. Turnbull (Academic Press, New York, 1976), Vol. 31, p. 71.

[70] R. Biswas, R. M. Martin, R. J. Needs, and O. H. Nielsen, Phys. Rev. B **35**, 9559 (1987).

[71] L. Kleinman and D. M. Bylander, Phys. Rev. Lett. **48**, 1425 (1982).

[72] B. Pfrommer, M. Côté, S. G. Louie, and M. Cohen, J. Comp. Phys. **131**, 233 (1997).

[73] N. Moll *et al.*, Phys. Rev. B **52**, 2550 (1995).

[74] R. Needs and A. Mujica, Phys. Rev. B **51**, 9652 (1995).

[75] L. L. Boyer *et al.*, Phys. Rev. Lett. **67**, 715 (1991).

[76] A. Garcia *et al.*, Phys. Rev. B **46**, 9829 (1992).

[77] J. M. Besson, E. H. Mokhtari, J. Gonzalez, and G. Weill, Phys. Rev. Lett. **59**, 473 (1987).

[78] M. S. Hybertsen and S. G. Louie, Phys. Rev. B **34**, 5390 (1986).

[79] L. C. Allen, Ann. N.Y. Acad. Sci. **118**, 883 (1965).

[80] R. Steudel, *Chemistry of the Non-Metals* (Walter de Gruyter, New York, 1977).

[81] K. Goettel, J. Eggert, I. Silvera, and W. Moss, Phys. Rev. Lett. **62**, 665 (1989).

[82] R. Reichlin *et al.*, Phys. Rev. Lett. **62**, 669 (1989).

[83] H. chacham, X. Zhu, and S. Louie, Europhys. Lett. **14**, 65 (1991).

[84] C. J. Allegre, T. Staudacher, and P. Sarda, Earth Planet. Sci. Lett. **81**, 127 (1986).

[85] D. Krummenacher, C. Merrihue, R. Pepin, and J. Reynolds, Geochim. Cosmochim. Acta **26**, 231 (1962).

[86] I. Tolstikhin and R. O'Nions, Chem. Geol. **115**, 1 (1994).

[87] J. Matsuda *et al.*, Science **259**, 788 (1993).

[88] R. Jeanloz and B. Romanowicz, Physics Today **50**, 22 (1997).

[89] A. Jephcoat *et al.*, Phys. Rev. Lett. **59**, 2670 (1987).

[90] P. Loubeyre, Phys. Rev. B **37**, 5432 (1968).

[91] A. E. Dwight, Trans. Am. Soc. Met. **53**, 477 (1960).

[92] M. Schindler, J. Am. Chem. Soc. **109**, 1020 (1987).

[93] U. Haeberlen, in *Encyclopedia of nuclear magnetic resonance*, edited by D. M. Grant and R. K. Harris (John Wiley & Sons, New York, 1996), p. 368.

[94] R. A. Wind, in *Modern NMR techniques and their application in chemistry*, edited by A. I. Popov and K. Hallenga (Marcel Dekker, New York, 1991), p. 125.

[95] C. Jäger, J. Gottwald, H. W. Spiess, and R. J. Newport, Phys. Rev. B **50**, 846 (1994).

[96] C. P. Slichter, *Principles of magnetic resonance*, *Harper's Physics Series* (Harper & Row, New York, 1963).

[97] A. Carrington and A. D. McLachlan, *Introduction to magnetic resonance*, *Harper's Chemistry Series* (Harper & Row, New York, 1967).

[98] E. O. Stejskal and J. D. Memory, *High resolution NMR in the Solid State* (Oxford University Press, New York, 1994).

[99] F. Mauri and S. G. Louie, Phys. Rev. Lett. **76**, 4246 (1996).

[100] F. Mauri, B. G. Pfrommer, and S. G. Louie, Phys. Rev. Lett. **77**, 5300 (1996).

[101] K. Ohno, F. Mauri, and S. G. Louie, Phys. Rev. B **56**, 1009 (1997).

[102] R. Ditchfield, Mol. Phys. **27**, 789 (1974).

[103] J. D. Jackson, *Classical Electrodynamics*, 2nd ed. (John Wiley & Sons, New York, 1975).

[104] G. Vignale and M. Rasolt, Phys. Rev. Lett. **59**, 2360 (1987).

[105] A. M. Lee, N. C. Handy, and S. M. Colwell, J. Chem. Phys. **103**, 10095 (1995).

[106] W. Kutzelnigg, U. Fleischer, and M. Schindler, in *NMR basic principles and progress*, edited by P. Diehl (Springer-Verlag, New York, 1990), Vol. 23, pp. 167–253.

[107] W. Schneider, H. Bernstein, and J. Pople, J. Chem. Phys. **28**, 601 (1958).

[108] M. M. Golzan *et al.*, Chem. Phys. **193**, 167 (1995).

[109] U. Schwerk, F. Engelke, R. Kleber, and D. Michel, Thin Solid Films **230**, 102 (1993).

[110] S. Kaplan, F. Jansen, and M. Machonkin, Appl. Phys. Lett. **47**, 750 (1985).

[111] R. H. Jarman, G. J. Ray, R. W. Standley, and G. W. Zajac, Appl. Phys. Lett. **49**, 1065 (1986).

[112] M. A. Tamor, W. C. Vassell, and K. R. Carduner, Appl. Phys. Lett. **58**, 592 (1991).

[113] A. Grill and V. Patel, Appl. Phys. Lett. **60**, 2089 (1992).

[114] H. Pan *et al.*, Phys. Rev. B **44**, 6741 (1991).

[115] S. M. Holl *et al.*, Mat. Res. Soc. Symp. Proc. **339**, 741 (1994).

[116] L. Merwin, C. Johnson, and W. Weimer, J. Mat. Res. **9**, 631 (1994).

[117] M. Duijvestijn, C. van der Lugt, J. Smidt, and R. Wind, Chem. Phys. Lett. **102**, 25 (1983).

[118] M. Pruski *et al.*, Phys. Rev. B **49**, 10635 (1994).

[119] A. K. Jameson and C. J. Jameson, Chem. Phys. Lett. **134**, 461 (1987).

[120] W. T. Raynes, *Nuclear Magnetic Resonance* (The Chemical Society, London, 1977), Vol. 7.

[121] W. Raynes and M. Raza, Mol. Phys. **17**, 157 (1969).

[122] F. H. A. Rummens, W. T. Raynes, and H. J. Bernstein, Phys. Chem. **72**, 2111 (1968).

[123] J. Ager III, D. Veirs, and G. Rosenblatt, Phys. Rev. B **43**, 6491 (1991).

[124] M. Hanfland *et al.*, Phys. Rev. B **31**, 6896 (1985).

[125] S. Iarlori, G. Galli, and O. Martini, Phys. Rev. B **49**, 7060 (1994).

[126] N. Marks *et al.*, Phys. Rev. B **54**, 9703 (1996).

[127] F. Patthey and W.-D. Schneider, Surf. Sci. **334**, 715 (1995).

[128] G. Cates *et al.*, Phys. Rev. Lett. **65**, 2591 (1990).

[129] D. Raftery *et al.*, Phys. Rev. Lett. **66**, 584 (1991).

[130] D. Raftery *et al.*, Chem. Phys. Lett. **191**, 385 (1992).

[131] C. R. Bowers *et al.*, Chem. Phys. Lett. **205**, 168 (1993).

[132] B. Driehuys *et al.*, Phys. Lett. A **184**, 88 (1993).

[133] H. W. Long *et al.*, J. Am. Chem. Soc. **115**, 8491 (1993).

[134] H. C. Gaede *et al.*, Appl. Magn. Reson. **8**, 373 (1995).

[135] G. Navon *et al.*, Science **271**, 1848 (1996).

[136] F. Mauri, B. G. Pfrommer, and S. G. Louie, Phys. Rev. Lett. **79**, 2340 (1997).

[137] C. Bandis and P. P. Pate, Phys. Rev. B **52**, 12056 (1995).

[138] G. Kern, J. Hafner, and G. Kresse, Surf. Sci. **366**, 445 (1996).

[139] X. Blase, A. Rubio, S. G. Louie, and M. L. Cohen, Europhys. Lett. **28**, 335 (1994).